Hydrodynamic performance of HAMCTs in steady and unsteady flows

Kaiming Ai

A thesis submitted in partial fulfillment of the requirements of the Degree of

Doctor of Philosophy

2019

Details of Publications

[1] Ai K, E.J Avital, T Korakianitis,A. Samad, N. Venkatesan "Surface wave effect on marine current turbine, modelling and analysis." Mechanical and Aerospace Engineering (ICMAE), 7th International Conference on. IEEE, 2016.

[2] Ai K, E.J Avital, Shen X, Samad A and Venkatesan N (2018) "The surface curvature effect on performance of a laboratory scale tidal turbine" IAENG World Congress on Engineering WCE- 2018, London

[3] Avital, E.J., Ai, K., Venkatesan, N.b Samad, et al. Hydrodynamic assessment of a dual-rotor horizontal axis marine current turbine, International Journal of Engineering and Technology(UAE), Volume 7, Issue 4.10 Special Issue 10, 2018, Pages 455-459

Acknowledgements

I would like to express my sincere appreciation to my doctoral supervisors, Dr Eldad Avital and Prof. Ante Munjiza, for their patience, advice, support and encouragement.

I would thank the other members of staff who have provide continuous maintenance and update on the high performance computers "Apocrita" at Queen Mary, University of London.

I also thank all my colleagues and friends for their companion, assistance, encouragement and proofreading. The list of names are Dr. Jiahuan Cui, Yan Yan, Dr. Xiang Shen, Mingyang Wang, Dr. Andrew P. Heffron, Dr. Haifeng Wang, Dr. Xiaolong Tang, Dr. Jia Mao, et al.

I would like to thank my families for their continuous support during my doctoral study.

Special acknowledgement is given to the support of China CSC and QMUL joint PhD Scholarship.

Abstract

The hydrodynamic performance of the common three-blades horizontal axis current turbine (HAMCT) is computationally investigated to seek paths of improvement. Two computational approaches are used, namely the Blade Element Method (BEM) and Computational Fluid Dynamics (CFD)-Reynolds Averaged Navier Stokes (RANS). Two BEM codes were written for steady and unsteady calculations. Both account for hub/tip losses, turbulent wake effect and stall delay. Dynamic wake model was used for the unsteady BEM. Ansys is used for CFD-RANS.

Three cases are studied; (i) Hydrodynamic improvement by replacing the common low Reynolds number asymmetric E387 profile with its CIRCLE previously-redesigned A7 profile calling for continuous surface curvature. This yields better high-angle of attack (AOA) performance. As result the A7 turbine outperforms the E387 turbine for low tip speed ratio (TSR) from mild improvement for the optimally twisted blade to a much higher improvement for the non-twisted blade.

(ii) The dual-rotor turbine, where each rotor is optimally pitch-fixed for its upstream velocity, thus fitting rectilinear tidal current with no need of pitch control. Symmetric profiles outperform the asymmetric profiles when the rear rotor is correctly used, yielding an increase of up to 20% in the combined power according to the BEM coupled with the Park wake model. An analytical estimate backs this estimate. RANS is used to assess and improve the Park model.

(iii) Surface wave effect is investigated for HAMCT close to the surface using BEM coupled with gravity wave theory and CFD. For the first time, effect of large waves is investigated to show the turbine's non-linear time response at low TSR. Blade loading, power spectra and time averaged proprieties are also analysed.

All computations were compared to experimental results when available, generally yielding good agreement. Cases of disagreement are also discussed.

Contents

List of Figures

List of Tables

List of Symbols

Roman symbols

a	axial induction factor
a'	tangential induction factor
A	rotor area
$A(r)$	area of wake region at a given axial distance (x/D)
B	number of blades
c	chord length
C_D	drag coefficient
C_L	lift coefficient
C_P	power coefficient
C_n	normal force coefficient
C_t	tangential force coefficient
C_T	thrust coefficient
D	Diameter of rotor
f	frequency
f_s	separation function
g	gravity
h	water depth
H	wave height
k	turbulent kinetic energy, wave number
L	lift
M	mass source, torque(moment)
m	mass
p	pressure
P	power, mean component of pressure
r	radius
R	radius of rotor

Re	Reynolds number
Re_c	Reynolds number based on chord length
S_k	user defined source term
t	time
T	thrust
T_{ij}	stress tensor
TI^s_∞	stream-wise turbulence intensity
TI_∞	3D turbulence intensity
U_∞	free stream velocity
$\overline{u}$	instantaneous velocity in wave and current
u_r	axial component of wave velocity
$\overline{U}$	area averaged axial mean velocity
$\mathbf{v}$	velocity vector (inertial reference frame)
$\mathbf{v_r}$	velocity vector (moving reference frame)
V	main part of velocity, volume
W	induced velocity
w_r	vertical component of wave velocity
x	non-dimensional radius, $x = r/R$
X	rotor spacing in dual rotor turbine
y^+	non-dimensional wall distance, y plus
z_0	hub installation depth

Greek symbols

α	angle of attack
α_q	volume fraction of the q^{th} fluid
β	twist of blade
θ	local pitch angle, wave phase
θ_T	tip pitch angle
ϕ	angle between rotation plane and relative inflow velocity, velocity potential
δ_{ij}	Kronecker delta
μ_t	turbulent eddy viscosity
μ	dynamic viscosity
ν	kinematic viscosity
ρ	density
σ	solidity
τ_{ij}	viscous stress tensor
τ_1	time constant in dynamic wake model of unsteady BEM
τ_2	time constant in dynamic wake model of unsteady BEM
ϵ	turbulent dissipation rate
ω	Specific dissipation rate, wave frequency
Ω	angular velocity
λ_r	local speed ratio
ψ	azimuthal angle
η	surface wave elevation

Abbreviation

BEM	blade element momentum
CFD	computational fluid dynamics
CIRCLE	prescribed surface curvature distribution blade design
DES	detached eddy simulation
HAMCT	horizontal axis marine current turbine
LES	large eddy simulation
LSB	laminar separation bubble
MCT	marine current turbine
RANS	Reynolds averaged Navier Stokes
SST	shear stress transport
TI	turbulence intensity
TSR	tip speed ratio
TKE	turbulent kinetic energy
UDF	user defined function
VAMCT	vertical axis marine current turbine

Chapter 1

Introduction

1.1 Marine energy

Renewable energies include two broad categories: 'modern renewables' and the traditional biomass. The term 'modern renewables' denotes all kinds of renewable techniques with exception of the traditional biomass, which represents the usage of solid biomass with traditional technologies, such as open fires for cooking, ovens for cooking, residential heating, and small-scale agricultural and industrial processing. The traditional biomass is more often used in rural areas of developing countries. According to the recent REN21 report [1], 19.3% of global energy came from renewable energy in 2015, in which 'modern renewables' constituted nearly 10.2%, and hydropower made up about 3.6% (Fig. 1.1). Among those renewable resources, one of the most promising sector is marine energy, which generated 536 MW by the end of 2016.

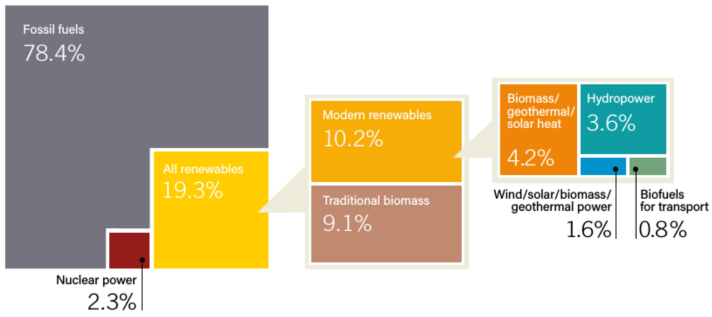

Figure 1.1: Estimated renewable energy share of total energy consumption,2015 [1]

Marine energy, also referred to as ocean energy, and marine hydro-kinetic energy (MHK), includes various means through which energy can be harnessed from the sea and ocean. Marine energy is an important form of renewable energy, particularly to countries with long coastal lines such as the UK, India and China. There are various types of marine energy, including wind-generated waves, tidal current, ocean thermal, etc. Recent ocean renewable technologies mainly harvest the wind-generated waves and tidal current energy. Devices mainly designed to extract wind generated wave energy are named wave energy converters (WECs), which do not have rotors. Typical types of WECs include attenuator, point absorber, and terminator [17]. There are many ways to extract energy from the tidal energy. Tidal basin (fig. 1.2a) and marine current turbine (Fig. 1.2b) are the two basic ways to extract tidal current energy. Tidal basin exploits the potential energy, while

marine current turbine extracts the kinetic energy. Devices extracting the kinetic energy of tidal energy are named tidal turbine, tidal current turbine, tidal stream turbine, tidal stream convector, and marine current turbine in different references. Actually, all these devices share the same principle and are referred to as marine current turbine in this thesis. For tidal basin, barrages or dams are required to create a potential drop. The building of such constructions need large financial investment and may change the marine ecosystem [18]. Recent developments in marine current turbine and the identification of sites around the world with high tidal energy as the Pentland Firth in the UK and the Gulf of Kutal in India, mean that the build up of such barrages is not a necessary condition any more. Marine current turbine does not need these civil constructions, thus has lower capital cost, fewer environmental and visual impact. However, marine current turbine technology is relatively immature compared to tidal basin. In summary, tidal basin and marine current turbines have advantages and disadvantages and can complement each other.

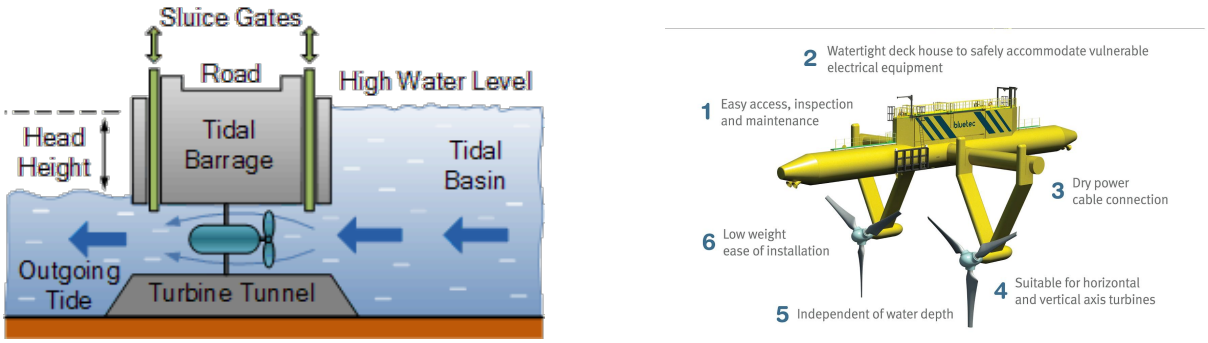

(a) Schematic diagram of tidal barrage [19] (b) Bluetec marine current turbine [20]

Figure 1.2: Examples of Tidal barrage and marine current turbine

Compared to solar and wind power, the distinct advantage of tidal current power is its predictability. Solar energy is under the influence of rain, clouds and fog. Wind power is influenced by wind speed and force. Tidal current, driven by the gravitational force of the moon and sun, is immune to the above mentioned meteorological conditions. Thus tidal power is more reliable and predictable than solar and wind power. The drawback of marine current turbine is that it is not as well developed as solar and wind power energy. This is due to the fact that devices that harness marine current energy present a unique set of engineering challenges with regard to design, installation, support structure and maintenance.

1.2 Research questions

1.2.1 Surface curvature effect on airfoil and blade

Generally, a horizontal axis marine current turbine consists of two or three blades. The blade is composed of one or more hydrofoils with different shape and length from the blade root to tip. Similar as small wind turbines, low Reynolds number airfoil (hydrofoil) is also widely used for small marine current turbines. A typical example is the Eppler 387 (E387) airfoil which was designed by R. Eppler [21] in the 1990s and later widely used for small wind and marine current turbines [13, 22, 23]. A landmark experimental study

on the E387 airfoil was carried out by Selig [24], who conducted wind tunnel research on six airfoils for use on small wind turbines at the University of Illinois at Urbana-Champaign in 2004. The surface oil visualization and pressure distribution along chord length direction show evidence of laminar separation bubble near the leading edge at Reynolds number order of 1×10^5.

For wall bounded flow, the boundary layer starts from the leading edge of the profile and develops towards the trailing edge. The leading edge shape plays an important role at the start of boundary layer and affects the development of boundary layer along the blade surface [25]. The importance of surface curvature discontinuity of airfoils and blades has been realized in references [26, 27]. It can lead to sharp jump in the pressure, resulting in early transition to turbulence at high Reynolds numbers and early flow separation at low Reynolds numbers. Korakianitis [28] proposed a method named prescribed surface curvature distribution blade design (CIRCLE) method to improve the surface curvature continuity. The CIRCLE method redesigns the blade profile coordinates to yield a continuous curvature and slope of curvature, thus a smooth pressure and velocity distributes along the blade surface. Korakianitis applied the CIRCLE method to various blades [29] and airfoils [30], noticeable improvement of lift coefficients were recorded. Later Shen et al. [11] further extended Korakianitis' work. Shen conducted experimental and numerical study of Eppler 387 and redesigned A7 airfoil at three different Reynolds number (1×10^5, 2×10^5 and 3×10^5) . Shen et al concluded that removing the surface curvature discontinuity increases the aerodynamic performance and reduces drag of airfoil at high angle of attack (AOA) and stall condition. Shen et al also compared the performance of 3KW small wind turbines whose rotors were composed of E387 and A7 airfoils respectively. The steady Blade Element Momentum results showed that the A7 had noticeable improvement of power coefficient at low tip speed ratio (TSR), and marginal improvement at optimal and large tip speed ratio.

Song et al [31] removed the surface discontinuity at leading edge and main surface of a compressor blade respectively, and found that smoothing the leading edge has better performance than its main surface counterpart. The surface curvature of NREL S814 airfoil was smoothed using [30] and renamed as R1, the RANS results showed that the R1 had lower lift and drag but higher lift to drag coefficients at $Re = 1.5 \times 10^6$ with angle of attack varies from 3-11 degree.

The aforementioned research only analyzed the surface curvature effects on performance for 2D isolated airfoil, turbine cascades using numerical or experimental methods. Shen et al [11] studied the performance improvement of a 3D wind turbine model by replacing E387 airfoil with redesigned A7 airfoil at all blade stations using a simple method like BEM, but have not explain the mechanism of improved power coefficient at small tip speed ratio. Also, the power performance obtained from BEM has not been validated by comparing with experimental data or more advanced CFD methods.

1.2.2 Dual rotor design for a bi-directional tidal current flow

The term "current" denotes the motion of water when used in association with water. Typical water currents include rainwater, open channel flow, and oceanic currents. Gravity is the driving force for rainwater and open channel flow, while ocean currents are driven by several factors including density difference, wind, and most importantly the gravitational attraction of the sun and moon on earth's oceans. Tidal current includes flood and ebb phases. Tidal current is in flood phase when it flows towards the shore, and

in ebb phase when it returns back the ocean. Tidal current is governed by the rise and fall of the tides, and changes direction in every few hours. The reversing flow direction problem can be addressed using two control systems, namely pitch and yaw controls. An example of a MCT using yaw and pitch control systems is the AR1500 turbine of Atlantis Resources Corp.

The yaw control makes the rotational plane perpendicular to incoming free stream velocity. This system is needed for wind turbines because the wind velocity direction changes at different days and seasons. The performance of wind turbine plunges when the yaw angle reaches a certain degrees. For a marine current turbine with yaw control system, the yaw control system only operates between ebb and flood phase. The yaw control system does not operate during a single phase of ebb or flood because the current velocity varies in a small range of degrees in a single phase of ebb or flood.

To reduce the manufacturing cost and simplify the control systems, a MCT with only pitch control can be employed to deal with the bi-directional problem of tidal current. Zero yaw control can be employed for tidal current because the tidal current direction is relative fixed during single phase of ebb or flood. However, the pitch control system is a weak joint in terms of structural strength, which is easy to break and reduces the reliability of a MCT.

Another possible solution for bi-directional current flow is the dual rotor configuration without pitch control and yaw control. This significantly reduces the capital cost and improve the structural intensity. The left rotor blades are pitched at the optimal angle for flow coming from the left and the right rotor blades are optimally pitched for flow coming from the right. In this study, the rotor with the blades that is correctly-pitched to the flow is called the front rotor and the other one is the rear rotor. This configuration was used for example in the legacy AK1000 marine current turbine (Fig.1.3) designed by the Atlantis Resources Corp. However, it leaves the question what to do with the rear rotor. One way is to leave the rear rotor stationary, another option is to use rotational speed control that is common in marine turbines [32–34] in order to maximise energy extraction from the rear rotor. The dual rotor configuration is different from counter rotating wind turbine whose blades are optimally pitched in one direction.

Figure 1.3: AK-1000 Atlantis (D=18m) [2]

1.2.3 Unsteady wave effect on performance of a HAMCT

Generally, there are five types of waves in the ocean environment, namely sound waves, capillary waves, gravity surface waves, internal waves and planetary waves. Sound waves are caused by the compressibility of water, which is very small and can be ignored in normal condition. Capillary waves characterizing high frequency, are due to joint effect of the turbulent wind and surface tension. Gravity waves can be sub-divided into surface and internal gravity waves. Surface gravity waves are mainly driven by wind and are particularly enhanced by the wind if their phase speed is comparable with the wind speed, while the internal waves are due to density differences in a stratified fluid. The variation of the equilibrium potential vorticity gives rise to planetary waves characterizing slow frequency and large length scale. Other forms of waves includes tides and Tsunami. Table 1.1 summaries typical wave types in the ocean environment, physical mechanisms generating these waves, and their time periods. Among these waves, tidal current and gravity waves are the most important for offshore marine current turbine operation, offshore civil structures and ship performance [16]. Typical periods of tides vary 12-24 hours, however wind waves and swell have a much shorter wave periods, which are normally below 30s. These short period waves pose a unique challenge for the performance and fatigue of marine current turbines. Different wave theories are developed to describe waves in river and oceans, their applicability for different waves is presented in Fig. 1.4.

Table 1.1: Wave types, physical mechanisms, and periods [16]

Wave type	Physical mechanism	Periods
Capillary waves	Surface tension	<0.1s
Wind waves	Wind shear, gravity	<15s
Swell	Wind waves	<30s
Internal waves	Density structure instability	10 min-15h
Tsunami	Earthquake	10 min-2h
Tides	Gravitational action of the moon and sun, earth rotation	12-24h
Storm surges	Wind stresses and atmospheric pressure variation	1-3 days

Regions of Oceans can be grouped into shallow water, intermediate depth and deep water based on the water depth (h) to wave length (λ) ratio,h/λ. Shallow water waves denotes the waves in a region where the h/λ <1/20, while the deep water is a region where the h/λ >1/2, and in between is intermediate depth water region. Most of seabed mounted marine current turbines are installed in shallow and intermediate waters, while floating marine current turbines can be deployed in deep water.

Much of the technology and modelling used for the marine current turbine has been imported from the wind power industry which in turn has relied on aerospace technology developed for propellers and fans. However, the free-stream MCT faces challenges different from its wind turbine counterpart. While the flow direction is well known in advance, it turns to the opposite direction during the day and flow unsteadiness can be enhanced by gravity waves as well as cavitation. The latter can occur for high flow velocities and when the blade passes near the free (water) surface reducing the static pressure below the cavitation level. This is not common for MCTs [35]. However, the effect of gravity waves and particularly surface waves (i.e. maximum water displacement at the free surface) is more common and can degrade the turbine performance.

Several laboratory researches on the effect of wave on the performance and loading of

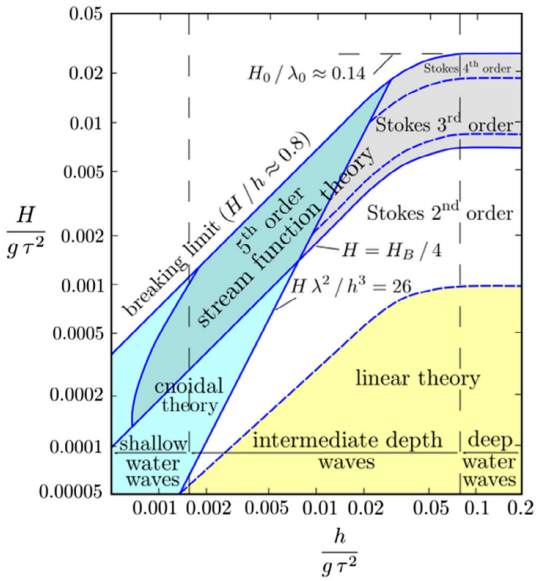

Figure 1.4: Applicability of wave theories [3]

MCTs were presented in references [14,36,37], just to name a few. However, most of the studies focused on simple linear waves. Luznik studied a second Stokes wave effect on a small scale HAMCT in the laboratory towing tank, which provides valuable data for numerical modelling validation. However, only one wave amplitude was tested. Three basic wave parameters include water depth, wave length, and wave amplitude. Different wave parameters will affect the performance and loading of a HAMCT in different ways, thus a wave parametric study on a HAMCT is need for providing more detailed database for engineering application. Another important parameter is the installation depth of a HAMCT. A HAMCT may have different performance when it is installed at different locations in the gravitational direction.

1.3 Objectives and contributions

The main objectives of study and associated outcomes are as follows:

1. The performance improvement of a general three bladed HAMCT using the CIRCLE method is to be evaluated by both fast BEM and more advanced methods such as CFD-RANS. Outcome: the redesigned A7 HAMCT had a mild better performance at low tip speed ratios, which expanded the operational range. Fluid visualization showed that flow separated from the blade surface where the radial distance was below half blade length. Further blade optimizations were conducted based on Burton and implicit models derived from the blade element momentum theory. For a HAMCT redesigned based on the implicit model, 13.1% increase of power coefficient was obtained at design tip speed ratio, although the optimized rotor was subjected to a 5% higher thrust loading. The implicit model and CIRCLE method can be used together to improve the power efficiency of a HAMCT.

2. A small fixed pitch HAMCT composed of counter rotating dual rotor is proposed for bi-directional tidal current. Counter rotating dual rotors using both symmetric and asymmetric profiles (Eppler 387 and NACA0012) are to be studied. Outcome: both BEM-Park model and CFD-RANS were used to study the performance and thrust of the

dual rotor HAMCT. The results showed that there was good potential power gain up to 0.55 for a mid-size (3.5m) dual-rotor HAMCT without pitch and yaw control.

3. Effects of surface wave parameters and turbine operating depth on performance and loading of a HAMCT are to be analyzed using both unsteady BEM and CFD-RANS. This will include prediction of the hydrodynamic power and and blade loading development in time as they are affected by surface waves. Both linear and non-linear surface waves are to be considered. Outcome: these parametric studies provide valuable guide for industrial installation and operation of a HAMCT. An unsteady BEM code including the wave effects was developed by Dr. Avital and modified in this thesis. It is shown that a large amplitude wave, but still long wave can affect the time-averaged coefficient of power and also introduce non-linearity in the time response of the turbine particularly at low tip speed ratio. This can have consequence for an effective control of the turbine.

All three contents mentioned above were published in three papers noted on page i.

1.4 Structure of the thesis

The order of information this thesis is organized as follows:

In Chapter 2, a detailed literature review on marine current turbines is presented. This includes a review on the kinetic energy available in the ocean environment, types of marine current turbines, steady and unsteady modelling of horizontal axis marine current turbines, counter rotating dual rotor, and wave effects.

Chapter 3 introduces the computational hydrodynamic methodologies used in this thesis. Both the steady BEM and unsteady BEM incorporated with TUDK dynamic wake model are discussed. The turbulence models for Reynolds Averaged Naiver Stocks equations are also presented with emphasize on eddy viscosity models. This is followed by numerical approaches for turbine modelling, including both moving reference frames and sliding mesh methods. Finally, wave modelling are described, including the one phase approaching and free surface modelling techniques.

The first section of Chapter 4 evaluates the effects of the blade's surface curvature on the hydrodynamic performance of a laboratory scale turbine model. This is followed by blade optimization based on the blade element momentum theory which involves changing the profile's chord length and pitch angle along the spanwise direction of blade.

Chapter 5 presents two dual-rotor HAMCTs with fixed pitch used for bi-directional current flow. The steady BEM is coupled with Park wake model and CFD-RANS is used to assess that coupling. The asymmetric E387 and symmetric NACA 0012 profiles are compared in terms of performance and thrust.

Chapter 6 pursues unsteady modelling of surface wave effect on the performance and loading of a HACMT. Parametric study is carried out and it includes the effects of wave amplitude, wave-turbine frequency ratio, tip clearance distance. Both the unsteady BEM coupled gravity wave theory and the CFD software ANSYS are used for this analysis, where the User Defined Function (UDF) capability in ANSYS is used to mimic the effect of surface wave induced velocities.

Chapter 7 presents the summary and conclusions for this thesis, followed by further research work.

Chapter 2

Literature review

2.1 Marine current turbine

The marine current turbine is a relatively new technology and has a short history. Briefly, the marine current turbine shares the similar principle as the wind turbine, which extracts the kinetic energy from the moving air. Compared with the wind turbine, the advantages of the marine current turbine includes stability, availability of a large water flow, predictability of the flow speed, and less visual impact.

The first prototype marine current turbine was installed on the North Devon coast of England in 2003 (Fig.2.1a). SeaGen, the first commercial scale marine current turbine in the world, was installed in Strangford Narrows in 2008 [38] (Fig. 2.1b). The SeaGen marine current turbine produces more than 6,000 MWh every year, which opens up a new epoch in tidal stream generator. In 2006, a 100 kW Aquanator ^{TM} device was installed and connected to the national grid in Victoria, Australia [39].

2.1.1 Categories of marine current turbine

According to the European Marine Energy Center (EMEC) [41], marine current turbines could be classified into six categories, namely horizontal axis marine current turbine(HAMCT), vertical axis marine current turbine(VAMCT), ducted marine current turbine, tidal kite, oscillating hydrofoil, and archimedes' screw as presented in Fig. 2.2. Among all these types, horizontal and vertical axis marine current turbines are predominant in the market up to now.

The HAMCT and VAMCT have similar design as horizontal and vertical axis wind turbines. The rotational axis of the HAMCT is normally parallel with the free stream velocity, while VAMCT's axis is perpendicular to the free stream velocity. Fig. 2.2 (a) illustrates the 1.5MW AR1500 HAMCT which was developed in MeyGen Tidal energy project funded by the Atlantis Resources Limited. The diameter of AR1500 is 18m, and its length is 12m. This turbine is designed to operate at 14 rotations per minute in a current velocity of 3m/s. A typical VAMCT, Subsea Power Hub, is presented in Fig. 2.2 (b). This turbine was developed by EC-OG Ltd and tested at EMEC's Shapinsay sound test site in 2013.

The vertical axis turbine can be lift or drag based device. The drag-based device is typically limited to low tip speed ratio (TSR) and the lift-based device excels at high TSR, where $TSR = \Omega R/U_\infty$, Ω is the rotational speed of the turbine, e.g. round per minute (RPM), R is its radius and U_∞ is the freestream water velocity. The lift-based

(a) Seaflow [38]

(b) SeaGen [40]

Figure 2.1: Seaflow and SeaGen Turbine

vertical axis turbine can produce a higher coefficient of power (C_P) than the drag-based one, but it is still not as high of the horizontal axis turbine. This is because the blade profile is at the wrong angle of attack (AOA) during some of the the cycle of the vertical axis turbine [42]. This can be partly mitigated using a variable pitch for the blades, setting the blade orientation during the cycle in order to place it in a way of producing high hydrodynamic efficiency (lift to drag ratio) most of the cycle. This method has gained good interest and coupling this approach with computational fluid dynamics (CFD) design has been suggested [43]. However, it also leads to complexity in terms of additional machinery on the turbine and appropriate pitch-control. The VAMCT has its advantages in terms of current velocity direction, while the HAMCT normally needs a pitch control system to place the rotational plane normal to the current direction for bi-direction nature of tidal current. The pitch control system is a vulnerable component in terms of structural strength, and increases the manufacture cost. Thus, the pitch control system is normally available for large size HAMCTs, while it is neglected for small size HAMCTs.

Other less popular turbines include ducted marine current turbine, tidal kite, oscillating hydrofoil, and, archimedes' screw. Fig. 2.2 (c) shows the 250kW Open Centre Turbine designed by OpenHydro Ltd in 2005. It was tested at EMEC tidal test site and successfully installed and situated at the Fall of Warness off the island of Eday UK in 2006. The ducted turbine takes advantages of the venturi effect which accelerates the incoming current velocity, however the shroud structure increases the manufacture cost. Fig. 2.2 (d) shows a kite-like turbine named Deep Green, which was invented by Sweden engineer Magnus Landberg. The Deep Green turbine has a 0.5MW power production, which is relative small compared to the conventional HAMCT or VAMCT. However, the Deep Green turbine can operate at a depth of 60-120m below the mean free surface level, which is deeper than the installation depth of HAMCT and VAMCT that varies from 30m to 80m.

Fig. 2.2 (e) presents a oscillating hydrofoil named Stingray Assembly that was proposed by Engineering Business Ltd in 2005. The full scale prototype has a power production of 150kW. The oscillating hydrofoil has a simpler geometry compared with the HAMCT and VAMCT. However, the power efficiency of oscillating hydrofoil is lower than

(a) AR1500 (Atlantis Resources Ltd)

(b) Subsea Power Hub (EC-OG Ltd)

(c) Open Centre Turbine (OpenHydro Ltd)

(d) Deep Green (Minesto Ltd)

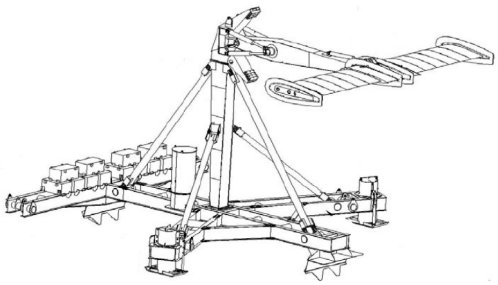

(e) Stingray asembly (Engineering Business Ltd)

(f) Fulmill (Fulmill Ltd)

Figure 2.2: Examples of different types of MCT

its conventional turbine. Meanwhile, the oscillating hydrofoil has a complex motion which requires continuous monitoring. This reduces the reliability of the operating system.

Fig. 2.2 (f) illustrates a archimide's screw type of turbine named Flumill system that was proposed by Flumill Ltd in 2002. The turbine blade is composed of a helical screw structure that is originally designed for water based streams.

2.1.2 The support structure of tidal turbines

The support structure is vital for the sustainable operation of marine devices, yet there is not much experience with the foundation of marine current turbine because the first commercial marine current turbine was built just in 2008. The support structure of a

Marine Current Turbine includes three components: foundation, load transmission and connection. Orme et al. compared six concepts of support structures (Fig.2.3), which are briefly described below [4]. The first type of support structure is named the sheath system, where a long circular tower is installed on the seabed and its top is above the mean free surface level. The rotor and nacelle could be raised and lowered for installation, inspection and maintenance. A typical example of this type of support structure is the seaGen turbine manufactured by Marine Current Turbine Ltd. The second type of support structure is the anchored system. The buoyancy of the nacelle gives tension to the anchor chain and the rotor is held in a downstream position. The third type of support structure is guyed tower design which uses the buoyancy of the nacelle to tension multiple chains. The fourth type of support structure is a top mounted system. In this model, the tower is totally submerged in the water. The fifth type of support structure is telescopic system. The blades and nacelle are submerged in operation and extended to surface during maintenance. The sixth type of support structure is the shrouded system in which a cylindrical shroud is used to concentrate ocean water around the rotor. Among these types of support structures, the most popular are the sheath and top mounted.

2.1.3 Basics of tidal turbines

The basic quantities for MCTs analysis include coefficient of power, C_P, coefficient of thrust, C_T, coefficient of moment,C_M, and tip speed ratio, TSR. If a MCT is situated in a flow with a free stream velocity of U_∞ and density of ρ, then the overall kinetic energy (P_{ref}) that can be extracted in a swept area of A is:

$$P_{ref} = \frac{1}{2}\rho A U_\infty^3 \tag{2.1}$$

The power obtained by a MCT can be derived from Euler's turbine equation [7]. The power$P$ and torsional moment (torque),M is related in the following relationship:

$$P = \Omega M_{axi} \tag{2.2}$$

where Ω is the angular velocity of a turbine, and M_{axi} is the moment of fluid on turbine in the axial direction. The axial force in the flow direction is denoted as thrust, T. The tip speed ratio is defined as the ratio of the tangential speed of blade's tip to the free stream velocity. Normally, these quantities are normalized and their definitions are written as:

$$C_P = \frac{2P}{\rho A U_\infty^3} \tag{2.3}$$

$$C_T = \frac{2T}{\rho A U_\infty^2} \tag{2.4}$$

$$TSR = \frac{\Omega R}{U_\infty} \tag{2.5}$$

where R is the radius of turbine. Power and thrust coefficients are usually plotted against TSR in the steady study of turbines, also known as performance and thrust curves.

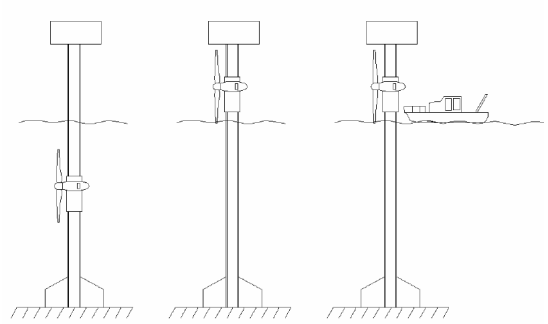

(a) The sheath system

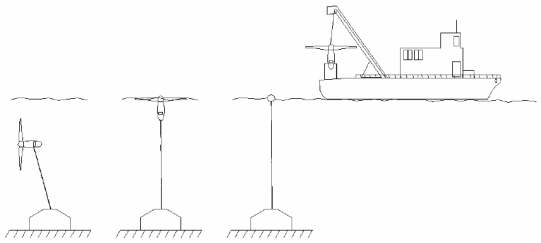

(b) The anchored system

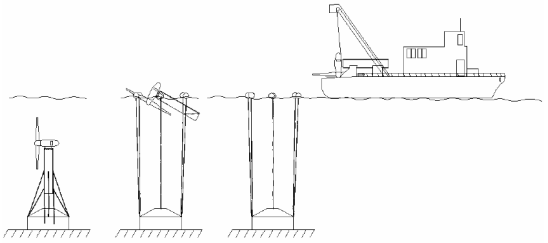

(c) The guyed system

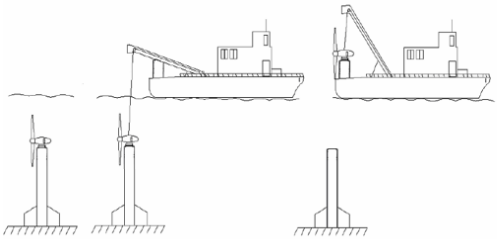

(d) The top mounted system

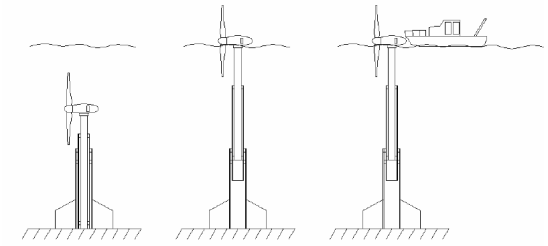

(e) The telescopic system

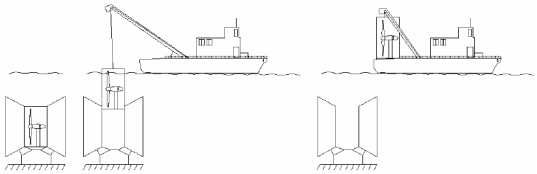

(f) The shrouded system

Figure 2.3: Schematic of support structures of marine current turbine [4]

2.2 Brief review on turbulent flow simulation

Turbulent flow is abundant in most natural flows and engineering practice. Common examples of turbulent flow are blood flow in arteries, oil transport in pipelines, lava flow, and ocean currents. However, it is not easy to give a clear definition of turbulent flow due to its complex nature. Lesieur [44] noted that "turbulence is a dangerous topic which is at the origin of serious fights in scientific meetings since it represents extremely different points of view, all of which have in common their complexity, as well as an inability to solve the problem. It is even difficult to agree on what exactly is the problem to be solved."

Numerous renowned researchers have contributed to turbulence study such as Osborne Reynolds, G. I. Taylor, Prandtl, von Karman, and Lewis Richardson, just to name a few. Their main contributions to the understanding of turbulent flow are highlighted as below:

In 1883, Osborne Reynolds, the first person to conduct a systematic work on turbulence, conducted his famous pipe flows experiments which demonstrated that the flow

becomes turbulent or irregular if the Reynolds number is above a certain critical value. In 1921, the idea of a correlation function was proposed by the British physicist G. I. Taylor. During the 1920s, the mixing length theory was well developed by Prandtl and von Karman. In 1922, the idea of energy cascade was proposed by a British meteorologist Lewis Richardson [45].

As the understanding of turbulence has progressed, researchers have found that turbulent flow has several general characteristics: nonlinearity, diffusivity, vorticity and dissipation.

There is a variety of numerical methods to compute turbulent flow, and the most well known methods are the Direct Numerical Simulation (DNS), Detached Eddy Simulation (DES), Reynolds-Averaged Navier-Stokes (RANS)-based simulation and Large Eddy Simulation (LES).

In the Direct Numerical Simulation approach, the Navier-Stokes equations are solved without averaging or approximation. This makes direct numerical simulation is the most accurate approach. To capture the dynamics of the smallest scales of the flow, the grid spacing must be at least at the Kolmogorov length scale which is the smallest scale in the turbulence dynamics. Meanwhile, the computational domain must be large enough to represent the largest scales which are typically comparable in size to the characteristic length of the mean flow. As turbulent flows contain a wide range of length and time scales, direct numerical simulation is very computationally expensive and mainly used for simple geometries, such as the airfoil and circular cylinder.

LES is a filtering approach, in which the large eddies are computed and the smallest eddies are modelled. Therefore, LES falls between DNS and RANS in terms of the fraction of the resolved scales. As the smallest eddies are modelled, the smallest cells and time steps in large eddy simulation are larger than their counterparts in direct numerical simulation. Hence, LES saves more computer sources of the same Reynolds number and could achieve much higher Reynolds numbers compared with DNS [46].

The DES model, also referred as the hybrid LES/RANS model, is a combination of both the LES and RANS. The unsteady RANS model is used in the boundary layer, while the LES approach is applied to the other regions, where large unsteady turbulence scales dominate [10]. The DES model is cost effective in the boundary layer, compared with the LES model, which resolves all the boundary layer. However, the DES model still require extensive CPU resources, and too expensive for the industrial flow simulation.

In RANS, the time averaged motion is computed while the effect of fluctuations is modelled. The basic idea of Reynolds averaging is that the variables in the instantaneous Navier-Stokes equations are split into a mean part and a fluctuating part. The effects of the fluctuating part (i.e. the Reynolds stress) is modelled. Normally, RANS models are recommended for complex geometry and flows, while the LES and DES are limited to simple flows and academic study.

2.3 Steady flow study of HAMCTs

The strict definition of steady flow is that the fluid quantities (density, velocity, pressure) at any fixed point do not change with time. A broad definition of steady flow is that the mean part of flow quantities at any fixed point do not change over long time periods. In physical and numerical modelling, the incoming flow seen by a HAMCT is often simplified as uniform steady flow. This simplification reduces the difficulty in physical experiments

and computational resources in numerical modelling.

2.3.1 Physical experiments

Normally, test facilities such as towing tank or cavitation tunnel can not accommodate full scale turbine models. Also, a full scale model is much more expensive and time consuming than a small scale model. Thus, small scale model is more popular in the laboratory experiments. The diameter of small turbine model varies from 0.2m to 1.5m, which depends on the sectional size of the towing tank or tunnel. For simplification, an isolated small turbine model subject to steady uniform inflow is used to estimate the overall performance of a MCT. For physical quantity measurement, the thrust and torque can be measured by dynamometers. Fluid velocity can be measured by various techniques, such as the particle image velocimetry (PIV), acoustic Doppler velocimeter (ADV), Acoustic Doppler current profiler (ADCP), and pitot probes.

The main quantities of interest are power, moment, thrust, and wake characteristics. Performance and thrust are two of the most important parameters in the analysis of a HAMCT. Parameters affecting the performance of a MCT include blade geometries (blade profile, pitch angle, chord length), inflow condition, cavitation, and blockage effects (free surface and seabed).

The on site measurements of turbulence intensity is presented in the table 2.1, where TI^s_∞ stands for 1D turbulence intensity. In water flume tests, the turbulence intensity level is normally lower than 3% [47], which is lower than the values on field-site. Mycek et al. [48] studied the effect of turbulence intensity level on the mean performance and wake behind an isolated turbine model. Water flume tests showed that the turbulence intensity had slight effect on mean coefficient of power and thrust, but large impact on wake.

Table 2.1: On site measurements of turbulence intensity

Location	TI^s_∞ (%)	TI_∞ (%)	U_∞ (m/s)	h(m)	Techniques	Ref
Island of Eday, UK	10-11	7.9-8.7	1.5	5.0	ADCP	[49]
Sound of Islay, UK	12-13	9.5-10.3	2.0	5.0	ADV	[50]
Puget Sound, USA	8.4/11.4	6.6/9.0	1.3 ($\pm$ 0.5)	4.7	ADV	[51]
Strangford Lough, UK	4-9	3.2-7.1	1.5-3.5	14	–	[52]
East River, NY,USA	20-30	16-24	1.5-2.3	5.22	ADCP	[53]
Goto Islands, Japan	10-25.5	8-23	0.25-2	18	ADCP	[54]

One of the well-known experimental work on a lab-scale MCT model was conducted by Bahaj et al. [35] in 2007. The experimental data includes power and thrust of a HAMCT at different tip speed ratios and pitch angles. The max power coefficient, C_P is close to 0.43 at TSR 6. This study provided the details of blade geometry and was used as the basis of many followed numerical modeling. Lust [55] designed a 0.8m two-bladed HAMCT and conducted towing tank tests at US naval academy. A peak power coefficient of 0.43 was obtained at TSR 6.5 with a $Re_c = 4 \times 10^5$, where c is chord length at 0.7 radius of blade (R) measured from the center of rotation. Zhang et al. [56] studied the effects of turbine submerge depth on the wake characteristics. The authors collected and compared velocity components at different depths. Chernin et al. [57] proposed a probabilistic method to predict the cavitation of a tidal stream turbine. A case study illustrating the application of the new probabilistic approach as well as an

existing deterministic approach is presented. It is shown that the existing deterministic approach does not provide sufficient data for rationally and economically efficient design of tidal stream turbines for cavitation.

2.3.2 Numerical modeling

Numerical modeling is a good alternative to physical experiments, which are expensive and time consuming. Meanwhile, numerical modeling gives more details of flow field around turbine models. For example, the detailed loading on turbine blades obtained from numerical modeling can be used a reference for structural design of a marine current turbine. Flow separation at the suction side of blade is available in the post processing of numerical simulation, although it is hard to observe in the laboratory test. Numerical modeling can also be used in situations which are difficult for physical model tests, such as turbines operating in array, large size turbine models, scale effects. The categories of numerical methods include the Blade Element Momentum (BEM) method, BEM-CFD and CFD methods. These numerical models are presented in detail in the following sections.

2.3.2.1 BEM method

The BEM method is the simplest and fastest model among the three models mentioned above. The BEM method is a combination of momentum and blade element theories. Turbine blades are represented by a actuator disk. The sectional power and thrust are derived from tabulated lift and drag of airfoils (hydrofoils). The overall power and thrust are a result of integration from the blade root to its tip. The BEM theory greatly reduces the computational cost and is used as industrial standard for primary stage of turbine blade design. Due to the simplicity and reasonable accuracy, the BEM method has been widely used in the literature [15, 58–61]. Further details on the BEM method are given in Chapter 3.

2.3.2.2 BEM-CFD models

The BEM-CFD is a combination of the BEM and CFD methods, where the BEM method is used to model the turbine blade geometry, and the CFD is employed to calculate the physical quantities elsewhere in the computational domain. The forces of blade on fluid are incorporated into the source terms of the momentum equation of the CFD. This method provides more detail of fluid field, but less computational expensive than CFD models [62]. The BEM-CFD approach is mainly used for turbine array study, where geometry resolved method is too expensive for a number of turbines. Examples employing the BEM-CFD model are presented in references [63–66]. Masters et al. [66] used a coupled BEM-CFD model to evaluate the influence of flow acceleration on wake dynamics of a marine current turbine. The numerical results of performance gave good accuracy when compared against laboratory data.

2.3.2.3 CFD models

Although the BEM and BEM-CFD models provide reasonable accuracy for the performance and thrust of MCTs, the CFD models are a more comprehensive method and give more details of flow field around MCTs. The CFD models can be classified into inviscid

flow models and viscous flow models. Examples of inviscid flow model include lift line, vortex lattice, etc. The inviscid flow models assume inviscid, irrotational onset flows, which reduces the computational resource when compared with the viscous flow models. However, the inviscid flow models neglect viscous effects and do not address the blade stall and post stall problems.

Among viscous flow models, the most widely used turbulence model is the solution based on the Reynolds-Averaged Navier-Stokes (RANS) Equations. Recently, many numerical simulations of a MCT used the RANS-based turbulence models [67–70]. The moving reference frame (MRF) and sliding mesh are used to account for the rotation of the blade. Rahimian et al. [71] compared the effect of different turbulence models on performance of a two bladed turbine model. These numerical results were compared with experimental data, and concluded that the $K-\omega$ RANS model with wall function and the MRF was recommended for steady study of a MCT.

In the turbulence modeling, relative turbulence parameters are need to be specified at inlet boundaries of the computational domain. Normally, a low turbulence intensity(TI) is used for modeling a MCT in a steady current. Although the RANS is accurate enough for the performance in terms of C_P and C_T, it can not distinguish the effect of turbulence length scale in the wake recovery region [72]. More details on the CFD-RANS method as used in this study are given in Chapter 3.

2.4 Unsteady study of HAMCTs

For on-site marine current turbines, the flow is always unsteady and turbulent. The components of unsteadiness include high level of turbulence in the current, wave current interaction, pitch angle change of blades. Although steady assumption of flow simplify the analysis process and the resultant integral quantities such as mean performance and thrust provide valuable datasets for on-site turbines, more accurate unsteady simulations are need for better and more realistic predictions of performance and loading.

For turbine array study, unsteady inflow conditions at realistic array spacing requires preservation of turbine wakes over a sufficiently large range, standard CFD software is not feasible [73].

2.4.1 Wave effect on marine current turbine

Although the theory behind gravity waves is well known [74], not much attention has been given for their effects on MCTs until recently. Barltrop et al. [36] used linear wave theory, the Blade Element Momentum (BEM) approach and towing tank to investigate the effect of free surface waves on a model turbine of a three-blades HAMCT. A similar approach was used by Galloway et al. [37]. Both concluded that the time-averaged power coefficient is not much affected by the free surface waves, but high unsteadiness can occur in the blade loading that may affect its long-term structural integrity. More dependence was found on the wave's frequency than the wave's amplitude and form. Lunzik et al. [14] also used towing tank experiments to investigate the effect of small amplitude free surface waves on a small scale three-blades HAMCT. They concentrated on an "intermediate" wave length of about $h/\lambda = 0.34$, where h is the undisturbed water's depth and λ is the wave length. They also found a small effect on the time-averaged power coefficient C_P of the turbine, but time fluctuations were found, matching the passing of the wave's crest and trough over the turbine. Lust et al. [13] pursued towing tank experiments

for a small scale two-blades HAMCT and used computations based on the BEM model. They concentrated on linear surface waves over deep water with waves of amplitude of up to 0.2 m. They actually found a mild improvement in the time-averaged Cp of a high tip-speed-ratio (TSR) due to increase in the coefficient of thrust (drag) C_T. Increase in Cp as the wave's crest passed over the MCT and decrease as the trough passed was also confirmed. Reasonable agreement was found with the BEM calculations. Bai et al. [75] used the Large Eddy Simulation (LES) approach, where the fluid flow was coupled with a three blades rotor using the immersed boundary method. Good agreement was found with experimental results, showing complex turbulent wake behind the rotor. Small effect was found for the free surface as no surface waves were imposed although the free surface was allowed to move. A lab experiment was conducted to study the influence of turbulent inflow condition on Cp for a axial flow hydro-kinetic turbine. spectra analysis shows that the effect of turbulent inflow on Cp is valid in low frequencies [76].

There is several research on the wave effect on the turbine's performance and wake behind the rotor, such as Bai et al. [75], Kolekar and Banerjee [77] and Riglin et al. [78]. The effect of Froude number on power performance of micro-hydrokinetic turbine has been studied by Riglin et al. [78]. During sub-critial flow, the wave effect is not effective, while the power coefficient drops about a third in critical flow. Maximum power coefficients are similar between propeller-shaped turbine and traditional turbine, but the best TSR of propeller-shaped turbine is lower than that of traditional turbine.

A scale model of kite-like turbine is tested in a circulating water channel with linear wave generator [79]. The turbine was placed at different depths below the mean water level to analysis the wave impact on mooring line tension. The results show that thrust of turbine is influenced by surface wave when the nacelle depth is half wave length, but not the case when the hub depth is slightly greater than the wavelength. A spike-like variation of the stream-wise and vertical force on mooring line is observed for the 3 MW case, while a sinusoidal motion is observed for the 10 MW case. The experiment shows that wave amplitude and nacelle depth are important parameters for design of mooring system. Noruzi et al. studied the effect of installation depth on performance of turbine using BEM and CFD [15]. More fluctuating of torque was observed when the turbine was placed closer to the surface. They concluded that the linear wave had great impact on the performance of turbine when the ratio of the installation depth to water depth was below 0.2.

2.4.2 Wake

Turbine wakes are important when marine current turbines are in arrays [62]. Hu et al. [80] analyzed the effect of inflow conditions on wake using towing tank and OpenFOAM. Actuator line method is used to represent the blade geometry. The numerical result shows asymmetric wake when inflow condition is turbulent. The wake recovery of two model horizontal-axis tidal stream turbines was measured in a laboratory flume with Particle Image Velocimetry [81].

2.4.2.1 Park wake model

Park wake model, one of the earliest wake models, was proposed by Jenson [82] in 1983. It is widely used for the wind farm power prediction due to its simplicity, reasonable accuracy, and easy implementation. Generally, the Park wake model is valid for down-stream distances of three rotor diameters (3D) or more [83]. A linear expansion of wake

and uniform axial velocity are assumed in the Park model. An empirical wake expansion rate, k, is used in the calculation of induced velocity. The recommended value of k is 0.04 [84] and 0.075 for offshore and land wind farms, while these values may not suitable for marine current turbine. For a marine current turbine operating in a wake region, a turbulence intensity dependent k was recommended by Pyakurel et al. [85]. A joint Jensen/Ainslie approach was proposed to calibrate the k using the center line velocity and thrust from CFD results. The calibrated k values are 0.0325 (TI=3%), 0.0477 (TI=6%), and 0.0679(TI=9%) However, this correction is less accurate because the wake shape behind an isolated marine current turbine normally forms a Gaussian shape distribution, and the axial mean velocity is minimum at the center line. Calibration based on area-averaged axial mean velocity will be a better option.

2.5 Dual-rotor turbines

In 1983, Newman [86] pursued an analytical study on a dual-disc kinetic turbines based on the actuator disc theory, and concluded that the maximum power coefficient could be 16/25, which is 8% higher than Betz limit (16/27). In Newman's model (Fig. 2.4a), two same diameter discs are in tandem layout which are enclosed by two stream tubes. The control volume is decomposed into two stream tubes which are independent from each other. The 1D linear momentum is applied to both stream tubes and the fluid across discs is assumed to be inviscid, incompressible, and steady. Same velocity deficit is assumed in both stream tubes of the front rotor, but the velocity induction factors are different in the far wake of rear disc. Three years later, Newman extended his dual-disc model to multiple actuator-disc model, and concluded that the optimal C_P is $8n(n+1)/[3(2n+1)^2]$ for n disc in tandem. The maximum C_P is 2/3, which is 13% higher than the maximum C_P of the single actuator disk model [87]. A more recent update of the dual-disc model based on the 1-D momentum theory was done by Sundararaju et al. [88], whose proposed no assumption on airflow pressure in between the rotors (Fig.2.4b). Based on his model, The maximum C_P is 0.814 with a rotor spacing of 2.8 times of rotor diameter.

In the above mentioned analysis, the rotational relations between the front and rear rotors are not specified. There are two types rotational relations, co-rotating and counter-rotating, respectively. Mycek et al. [89] pursued experimental tests on two co-axial turbines rotating in the same direction in the IFREMER flume tank. The effects of two independent variables, turbulence intensity and rotor spacing, were studied. At low turbulence intensity level (3%), the maximum power coefficient of rear rotor was only about half of the power coefficient of single rotor, while the maximum power coefficient of rear rotor could reach roughly 80% of the single rotor when the turbulence intensity level was high (15%). As rotor spacing increased, the maximum power coefficient of rear rotor increased as well. The optimum TSR was as low as 2 at low rotor spacing (X<4D) and low turbulence intensity level (3%).

For counter-rotating dual-rotor turbines, both rotors were optimally pitched towards the upstream direction and counter rotating configuration sought to reduce swirl flow losses that are important for the two discs are close to each other (X/D<2). The performance of a counter rotating wind turbine (CRWT) is evaluated by several methods, including the blade element momentum (BEM) theory, actuator line model [90, 91], free-wake vortex lattice method [92] and CFD [91]. The wake velocity behind the front rotor is evaluated using the experimental wake data [93] or wake models. Several in-site exper-

iments on CRWT prototypes [93–95] were conducted for the validation of theoretical and numerical results. Parametric studies including pitch angles [96], rotor spacings [88], rotor diameter ratios [93], and rotational speed control for rotors have been reported. Cho et al. [94] proposed an integrated control algorithm for a counter-rotating dual rotor/dual generator wind turbine configuration. For a CRWT operating in an isolated environment, the full-scale prototype tests [93,94] showed that the maximum C_P of a CRWT was close to 0.5. For a wind farm, the numerical results from Vaselbehagh [91] showed that the dual-rotor turbines produced 22.6% more power than the single-rotor turbines.

In the field of a counter rotating MCT, Charke [97] and Huang [5] pursued numerical and experimental tests for rotors with a small rotor spacing as seen in Fig. 2.5 ($X/D < 0.5$, X is the rotor spacing, and D is the rotor diameter). Charke used a modified BEM theory to evaluate the performance of the turbine, and conducted a towing tank test, resulting a peak C_P of 0.39. Huang designed a counter rotating turbine composed of NACA0015 and MEL002 hydrofoil with rotor spacing of 0.1D . However, a poor agreement on C_P was observed between the numerical and experimental results. Meanwhile, a scattered C_P was observed in the experimental results. Huang [98] designed a dual-rotor counter rotating horizontal axis MCT pitched in opposite direction with a close rotor spacing ($X/D < 0.5$). However, the overall C_P of the dual-rotor turbine was still below 0.4.

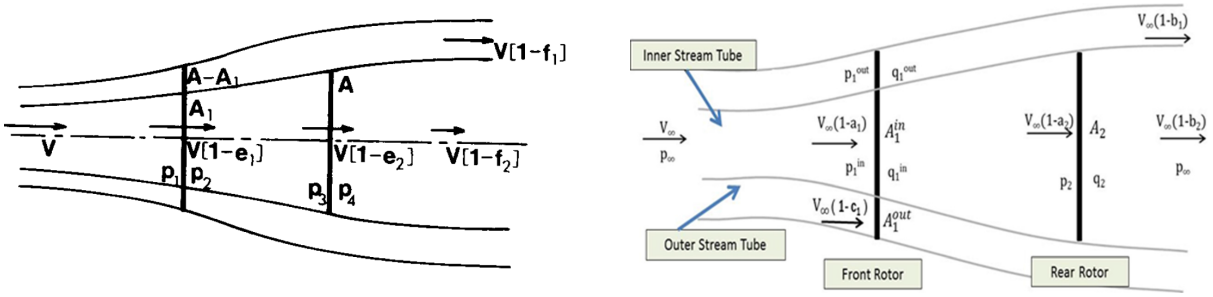

(a) Newman's model [86]

(b) Sundararaju's model [88]

Figure 2.4: Actuator disc models for dual rotor in tandem

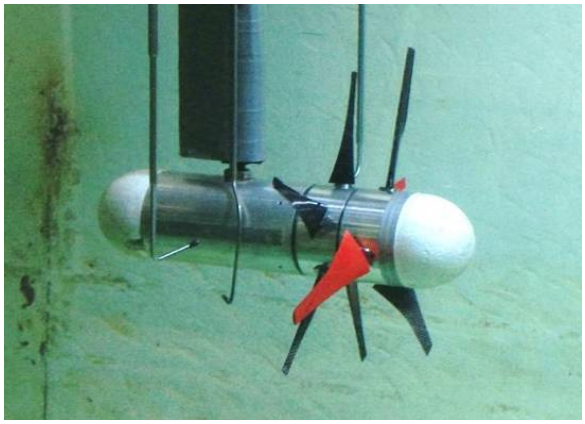

(a)

(b)

Figure 2.5: Counter-rotating MCTs [5, 6]

2.6 Summary

A review was given to the emerging importance of tidal power and in particular the marine current turbine that extracts the kinetic energy from tidal currents. The advantages of such device are that the direction of tidal current is well known in advance, the water density is much higher than its air's counterpart yielding a higher energy density than air, and the technology from wind power can be adopted and used in tidal power. However, the marine current turbine also exhibits unique challenges in terms of dealing with unsteadiness caused by the free surface waves, the reversing direction of the tidal current, availability of suitable sites. installation and access. For this purpose, the various forms of MCTs were reviewed as well as methods of prediction from the rapid BEM approach to the computationally demanding CFD approaches. The use of dual rotor and effects of free surface were also reviewed as they will related to the studies in Chapters 5 and 6.

Chapter 3

Computational hydrodynamic methodology

3.1 Introduction

Two computational approaches were used in this study: the Blade Element Momentum (BEM) method and Computational Fluid Dynamics (CFD). For the BEM, both the steady (classical) model and the unsteady model were used. For CFD, RANS and unsteady RANS were used through the ANSYS Fluent software. Both approaches, their models' advantages and disadvantages are described in the following sections.

3.2 Rapid solvers for a HAMT in free space

3.2.1 The steady BEM method

The actuator disk model was first described by Rankine in 1865 [99]. Later, the blade element theory was developed by Froude in 1898. Based on actuator disk model, the maximum power coefficient (16/27) was derived by Lanchster and Betz in 1920 [100]. The fully developed blade element momentum (BEM) was described by Glauert in 1935 [101]. The essence of the steady blade element momentum (BEM) is a combination of the blade element method and 1D momentum theory. The Glauert's BEM has several assumptions:

- The mean flow is steady
- An rotor has infinite number of blades
- The flow is axially symmetric
- No radial interdependence between annular control volumes

To calculate forces on a rotor with a finite number of blades, a tip correction was introduced by Prandtl in 1926. Goldstein [102] further developed induction factor calculation based on vortex wake in 1929. At first, the BEM approach was used in the propeller field. After the oil crisis in 1980s, the wind energy attracted attentions from all works of life and the BEM theory was transformed into the wind energy field. Later development of the BEM theory has gone through several modifications to improve its accuracy [7]. This includes semi-empirical expressions for hub and tip losses [103], post-stall profile

Figure 3.1: The ring-shaped control volume in the BEM model(a) [7], and the velocity vector triangle at the blade profile (b).

hydrodynamics [104], stall delay due to rotational augmentation [105], and correction for the axial force for a turbulent wake [7].

In the BEM model, the control volume is discretized into numerous annular elements along the spanwise direction (Fig. 3.1a). For each annual control volume with a cross sectional area of $2\pi r dr$, the thrust and moment elements (dT, dM) on the annular control volume based on the 1D axial momentum and Euler's turbine equations are:

$$dT = (U_\infty - U_w)d\dot{m} = 2\pi r\rho U(U_\infty - U_w)dr \tag{3.1}$$

$$dM = rC_\theta d\dot{m} = 2\pi r^2 \rho U C_\theta dr \tag{3.2}$$

where, r is the radial distance, ρ is the density of fluid, U_∞ is the free stream velocity which is assumed to be perpendicular to the rotational plane, U_w is the axial velocity in the far wake region, U is the axial velocity in the blade rotational plane, C_θ is the rotational velocity in the wake region. Based on the 1-D actuator disk theory, the U_w and U are related to U_∞, as follows:

$$U_w = U_\infty(1 - 2a) \tag{3.3}$$

$$U = U_\infty(1 - a) \tag{3.4}$$

where a is the axial induction factor. The rotational velocity, C_θ, can be expressed using a tangential velocity induction factor, a', as written:

$$C_\theta = 2a'\Omega r \tag{3.5}$$

Substituting Eqs.(3.3)-(3.5) into Eqs.(3.1) and (3.2), new expressions for dT and dM are derived as below:

$$dT = 4\pi r\rho U_\infty^2 a(1 - a)dr \tag{3.6}$$

$$dM = 4\pi r^3 \rho U_\infty \Omega(1 - a)a'dr \tag{3.7}$$

where Ω is the angular velocity of the rotor, and dr is the annulus width.

In the steady BEM approach the rotor disk is taken as infinitesimally thin, divided to rings and the momentum theory is used to calculate the axial force and torque for each

ring assuming axial and tangential induced velocity factors a and a' due to the blade motion, as seen in Fig. 3.1b. For the relative velocity seen by a blade element, the axial velocity is $U_\infty(1-a)$, while the tangential velocity is $\Omega r(1+a')$. The inflow angle (ϕ) , local angle of attack (α) and local pitch of blade(θ) are related in the following expression:

$$\tan\phi = \frac{(1-a)U_\infty}{(1+a')\Omega r} \tag{3.8}$$

$$\alpha = \phi - \theta \tag{3.9}$$

Then, thrust and moment elements can be derived from 2D airfoil aerodynamics.

$$dT = \rho B \frac{U_\infty^2(1-a)^2}{2sin^2\phi} c C_n dr \tag{3.10}$$

$$dM = \rho B \frac{U_\infty(1-a)\Omega r(1+a')}{2\sin\phi\cos\phi} c C_t r dr \tag{3.11}$$

and

$$C_n = C_L cos\phi + C_D sin\phi \tag{3.12}$$

$$C_t = C_L sin\phi - C_D cos\phi \tag{3.13}$$

Where C_L and C_D are the lift and drag coefficients of the blade's profile, B is the number of blades, C_n and C_t are the axial and tangential force coefficients.

The axial and tangential induction factors can be derived when combining the thrust and moment from 1D momentum and blade element theories, namely Eq. 3.6 , Eq. 3.7, 3.10 and 3.11.

$$a = \frac{\sigma C_n}{4\sin^2\phi + \sigma C_n} \tag{3.14}$$

$$a' = \frac{\sigma C_t}{4\sin\phi\cos\phi - \sigma C_t} \tag{3.15}$$

However, C_L and C_D depend on the angle of attack, α, and θ is the known pitch angle of blade profiles, but it has to be found from Eq.3.8. This yield two non-linear equations for a and a'. These can be resolved using a linear iterative solver, i.e. assuming initial guess for a and a' (usually zero). Finding ϕ from Eq.3.8, than finding α, leading to C_L and C_D from the known hydrodynamics of the profile. This leads to C_n and C_t which are used to find the new a and a' from Eqs.3.14 and 3.15. These a and a' are used in the new iteration until convergence is achieved for a and a'. The total thrust and moment of the blade are the integration result of all elemental thrust and moment (Eqs.3.10& 3.11), where a,a',C_n and C_t are functions of r.

The above thrust and moment coefficients do not include correction effects. As the BEM theory assumes infinite number of blades in the control volume, the Prandtl's tip loss factor,F, is used for dT and dM corrections, as written:

$$dT = 4\pi r\rho U_\infty^2 a(1-a)F dr \tag{3.16}$$

$$dM = 4\pi r^3 \rho U_\infty \Omega(1-a)a' F dr \tag{3.17}$$

and:

$$F = \frac{2}{\pi} cos^{-1}(e^{-f}) \tag{3.18}$$

$$f = \frac{B(R-r)}{2rsin\phi} \tag{3.19}$$

Another correction named Glauert correction is used when axial induction factor,a, is larger than 0.4, where assumptions of actuator disk theory are not valid (Fig.3.2a). Glauert derived an empirical relations between the C_T and a, as follows:

$$C_T = \begin{cases} 4a(1-a)F & a \leq \frac{1}{3}, \\ 4a[1-\frac{a(5-3a)}{4}]F & a > \frac{1}{3}. \end{cases} \tag{3.20}$$

The main results are the coefficients of thrust and power (C_T, C_P). This axial force is commonly noted as thrust due to the propeller implication, although it points at the flow direction for the turbine and thus physically it is a drag force. Once the axial and tangential induction factor a and a' are found per blade segment then C_T and C_P can be found by integrating the expressions given by the blade-element theory or the momentum theory along the blade span as given in the following for C_P from the momentum theory:

$$dC_P/dr = 8(TSR)^2[1-a(r)]a'(r)f(r) \tag{3.21}$$

where TSR is the tip speed ratio, and $f(r)$ is the blade and hub tip corrections decaying from one to zero at the vicinity of the blade's tip and hub. Fig.3.2b shows the relations between the power coefficient and the axial induction factor. It illustrates that a rotor has the potential extract power from the flow if a varies from 0 to 1. A similar expression can be driven for dC_T/dr by the momentum theory to be replaced by Glauret's correction for turbulent wake at $a > 0.34$ [7].

The steady BEM used in this thesis is from the classic BEM model of Glauert [101]. Due to the reasonable accuracy and low computational cost, the Blade Element Momentum (BEM) method has become the industrial standard for power estimation of wind turbines [7, 42, 106] .

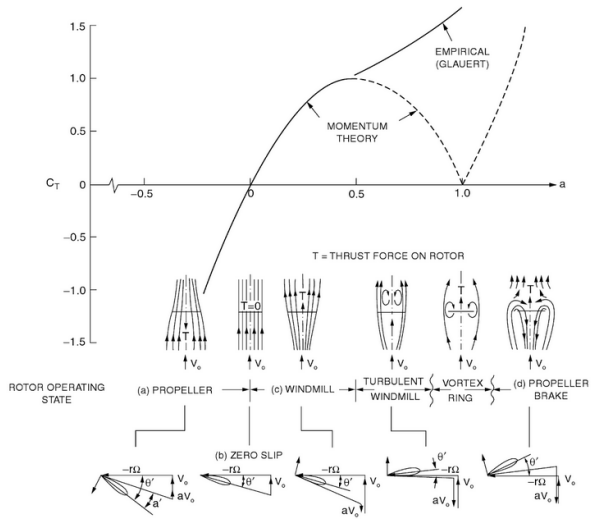

(a)

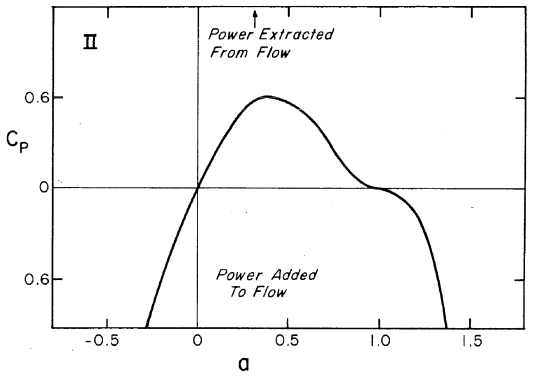

(b)

Figure 3.2: Thrust (a) and power (b) coefficients versus axial induction factor [8, 9]

3.2.2 The unsteady BEM method

Due to ocean water turbulence, wind-generated waves and presence of the supporting structure for marine current turbines, the mean velocity seen by the rotor is inherently unsteady. For a more realistic evaluation of the performance and fatigue of marine current turbines, an unsteady calculation is needed. Fig.3.3 shows the local velocity triangle on a blade profile in a non-inertial coordinate system rotating the same speed with the rotor. The free stream velocity, U_∞, is no longer assumed to be normal to the rotational plane and can changes with time . The local angle of attack can be computed if the induced velocity is known. The essence of the unsteady BEM is to calculate the induced velocity, W, at every time step.

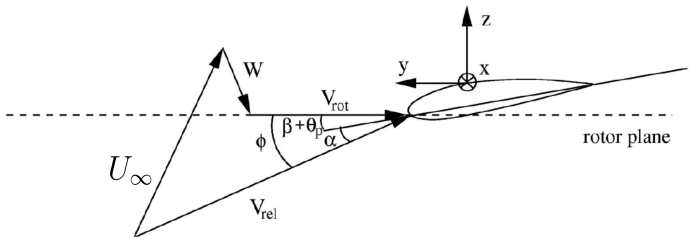

Figure 3.3: The local velocity triangle seen by a blade profile [7]

Basically, the unsteady BEM accounts for the time delay in the rotor response to changes in flow conditions such as the free stream velocity, U_∞, wind-generated waves, and the blade's pitch angle, θ.

The TUDK dynamic model [105] developed for wind turbines was mostly used in this thesis. For a correctly oriented turbine, i.e. the rotor plane is normal to the free stream velocity, U_∞, Oye's model [107] was used as follows:

$$W_{int} + \tau_1 \frac{dW_{int}}{dt} = W_{qs} + k \cdot \tau_1 \frac{dW_{qs}}{dt} \tag{3.22}$$

$$W + \tau_2 \frac{dW}{dt} = W_{int} \tag{3.23}$$

Where W_{qs} is the induced velocity (either axial or tangential) found by the steady BEM method described in the previous section. W is the induced velocity corrected by the dynamic wake, replacing $-aU$ and $\Omega r a'$ of Fig.3.1b in the axial and tangential directions. In the above equations, the time constants $\tau_1$and τ_2 are defined as:

$$\tau_1 = \frac{1.1}{1 - 1.3a} \cdot \frac{R}{U_\infty} \tag{3.24}$$

and

$$\tau_2 = (0.39 - 0.26(\frac{r}{R})^2)\tau_1 \tag{3.25}$$

Where R is the rotor's radius, $k = 0.6$ and a is the axial induction factor, which we took from the steady BEM. One should note that a should not be allowed to exceed 0.5, pointing to the validity of the TUDK model or wind mill state. When the axial induction factor, a, is larger than 0.5, the velocity in the far wake region, $U_w = U_\infty(1 - 2a) < 0$ (Eq.3.3), implying a reverse flow in the far wake. This is out of the validity of the BEM theory.

Equations 3.22 and 3.23 were solved as follows; At $t = 0$, W_{qs} was solved using the steady BEM method and dW_{qs}/dt was zero. At later time stages, dW_{qs}/dt was estimated as $(W^i_{qs} - W^{i-1}_{qs})/\Delta t$ where i is the time stage index and Δt is the time step. Thus equation 3.22 can be solved as:

$$W^i_{int} = H + (W^{i-1}_{int} - H)exp(\frac{-\Delta t}{\tau_1}) \tag{3.26}$$

and

$$H = W^i_{qs} + k \cdot \tau_1 \frac{W^i_{qs} - W^{i-1}_{qs}}{\Delta t} \tag{3.27}$$

Then, Equation 3.23 is solved as:

$$W^i = W^i_{int} + (W^{i-1}_{int} - W^i_{int})exp(\frac{-\Delta t}{\tau_2}) \tag{3.28}$$

At $t = 0$ and earlier, W^i and W^i_{int} are taken as identical as $W^{i=0}_{qs}$. It can be easily seen that if there are no changes in the flow condition, $dW_{qs}/dt = 0$ and $W^i = W^i_{qs}$, then the TUDK model converges to the steady BEM method.

A second and simpler method was provided by Garad & Hassen (GH) that was originally developed for helicopters and later adapted to the wind turbine [105]. It involves a first order in the equation for the axial induction factor, a. However, the TUDK model was found to provide better agreement with the experimental results of free surface effect in Chapter 6 and thus not described in detail here. The interested reader is referred to reference [105].

Another important is stall and post-stall behavior. The small scale turbine mainly investigated in this study has a low curvature and rounded noise profile as the E387 profile. This results in a leading edge short bubble stall, where the leading edge bubble bursts at high angle of attack, leading to massive flow separation over the suction side of the profile and stall. To account for this and post stall characteristics, the semi empirical formulas of C_L and C_D were incorporated from references [104, 105]. They converges to Hoerner's [108] empirical estimates of $C_L = sin2\alpha$ and $C_D = 1.3sin^2\alpha$ for $\alpha > \alpha_{stall}$. High chamber profiles experience stall of trailing edge separation which is much greater than the leading edge stall. For such profile, S. Oye developed a dynamic stall model as follows [107]:

$$C_L = f_s C_{L,inv}(\alpha) + (1 - f_s)C_{L,fs}(\alpha) \tag{3.29}$$

Where, $C_{L,inv}$ is the lift coefficient for inviscid flow without flow separation, and $C_{L,fs}$ is the lift coefficient for full separated flow,i.e. $sin2\alpha$. f_s is a separation function and is modified for dynamic stall response as follows:

$$f_s(t + \Delta t) = (f^{st}_s + (f_s(t) - f^{st}_s)exp(-\frac{\Delta t}{\tau}) \tag{3.30}$$

Where f^{st}_s is the value of f_s when static aerofoil data is applied in equation 3.29. τ is a time constant and equal to $4 \cdot c/U_{rel}$, where c is the local chord length, U_{rel} is the relative velocity seen by the blade profile. high curvature profiles are more common in large kinetic turbines and hence for the model turbine investigated in Chapters 4, 5, 6, leading edge stall was experienced as already noted. Hence, this dynamic stall model effect was found to be very small.

3.3 CFD

3.3.1 Governing equations

The basic governing equations for water flow modelling are continuity, and momentum equations. The continuity equation in index form is as follows:

$$\frac{\partial \rho}{\partial t} + \frac{\partial \rho u_i}{\partial x_i} = 0 \tag{3.31}$$

Where u_i is the i component of velocity vector, and the Einstein notation is used(i=1,2,3).

The momentum equation is derived from Newton's second law which states that net forces on a material region equals to rate of change of momentum on that.

The momentum equation which only includes body force is as written:

$$\frac{\partial \rho u_i}{\partial t} + \frac{\partial \rho u_i u_j}{\partial x_j} = -\frac{\partial p}{\partial x_i} + \frac{\partial T_{ij}}{\partial x_j} + \rho g_i \tag{3.32}$$

and

$$T_{ij} = \mu(\tau_{ij}^s - \frac{2}{3}\mu\delta_{ij}\frac{\partial u_j}{\partial x_j}) \tag{3.33}$$

where p is the pressure, and T_{ij} is the stress tensor,τ_{ij} is the viscous stress tensor and δ_{ij} is the Kronecker delta which is defined as:

$$\delta_{ij} = \begin{cases} 0 & \text{if } i \neq j, \\ 1 & \text{if } i = j. \end{cases} \tag{3.34}$$

For incompressible flows, the density, ρ, is constant ($D\rho/Dt = 0$). As for water flow, the governing equations are simplified as follows:

$$\frac{\partial u_i}{\partial x_i} = 0 \tag{3.35}$$

$$\rho\frac{\partial u_i}{\partial t} + \rho\frac{\partial u_i u_j}{\partial x_j} = -\frac{\partial p}{\partial x_i} + \frac{\partial T_{ij}}{\partial x_j} + \rho g_i \tag{3.36}$$

The continuity and momentum equations are non-linear partial differential equations. The effect of the g is important only for the free surface wave in our cases.

3.3.2 Turbulence models for RANS equations

The basic concept in RANS is the Reynolds averaging where instantaneous flow quantities u, v, w, p are decomposed into mean parts U, V, W, P and fluctuating parts $u', v', w', p',$, etc. For example, the instantaneous velocity could be decomposed into two parts:

$$u_i = U_i + u_i' \tag{3.37}$$

Where u_i is the instantaneous velocity, U_i is the mean (emsemble averaged or time averaged) velocity, and u_i' is fluctuating part. Similarly, the instantaneous pressure,p could be split as the mean pressure, P and the fluctuating pressure,p':

$$p = P + p' \tag{3.38}$$

The Reynolds averaged Navier Stokes equations are derived from time averaging of both sides of the instantaneous mass and momentum equations. They can be written in conservation form as [109]:

$$\frac{\partial U_i}{\partial x_i} = 0 \tag{3.39}$$

$$\rho\frac{\partial U_i}{\partial t} + \rho U_j\frac{\partial U_i}{\partial x_j} = -\frac{\partial P}{\partial x_i} + \frac{\partial}{\partial x_j}(2\mu S_{ji} - \rho\overline{u_j' u_i'}) \tag{3.40}$$

For the steady RANS, $\partial U_i/\partial t = 0$. The Reynolds averaged continuity equation is the same as instantaneous continuity equation except that the instantaneous velocity is replaced by time averaged velocity. In the momentum equation, the instantaneous velocity is also replaced by time averaged velocity, but a new term ($\rho\overline{u_j' u_i'}$) is generated, which represents the effects of turbulence. The term $-\rho\overline{u_j' u_i'}$ is named Reynolds stress tensor, and thus the equations not closed, which can be solved using turbulence models. Typical turbulence models for RANS include eddy viscosity models (EVM) and Reynolds stress transport models (RSM).

3.3.2.1 Eddy viscosity models for RANS

In 1887, J. Boussinesq [110] introduced the concept of eddy viscosity, which was inspired by the idea that the momentum transfer caused by the molecular motion in a gas can be described by a molecular viscosity. The Boussinesq assumption states that the Reynolds stress tensor is proportional to the trace-less mean rate-of-strain tensor, and can be written as:

$$-\rho\overline{u_i' u_j'} = \mu_t\left(\frac{\partial u_i}{\partial x_j} + \frac{\partial u_j}{\partial x_i} - \frac{2}{3}\frac{\partial u_k}{\partial x_k}\delta_{ij}\right) - \frac{2}{3}k\delta_{ij} \tag{3.41}$$

The Boussinesq eddy viscosity approximation is the basis of all eddy viscosity models. The eddy viscosity concept, along with the mixing length hypothesis become the cornerstone for almost all turbulence modeling research [46]. In Fluent, the Boussinesq hypothesis is used in the Spalart-Allmaras model, the $k-\epsilon$ models, and the $k-\omega$ models [10].

In the following section, only two-equation turbulence models are briefly introduced as they are used in this thesis. For other models, the interested reader may refer to number of references, such as [10, 46, 111]. In two-equation turbulence models, two transport equations are used to obtain the turbulent length and time scales. Typical two-equation turbulence models include $k-\epsilon$ models and $k-\omega$ models. The standard $k-\epsilon$ model was proposed by Launder and Spalding [112], and becomes popular for practical engineering flow simulations due to its robustness, economy and reasonable accuracy. This model assumes that the flow is full turbulent, and the influences of molecular viscosity are negligible [10]. In the standard $k-\epsilon$ model, two transport equations are used to obtain the turbulence kinetic energy (k) and its dissipation rate (ϵ). For incompressible flow without any source term, the transport equations for $k-\epsilon$ model are:

$$\frac{\partial}{\partial t}(\rho k) + \frac{\partial}{\partial x_i}(\rho k u_i) = \frac{\partial}{\partial x_j}\left[\left(\mu + \frac{\mu_t}{\sigma_k}\right)\frac{\partial k}{\partial x_j}\right] + G_k - \rho\epsilon \tag{3.42}$$

$$\frac{\partial}{\partial t}(\rho\epsilon) + \frac{\partial}{\partial x_i}(\rho\epsilon u_i) = \frac{\partial}{\partial x_j}\left[\left(\mu + \frac{\mu_t}{\sigma_\epsilon}\right)\frac{\partial \epsilon}{\partial x_j}\right] + C_{1\epsilon}\frac{\epsilon}{k}\left(G_k+\right) - C_{2\epsilon}\rho\frac{\epsilon^2}{k} \tag{3.43}$$

where G_k is the generation of turbulence kinetic energy due to the mean velocity gradients, σ_ϵ and σ_k are the turbulent Prandtl numbers for ϵ and k, and $C_{1\epsilon}$, $C_{2\epsilon}$, $C_{3\epsilon}$ are constants. The eddy viscosity, μ_t, is related to k and ϵ as follows:

$$\mu_t = \rho C_\mu \frac{k^2}{\epsilon} \tag{3.44}$$

The standard $k-\epsilon$ model is a semi-empirical model, and its further development include the RNG $k-\epsilon$ model and the realizable $k-\epsilon$ model.

Similar as the standard $k-\epsilon$, the standard $k-\omega$ model include two transport equations for the turbulence kinetic energy and the specific dissipation rate, ω. In ANSYS Fluent, the Wilcox's $k-\omega$ model [46] is used as the default standard $k-\omega$ model. For incompressible flow without any source term, the governing equations of k-ω model are as follows [10]:

$$\frac{\partial}{\partial t}(\rho k) + \frac{\partial}{\partial x_i}(\rho k u_i) = \frac{\partial}{\partial x_j}(\Gamma_k \frac{\partial k}{\partial x_j}) + G_k - Y_k \tag{3.45}$$

$$\frac{\partial}{\partial t}(\rho \omega) + \frac{\partial}{\partial x_i}(\rho \omega u_i) = \frac{\partial}{\partial x_j}(\Gamma_\omega \frac{\partial \omega}{\partial x_j}) + G_\omega - Y_\omega \tag{3.46}$$

where k is the turbulence kinetic energy, ω is the specific dissipation rate. G_ω represents the generation of ω. Γ_K and $\Gamma\omega$ represent the effective diffusivity of k and ω, respectively. Y_k and Y_ω represent the dissipation of k and ω due to turbulence. The turbulent viscosity, μ_t is computed by combining k and ω as follows:

$$\mu_t = \frac{\rho k}{\omega} \tag{3.47}$$

In the $k-\omega$ model, the low-Reynolds number terms are not recommended because these terms yield a delayed onset of the turbulent wall boundary layer. Meanwhile, the standard $k-\omega$ model is sensitive to free stream conditions. Further improvement of $k-\omega$ model include the baseline (BSL) $k-\omega$ model and the Shear-Stress Transport (SST) $k-\omega$ model introduced by Menter [113]. In the BSL $k-\omega$ model is a combination of both the $k-\epsilon$ model and $k-\omega$ model, where the free-stream independence of $k-\epsilon$ is implemented in the far field and the accurate formulation $k-\omega$ is used in the near wall region. This is achieved by a blending function. Further improvement of the BSL $k-\omega$ model yields the SST $k-\omega$ model, which explains the transport of the SST in the interpretation of the turbulent viscosity. Generally, the SST $k-\omega$ model is more reliable and precise for adverse pressure gradient flows, airfoils, transonic shock waves, compared with the standard and the BSL $k-\omega$ models [114]. In essence, the SST $k-\omega$ is a combination of $k-\omega$ and $k-\epsilon$ using a blending function.

3.4 Turbine modelling

The CFD modelling approaches for HAMCTs could be subdivided into two categories, namely geometry not resolved methods such as immersed boundary method,immersed

boundary method, and geometry resolved methods using moving reference frames or sliding meshes as implemented in ANSYS used in this study. The immersed boundary method involves embedding singularities around the moving body surface. These singularities force the flow velocity to the required body surface velocity as was done in Bai et al [75]. The BEM-CFD approach is a simplified variant of the immersed boundary method, where a line of singularities is laid along the span of the blade. The strength of these singularities is determined b the required C_L and C_D from the BEM method. The BEM-CFD method blends the BEM and CFD meothods, in which the rotor is treated as an actuator disk, blade element disk or actuator line, and CFD is employed to model the flow properties elsewhere in the domain [62, 64]. The main advantage of BEM-CFD model is that the computational cost is significantly reduced compared to geometry-resolved CFD models [60, 115]. One of the drawback of BEM-CFD models is that the angle of attack is relative to V_{rel} is not known, as V_{rel} is upstream of the profile not at the leading edge. The following looks at the two geometry resolved methods used in this study.

3.4.1 Multiple moving reference frames

The default reference frame is the inertial frame of reference. However, there are many cases where it is advantageous to use the moving reference frame. These cases normally involve moving parts, such as turbines, impellers and airplanes. The main advantage of using the moving reference frame (MRF) is to change unsteady flows in inertial reference frame into steady flows in MRF. For example, the rotating blade is unsteady in the inertial frame of reference. However, the blade is steady when the frame of reference is rotating with the blade. The velocity vector has different forms in the inertial and moving reference frames. The relationship between absolute velocity $\mathbf{v}$ (fixed observer) and relative velocity $\mathbf{v_r}$ (the velocity viewed from the moving frame) is as follows:

$$\mathbf{v_r} = \mathbf{v} - \mathbf{u_r} \tag{3.48}$$

where

$$\mathbf{u_r} = \mathbf{v_t} + \mathbf{\Omega} \times \mathbf{r} \tag{3.49}$$

where $\mathbf{v_t}$ is translational frame velocity, and $\mathbf{\Omega}$ is the angular velocity of rotor.

Additional acceleration terms are added into the Navier Stokes equations when the moving reference frame is used. The mass and momentum equations of fluid in a moving reference frame can be written as follows [10]:

$$\frac{\partial \rho}{\partial t} + \nabla \cdot \rho \mathbf{v_r} = 0 \tag{3.50}$$

$$\frac{\partial}{\partial t}(\rho \mathbf{v_r}) + \nabla \cdot (\rho \mathbf{v_r} \mathbf{v_r}) + \rho(2\mathbf{\Omega} \times \mathbf{v_r} + \mathbf{\Omega} \times \mathbf{\Omega} \times \mathbf{r} + \beta \times \mathbf{r} + \mathbf{e} = -\nabla p + \nabla \cdot \overline{\overline{\tau_r}} + \mathbf{F} \tag{3.51}$$

where $\mathbf{e} = d\mathbf{v_t}/dt$ and $\beta = d\mathbf{\Omega}/dt$.

In simplified cases, a single moving reference frame can be used for the whole domain of interest. For example, the single moving reference frame is good for HAMCTs modelling involving only the rotor. However, the single moving reference frame is not valid for other cases, such as HAMCTs involving the support tower, free surface waves, seabed, or different angular velocities for each HAMCT. For flows involving multiple moving parts, the domains of interest can be subdivided into several parts, with each part applied its

own moving reference frame. This is referred as multiple moving reference frames. Based on the treatment of the N-S equations at the interface, two sub-models of multiple moving reference frames are available, namely the multiple reference frame model and the mixing plane model.

Figure 3.4 illustrates the usages of a single moving reference frame and multiple moving reference frames on turbines. For the left turbine, a single moving reference frame can be applied to the entire domain. For the middle turbine, multiple reference frames are needed due to the existence of baffle. A moving reference frame can be applied in a domain enclosing the turbine, while the outside region is solved in inertial reference frame. For the right two turbines, a single reference frame is not enough if the two turbines rotate at different angular velocities. In such case, the computational domain must be divided into three sub-domains: an inertial frame outside both turbine regions and two independent moving reference frames on the two turbines.

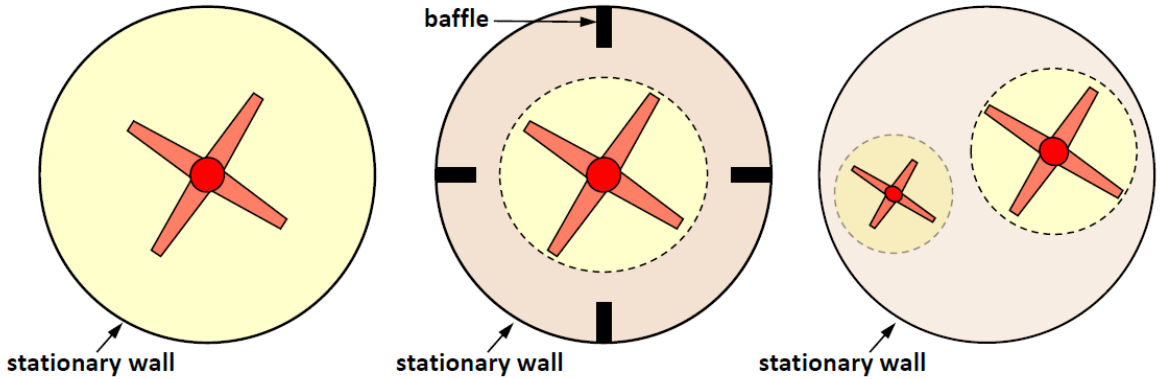

Figure 3.4: A single reference frame versus multiple reference frames [10]

3.4.2 The sliding mesh

The multiple moving reference frames provides a steady approximation of HAMCTs, where the computational domains are relative steady in the inertial reference frame. To obtain more realistic unsteady solution of flows, the relative motions of domains are needed. This can be achieved by the sliding mesh, and overset (chimera) mesh. Overset mesh is composed of computational domains with overlapping regions in physical space, while the sliding mesh consists of meshes with an non-conformal interface. The sliding mesh is a special case of dynamic mesh, in which the interface mesh does not change shape but do a rigid translational or rotating movement. Both the overset mesh and sliding mesh are good for unsteady modelling of HAMCTs with tower or in confined space, such as including free surface waves and the sea floor. The overset mesh is more flexible in meshing generation than the sliding mesh, however the overset mesh requires more computational resource. References [10, 116] show that both mesh methods give similar numerical results in terms of accuracy.

Figure 3.5 illustrates a sliding mesh with two cell zones and a non-conformal interface, which is represented by a solid line, *ac*. The nodes locations are not exactly the same on the boundaries of cell zone 1 and 2. The physical quantities in cell zone 1 and 2 are interpolated on the interface. The interface is regarded as interior zone when the interface

zone 1 and interface zone 2 are contacted, while a "wall zone" is generated when the two interface zones are separated due to relative mesh motion.

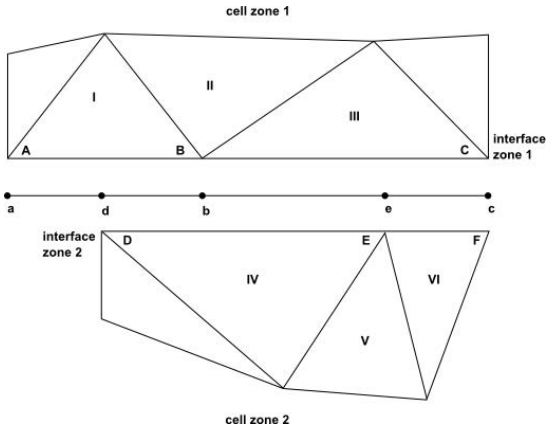

Figure 3.5: Schematic 2D non-conformal meshes [10]

3.5 Wave modelling

Typical free surface modelling methods are Eulerian method, Lagrangian method, and Mixed Eulerian-Lagrangian method. In this study, we used mainly the user defined functions (UDF) approach, i.e. mimicking the effect of the free surface wave by specifying a combination of wave and current velocities as inflow. Then the free surface is replace by a upper lid (symmetry boundary condition).

3.5.1 One phase approximation using UDF

Only steady fixed values can be specified in the default boundary conditions of Fluent. For time dependent and variable boundary conditions, these can be achieved by the UDF in Fluent. A UDF is a function written in C programming. User defined functions can provide boundary and cell zone conditions, material properties, and user-defined models,etc. The pre-defined marcos are used for data exchange between the UDF and the solver in Fluent [117]. UDFs can be either compiled or interpreted. The compiled UDFs are more efficient and recommended. Microsoft Visual C++ is the default compiler for Fluent on Windows OS, while any ANSI-compliant compiler is supported on Linux OS. The essence of one phase approximation is that the inlet boundary condition is specified by a user defined function representing the wave and current velocities seen by the rotor. The basic steps for defining a sine wave at inlet boundary condition is as follows:

1. Edit the sine wave velocity function in a text editor
2. Compile the UDF in the Fluent session
3. Hook the UDF to the inlet zone in boundary condition panel
4. Initialize and run the calculation
5. Examine the results

A wave velocity function specified at the inlet boundary is a good approximation for estimating the wave effect on HAMCTs. The two phase flow (water and air) is simplified into one phase flow (water only), which neglects the free surface motion and significantly reduces the computational cost.

Chapter 4

Hydrodynamic performance of the HAMT rotor in free space

4.1 Introduction

A tidal turbine blade is composed of profiles located along the span. The performance of tidal turbine is determined by several parameters such as the fluid property, tip speed ratio (TSR), blade shape and diameter. The blade design process normally involves proper parameters such as the airfoil shape at different station, twist angle, and chord length. For stall regulated tidal turbine,the operational TSR of tidal turbine changes due to the variation of inflow tidal current and wave speed, thus the tidal turbine operates at off-design TSR at most cases. In order to capture more power, it is important to maintain a relative high power coefficient at a wide range of TSR.

The purpose of this section is to study the surface curvature effect on the performance of a marine turbine. Hence, as in the previous study of a generic small wind turbine, a generic configuration of a marine current turbine is studied using the E387 profile and its CIRCLE re-designed profile noted as A7 [118]. Although such turbine has similarities to a wind turbine, there are also dissimilarities, such as a shorter aspect ratio of the blade and monotonic reduction in the blade chord length with the distance from the hub.

The BEM method and steady RANS are used to analysis the total performance and spanwise distribution of local angle of attack, streamline, lift to drag ratio of the E387 turbine [14] and redesigned A7 turbine at different operation conditions.

4.2 BEM and RANS analysis of HAMT rotor

4.2.1 Blade Geometry

A laboratory scale turbine model [14] (denoted as E387 turbine) was chosen for this study because the turbine model is composed of Eppler 387 profile which has been redesigned using the CIRCLE method [11]. The chord length and twist angle distributions along spanwise direction are illustrated in Fig. 4.1. The CAD model of the turbine (Fig. 4.2a) is created with commercial software *Solidworks*®.

The surface discontinuity of the E387 profile is removed using the CIRCLE method [11, 118, 119]. The redesigned airfoil is named A7. The coordinate and curvature distribution of E387 and A7 airfoils are presented in Fig. 4.3. Fig. 4.4 show the lift and drag coefficients of the E387 and A7 profiles at different angle of attack. A redesigned A7

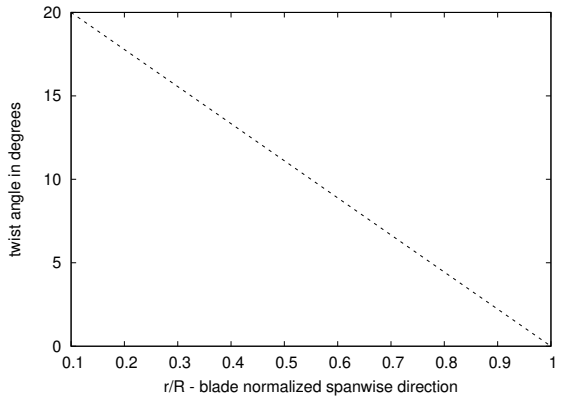

(a) Blade twist angle distribution along spanwise direction

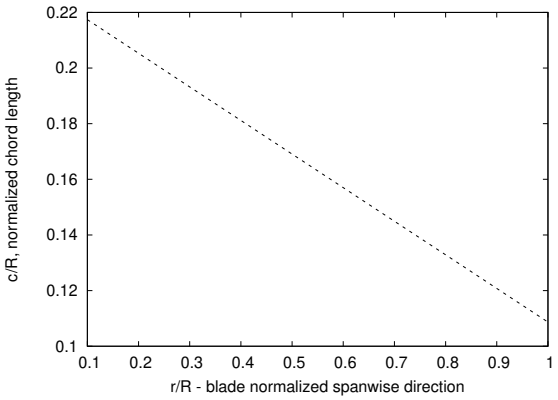

(b) Blade chord length distribution along spanwise direction

Figure 4.1: Chord length and twist angle distribution of the experimental turbine model

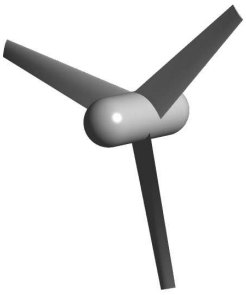

(a) Numerical geometry of the turbine

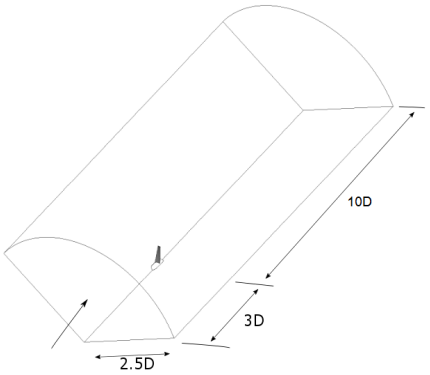

(b) Computational domain

Figure 4.2: Geometry and Computational Domain

turbine is obtained by replacing the original E387 airfoil at each blade station while keeping all other parameters the same.

4.2.2 Numerical Modelling Methods

The E387 airfoil is designed as a sharp trailing edge.The shape trailing edge does not exist in experimental model due to structural constraints and leads to skewed mesh in numerical modelling. Normally there are two methods to deal with the sharp trailing edge. One method is to simply cut the trailing edge, which decreases the chord length and changes the thickness to chord length ratio. Another and a better method is to thicken the trailing edge. Thickened trailing edge keeps the ratio of thickness to chord length. Thickened trailing edge method has been adopted in the experimental airfoil model, such as [24, 120]. The trailing edge thickness is normally about 0.1%c. The method used in NASA experimental model [120] has been adopted in the paper. The E387 coordinates has been thickened between 0.95-1c with a blunt trailing edge of 0.1%c.

The steady Blade Element Momentum (BEM) method and CFD are used to analysis the performance of E387 and A7 turbine. In BEM code ,the 2D aerodynamic parameters (Cl, Cd) of airfoils at $Re = 1 \times 10^5$ are from experimental data [11, 120] and then

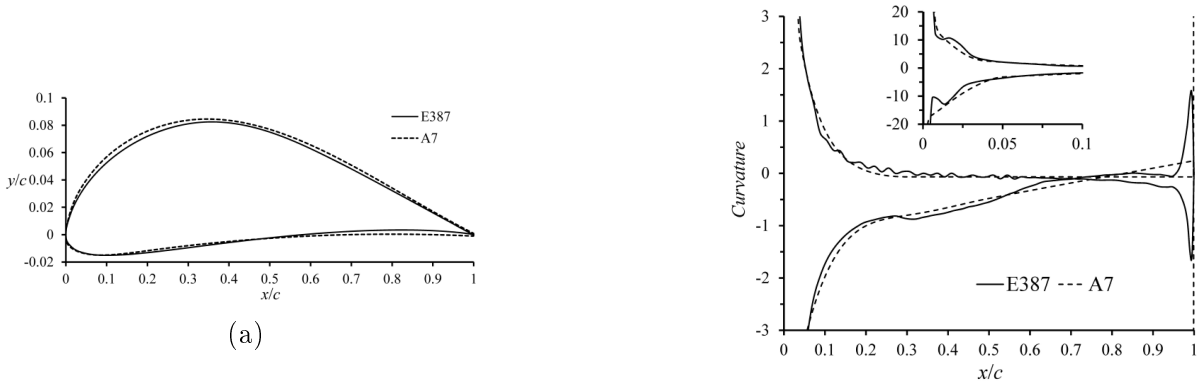

(a) (b)

Figure 4.3: Coordinates and curvature distribution of E387 and A7 [11]

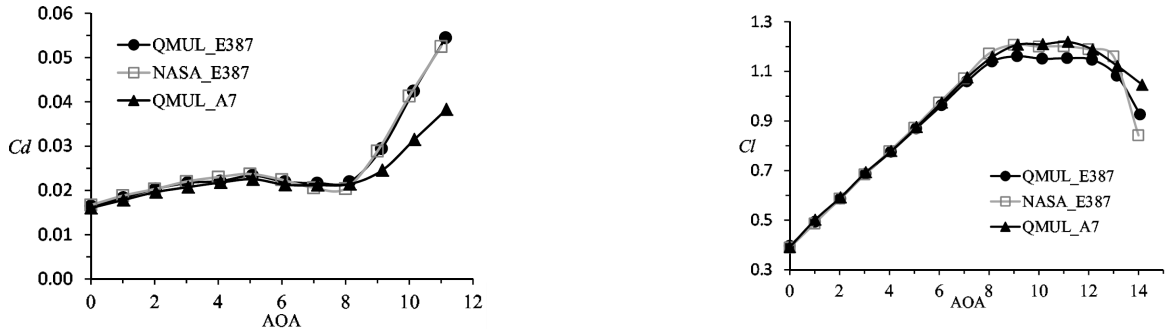

(a) (b)

Figure 4.4: Lift and drag coefficients versus AOA of E387 and A7 airfoils at Reynolds number 1×10^5 [11]

extrapolated using AirfoilPrep [121].

The computational domain is shown in Fig. 4.2b. Periodic boundary condition is used to reduce the computational resources. The origin of coordinate is located at the centre of rotational plane.The inlet is located 3 diameter (D) upstream of rotor, and the outlet is 10D downstream, the radial distance is 2.5D. The inlet boundary is specified as the velocity inlet at 0.6m/s at all cases, while the TSR is obtained by changing the rotational speed of the rotor. The outlet is specified as pressure outlet with a pressure of 1 atm neglecting the hydrostatic effect. The circumference is set as symmetry boundary condition, and the sides are set as periodic boundaries. The moving reference frame is used to account for the rotor rotating in steady RANS,and the sliding mesh is used for unsteady RANS calculation. The fluid field is assumed to be one phase (water), free surface and bed are not considered in this simulation. The TSR varies from 1 to 8, and the corresponding Reynolds number is $4.5 \times 10^4 - 1.8 \times 10^5$ based on the relative speed and a chord length at 0.5R. The prism and tetra mesh (Fig. 4.5) are used in this study. The prism layers are used in the blade surface to capture the boundary layer properties. Four different mesh sizes are used to study the mesh independence (Fig. 4.6), which shows that the grid converges at mesh size of 15 million with a y plus value (y^+) is below 2. References [71, 122] shows that the $k-\omega$ SST turbulence model was appropriate for this kind of calculation. ANSYS Fluent is used for the numerical simulation which runs on Apocrita cluster at QMUL. The residuals drop below 1×10^{-5} after about 3000 iterations

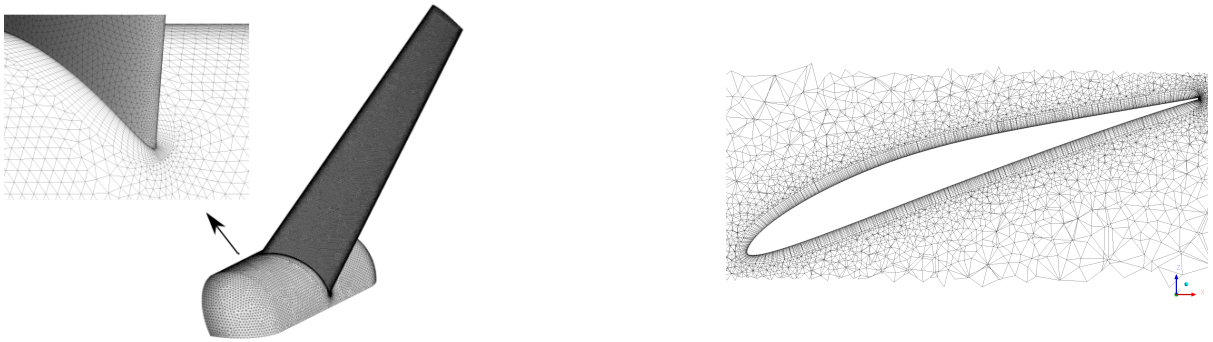

Figure 4.5: Mesh structure of E387 and A7

which took about 2.5-3 hours using 64 cores parallel running.

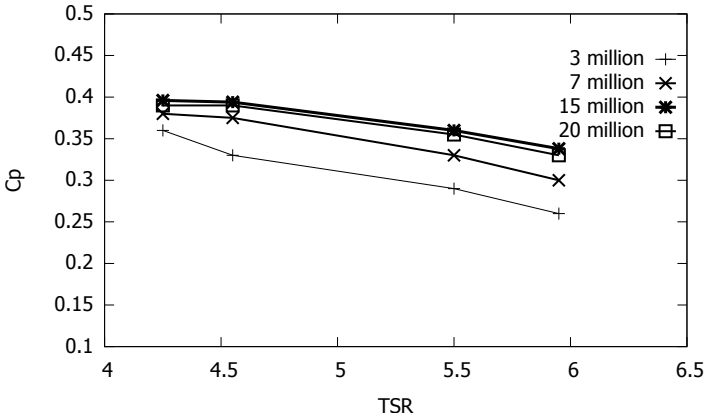

Figure 4.6: Grid convergence of E387

4.2.3 Results and Discussion

Fig. 4.7 compares the C_P and C_T from both steady and unsteady RANS calculations. The mean values of the unsteady RANS are almost identical to their steady RANS counterparts, although 3% fluctuations are observed. This shows that steady RANS is enough if quantities of interest are integral quantities, such as C_P and C_T. For the design of turbine blades, the steady RANS using moving reference frame is a trade-off solution between computational resources and accuracy. The variation of the power coefficient, C_P, with the TSR is shown in Fig. 4.8. Good agreement is observed between BEM, RANS and the experimental result conducted by Luznik et al [14]. When compared with the Cp from RANS, the power coefficient from BEM mildly overshoots near the optimal TSR. The BEM and RANS results show that the redesigned A7 turbine has noticeable better power performance at low TSR (1-4.25). From the RANS result, the power coefficient of the A7 turbine increased 5.5% at TSR 3.5. The improvement of Cp at low TSR can be explained after analysing the local angle of attack distribution along the spanwise direction at different TSR.

The optimal TSR is the TSR value where the max power coefficient is obtained. For E387 turbine, the optimal TSR is 4.25. Experimental results show that the E387 airfoil starts to stall when the AOA is higher than 8 degree at $Re = 1 \times 10^5$ [24] . When

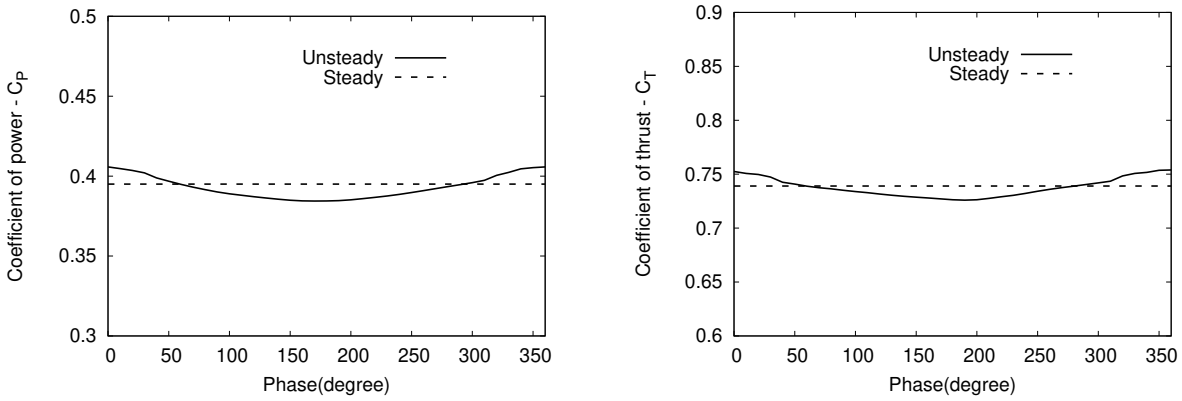

Figure 4.7: Instantaneous and steady power (a) and thrust (b) coefficients of E387, TSR=4.25

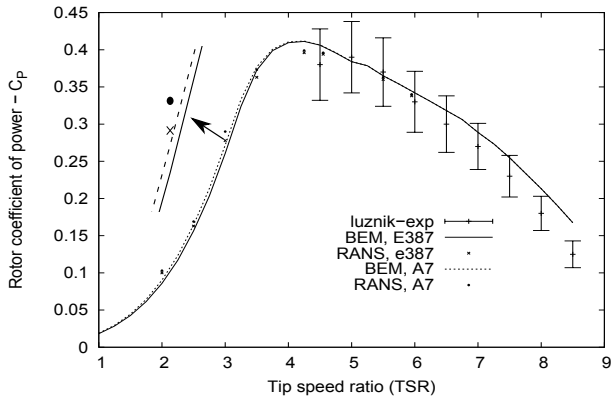

Figure 4.8: The power coefficient versus TSR

TSR is 4.25, the local angle of attack is stalled near the blade root ($r < 0.3R$) (Fig. 4.9a). When the operational TSR is below 4.25, the main body of the blade start to stall and the sectional lift decreases and drag increases dramatically. As the rotational speed decreases, the TSR decreases as well, which leads to the increase of the effective angle of attack, thus the blade stalls. The A7 turbine has marginally higher power coefficient compared to original E387 turbine due to the stall delay offered by the A7 profile.

The local angle of attack along spanwise direction is shown in Fig. 4.9a. At a fixed spanwise location, the local angle of attack decreases as the increase of TSR. Similarly, at a fixed TSR, the local angle of attack has highest value at root station and decreases towards the blade tip. The local angle of attack at all stations are stalled when the TSR is below 3. Fig. 4.9b shows the local angle of attack of E387 and A7 turbine at TSR =3.25. The angle of attacks of E387 and A7 turbine are the same, and the blades are stalled except towards the tip.

The lift to drag ratio is an important parameter for choosing the right airfoil shape of tidal turbine. The lift to drag ratio increases exponentially from root to tip (Fig. 4.10). The A7 turbine has better hydrodynamic efficiency around stall condition due to the delay in stall.

The local streamlines of E387 at three blade stations are shown in Fig. 4.11. A vortex exists at leading ledge at 0.2R when the rotor operates at TSR =3. The suction surface streamlines of E387 at three different $TSRs$ are shown in Fig. 4.12. For TSR =5, the flow is mainly attached to the suction side of the blade except the root region. At TSR=

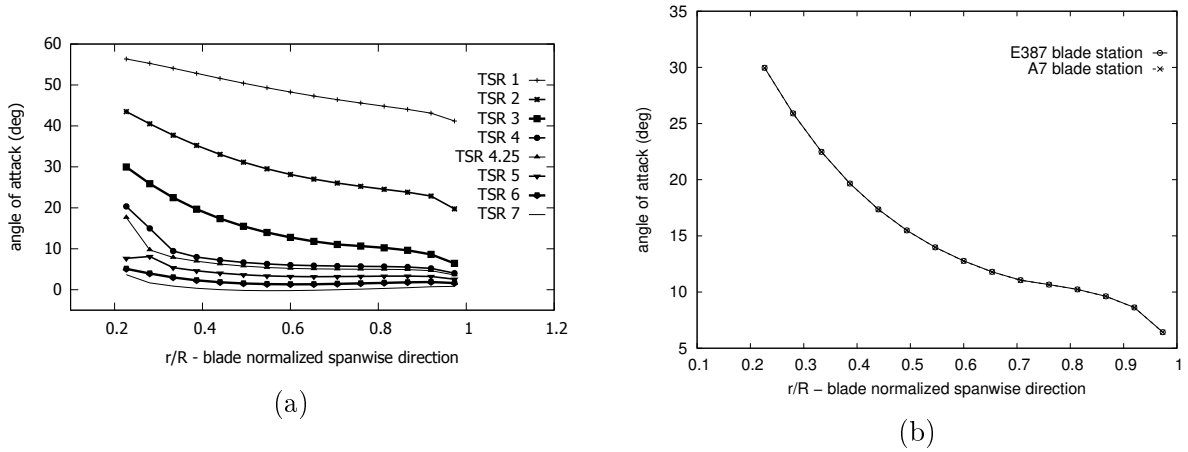

(a) (b)

Figure 4.9: Local angle of attacks of E387 at different TSRs (a) and angle of attack comparison at TSR 3.25 (b), BEM

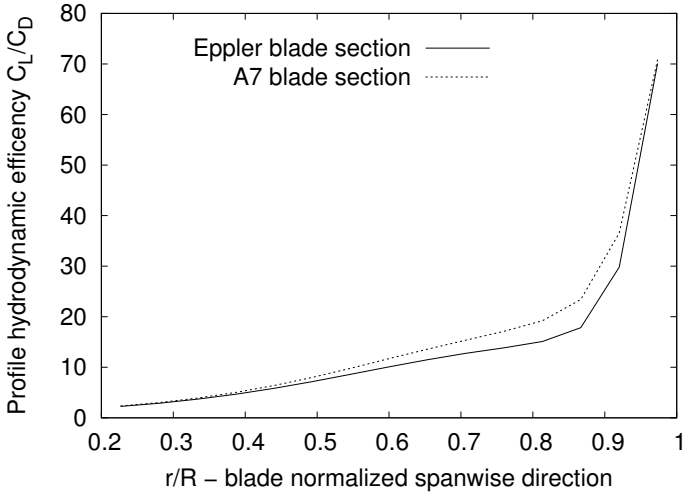

Figure 4.10: the hydrodynamic efficiency along spanwise direction, BEM results (TSR 3.25)

4.25, the flow separation starts from the trailing edge at the middle-span location. The suction surface streamlines of E387 and A7 at TSR 4.25 is shown in Fig. 4.13.

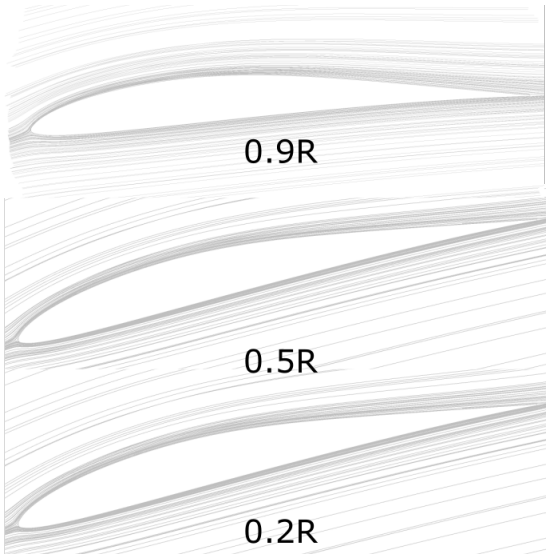

(a) TSR 5.5

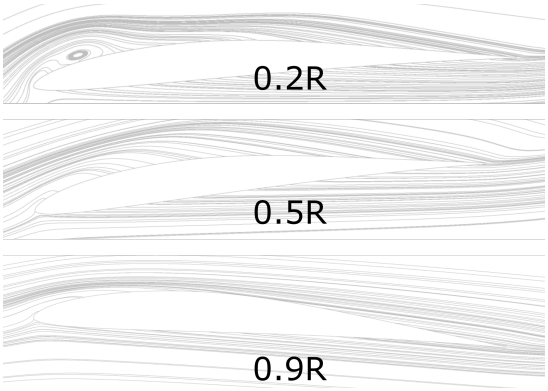

(b) TSR 3

Figure 4.11: Local steamline of E387, RANS results (rotational frame, chord lengths are scaled)

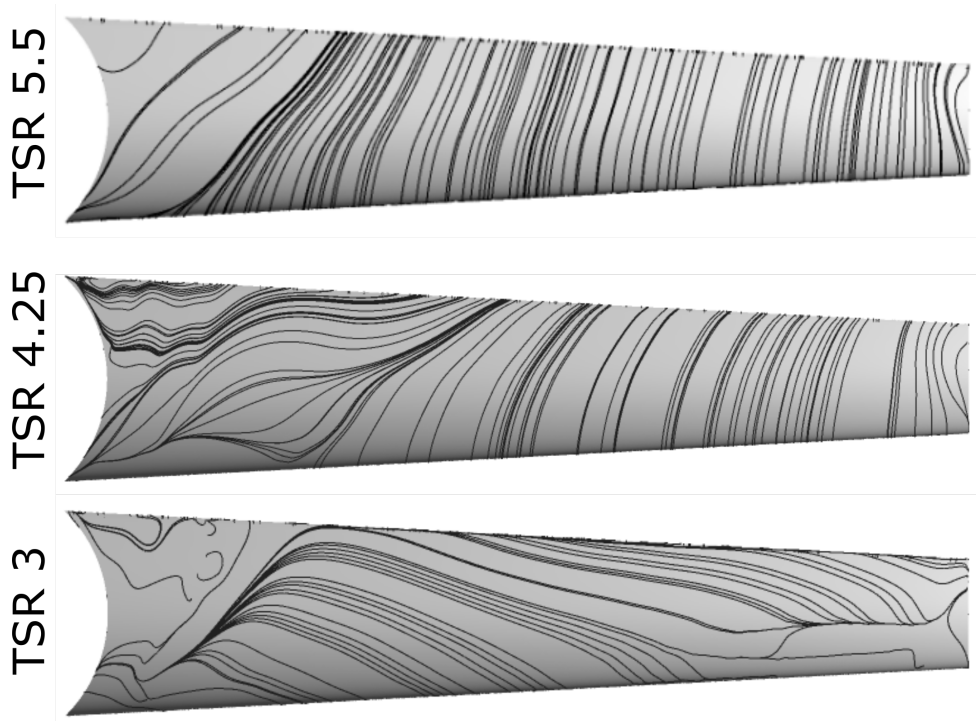

Figure 4.12: Blade surface limit streamline E387(flow direction from bottom to top)

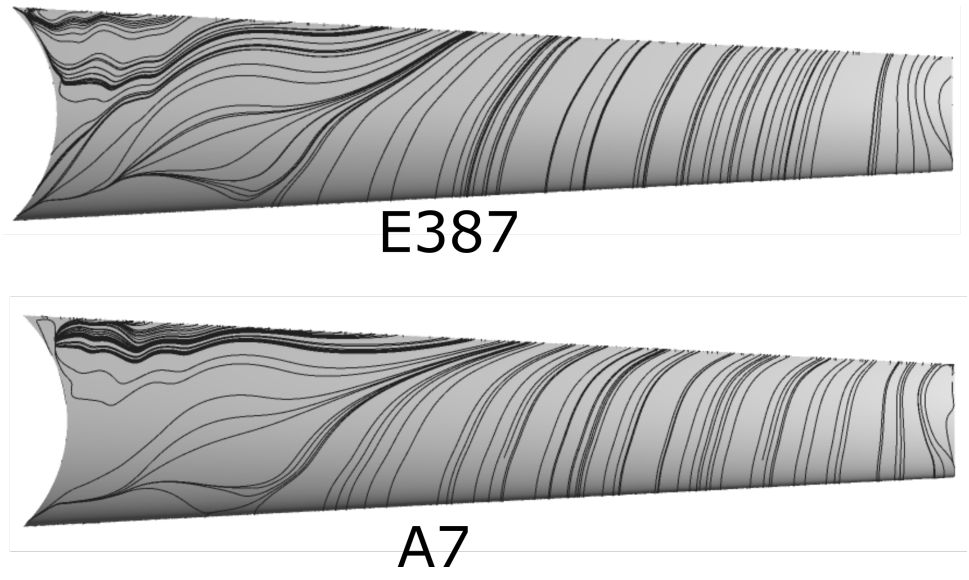

Figure 4.13: Blade surface limit streamline, TSR, 4.25

4.3 Optimal hydrodynamic behaviour analysis based on momentum theory

4.3.1 purpose of study

In this section, the chord length and pitch angle of E387 turbine are optimized using the Burton's model [106], and the Implicit model [123]. The performance is analyzed by the in-house code based on the blade element momentum method.

4.3.2 The optimum rotor methods

In the BEM model, the flow is simplified as steady, inviscid and incompressible. The blade is split into a number of annular control volumes with a radial size dr. Based on 1D momentum theory, the local torque acting on an annual control volume is:

$$dM = 4\pi\rho\Omega V_\infty(1-a)a'r^3dr \tag{4.1}$$

4.3.2.1 Burton's model

In the Burton's model, the derivation of local pitch angle and chord length based on the assumptions that the drag is ignored and the relationship between the axial and tangential induction factor are:

$$a = \frac{1}{3}, \quad a' = \frac{a(1-a)}{\lambda_r^2}, \quad \text{and} \quad \lambda_r = \frac{\Omega r}{V_\infty} \tag{4.2}$$

where λ_r is the local speed ratio, and r is the radial distance. For a given blade station at r distance from the centre of rotation, the local chord length distribution (c) and inflow angle (ϕ) have the following expressions:

$$c = \frac{16\pi R}{9B\lambda C_l\sqrt{4/9 + [\lambda_r + 2/(9\lambda_r)]^2}} \tag{4.3}$$

$$\tan\phi = \frac{2}{3\lambda_r + 2/3\lambda_r} \tag{4.4}$$

Then, the local pitch angle, $\theta(r)$, can be derived from the Eq. (3.9).

4.3.2.2 Implicit model

The implicit model proposed by Rosen is also derived from the classic BEM and ignores the drag. However, the optimal value of a is not given, and ϕ is related to a and a' in the following expressions.

$$\tan\phi = \frac{1-a}{\lambda_r(1+a')} \tag{4.5}$$

$$\frac{a}{1-a} = \frac{\sigma(r)C_L cos\phi}{4sin^2\phi} \tag{4.6}$$

$$\frac{a'}{1+a'} = \frac{\sigma(r)C_L}{4cos\phi} \tag{4.7}$$

$$\sigma(r) = \frac{Bc}{2\pi r} \tag{4.8}$$

where $\sigma(r)$ is the local solidity, which is related to the design lift coefficient, C_L as follows:

$$\sigma(r)C_L = 4(1 - cos\phi) \tag{4.9}$$

$$\lambda_r = \frac{sin\phi(2cos\phi - 1)}{(1 + 2cos\phi)(1 - cos\phi)} \tag{4.10}$$

The local inflow angle can be calculated using the Eq. (4.10) when a designed TSR and radial distance are given, then the local pitch angle,θ, is obtained from the Eq. (3.4), the local chord length, c, is obtained from the Eq. (4.9). The designed TSR, C_L, B and α are used input data during the blade design process. In this study, the designed number of blades, TSR, local angle of attack (AOA), lift coefficient are 3, 4.25, 8 (degrees), and 1.1 respectively. The designed TSR can not be determined mathematically, the designed local AOA is the maximum lift to drag coefficient for the E387 profile at $Re_c = 1 \times 10^5$ (Fig.4.14).

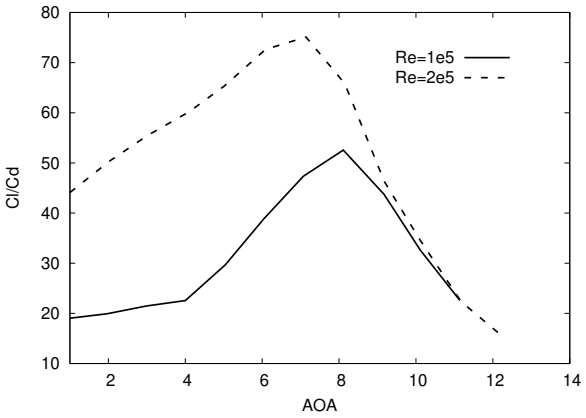

Figure 4.14: The lift to drag ratio of E387 airfoil

4.3.3 Results and discussion

The twist angle (β) and chord length (c) distribution of different models are shown in Fig.4.15a and Fig. 4.15b. Fig. 4.16a shows the power coefficient distribution of three models at different $TSRs$. The optimized models have similar performance at all $TSRs$. The max C_P of Burton's model has increased 13.1% compared with original E387 turbine at optimal TSR. Fig. 4.16b shows that the optimized blades have higher axial induction factor near the root (x<0.33). Fig.4.17 shows the thrust coefficient distribution of three different blades at different $TSRs$ (1-9). The implicit optimized blade has almost identical thrust coefficient as the experimental blade except near optimal TSR at which the implicit optimized blade has relative higher thrust coefficient value. The Burton's model has a higher thrust coefficient after TSR 3.5, and the differences between the experimental and Burton's model increases as the TSR goes up. The thrust coefficient of Burton's model increases 10% compared to the experimental blade at TSR 5. The chord length blade optimized by Burton's model is inversely proportional to TSR, thus a higher designed TSR leads to a smaller chord length. The drawback of Burton's model is that its chord

length distribution is more difficult to manufacture compared with the linear chord length distribution.

Figs. 4.18a and 4.18b show the tangential and axial induction factors of experimental E387 blade at different operating conditions. Tangential induction factors are much lower compared to axial induction factors. Tangential induction factors are high near the blade root and decrease rapidly until the middle span, followed by a gradual decline until the tip of blade. From $0.5R$, the higher the operating TSR, the lower the a'. Fig. 4.18b shows that the axial induction factors are around optimal axial induction factor (1/3) from 0.33-0.75R when the blade is operating near optimal TSR (TSR=4.25). Axial induction factors near the middle span of the blade are either too high or low when the blade operating at off-design $TSRs$, such as 3.25 and 5.25.

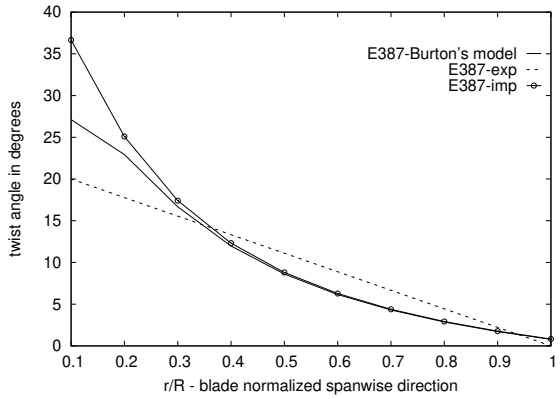

(a) twist angle (β) distribution along spanwise direction

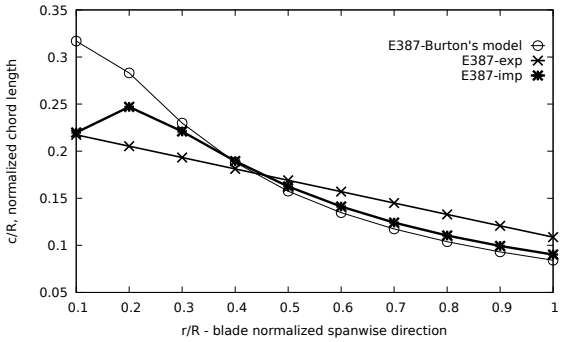

(b) chord length distribution along spanwise direction

Figure 4.15: Chord length and twist angle distribution along spanwise direction

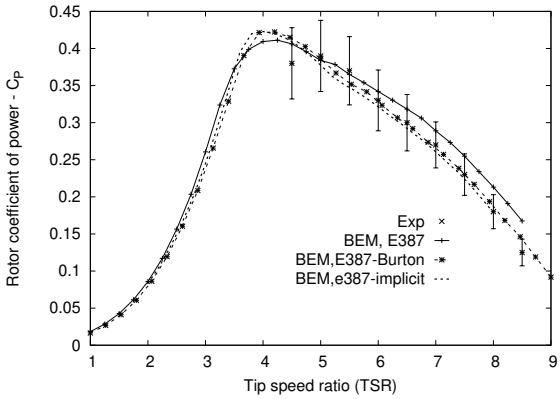

(a) The power coefficient versus TSR

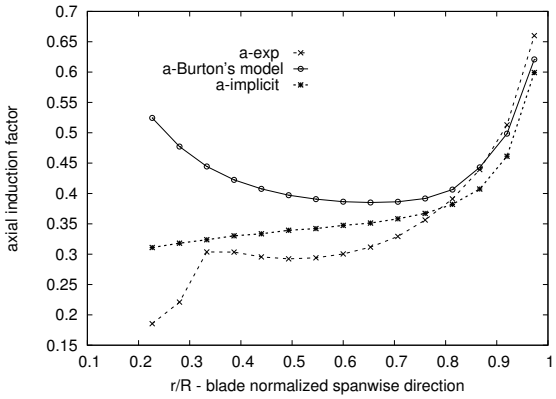

(b) axial velocity induction factor

Figure 4.16: Power coefficients and velocity induction factors of different models

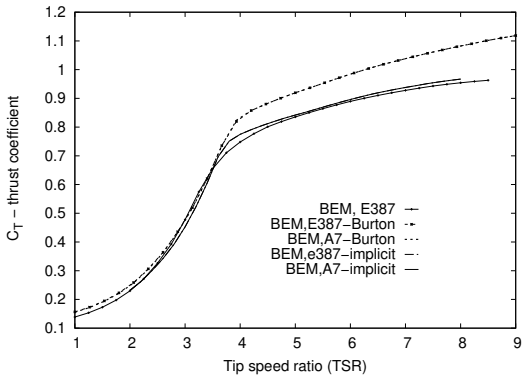

Figure 4.17: The thrust coefficient distributions of different models

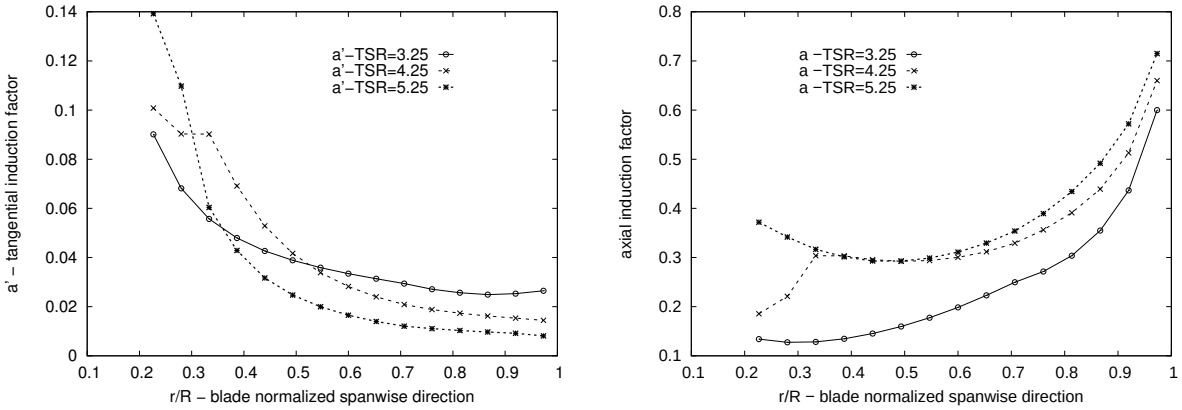

(a) tangential induction factor

(b) axial induction factor

Figure 4.18: The axial and tangential induction factors of E387

4.4 Summary

In the first section of this chapter, the E387 hydrofoil is optimized using the CIRCLE method and re-designed as the A7. Two turbines composed of E387 and A7 hydrofoils at different blade stations are numerical modelled using both the BEM and RANS methods. The BEM results of C_P overshoot at optimal and higher $TSRs$ compared with RANS results. The A7 turbine has mildly better power performance at low $TSRs$. This implies the continuous curvature blade can used a method to improve low TSR performance that commonly suffer stall conditions on the blade. The fluid visualization of blade sectional and surface streamlines provides insights for further blade design optimization.

In the second section of this chapter, the experimental blade is optimized using Burton's and Implicit models. The Burton's and Implicit models has non-linear distribution of chord length and twist angle along the spanwise direction. The Burton's and Implicit model have similar performance distribution. The performance of the optimized blade has improved 13.1% at the optimal TSR. As to the thrust coefficient distribution, the Implicit model has slight higher thrust around optimal TSR and almost identical thrust as the experimental blade at other $TSRs$. However, the Burton's model has obvious higher thrust coefficient when the blades operates at high $TSRs$. In summary, the implict model is more suitable solution for blade optimization design when both the performance and thrust parameters are considered.

Chapter 5

Hydrodynamic assessment of a dual-rotor horizontal axis marine current turbine

5.1 Introduction

The blades of the horizontal axis marine current turbine (HAMCT) are normally placed at the optimal AOA if the rotor disk is placed normal to the incoming velocity vector. For wind application this may require yaw control, but for marine currents with known and steady stream direction, a yaw free HAMCT seems to be ideally suited [124]. However, the tidal current alters its velocity to opposite direction every 12-24 hours . This will leave the HAMCT blades pitched at wrong angle for that direction, causing possible stall and much reduced power. This can be overcome using pitch angle control as commonly used in the wind power industry. However, the pitch controlled turbine increases the manufacture cost and reduces the reliability. Due to higher waterproof standard, the electrical pitch system for tidal turbine is more expensive than that of wind turbine which normally operates in a dry environment [125]. Thus, the industrial application of the pitch control system is commonly used for very large turbines and not for small and medium size ones. One possible solution for bi-direction current flow is the dual-rotor configuration with fixed pitch as illustrated in Fig. 5.2a. The aim of this chapter is to check whether there is potential gain in operating the rear rotor by analysing the hydrodynamic performance of a dual-rotor HAMCT.

In this study we have used the industrial approach of Blade Element Momentum (BEM) method coupled with the Park wake model and steady RANS with $k-\omega$ turbulence model. The BEM methods can provide accurate estimate of power and thrust, with minimal computational cost, while CFD RANS provides more insights on flow field. The rotor details and numerical methodologies are outlined in the next section, followed by analysis of numerical results of a generic dual-rotor HAMCT and a general analytical estimate of the power gain from the rear rotor.

5.2 Turbine geometry

Commonly, single-rotor HAMCTs are based on asymmetric profiles, such as the E387 of Luznik turbine of 46 cm diameter [14]. However, our numerical simulations using

the BEM and Park models have showed that there was little or no benefit operating a rear rotor based on such asymmetric profile. On the other hand, a noticeable benefit of increase in overall C_P was found when the blade profile was replaced by a symmetric profile as the NACA 00XX family. Thus the following results are based on the common NACA0012 and NACA0018 profiles. The three-blade HAMCT of Luznik et al [14] was used as the base geometric configuration. To achieve optimal performance in terms of C_P for high TSR , the blades were re-pitched according to $\theta = \theta_T(R/r)$ [123]. The subscript T stands for tip condition, r is the radial distance from the hub and R is the rotor's radius. Fig. 5.1(a) illustrates the local pitch angle at each station of three rotors tip-pitched at $2°, 0°, and -2°$ respectively, while the chord length distribution follows a linear relation as in [14] which is presented in Fig.5.1(b).

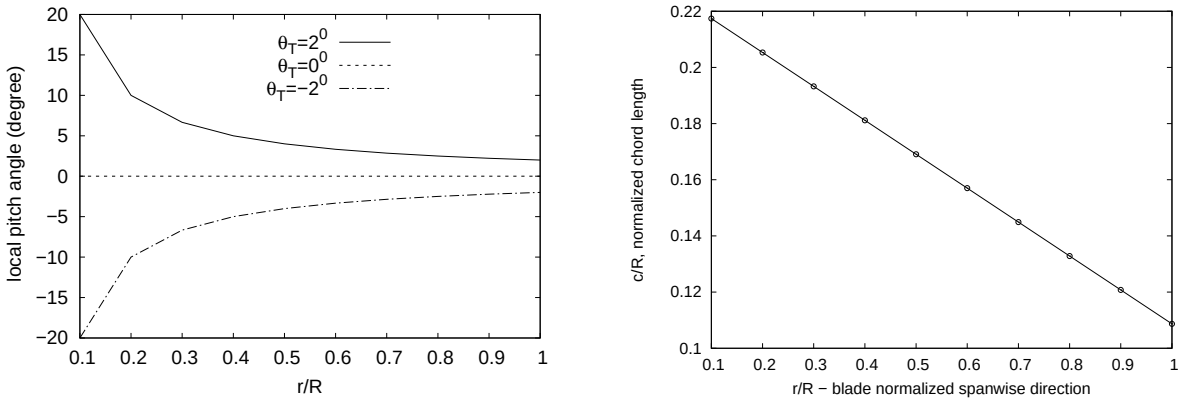

(a) (b)

Figure 5.1: The local pitch angle and chord length distribution of blades (θ_T stands for tip pitch angle)

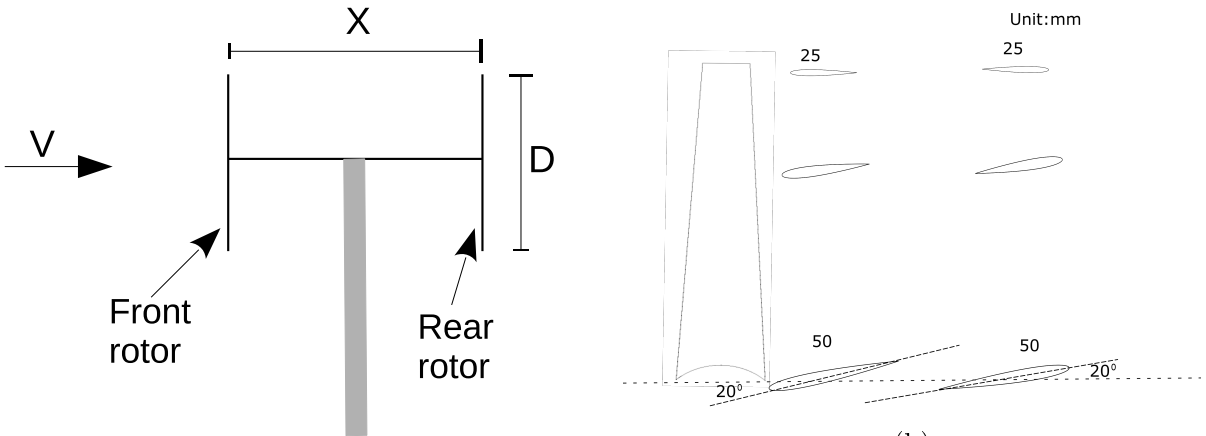

(a) (b)

Figure 5.2: Schematic description of the dual-rotor turbine (a) and blade profile at different stations (b)

5.3 Methodology

5.3.1 BEM and park wake model

The hydrodynamic performance of the dual-rotor turbine will be calculated using the Blade Element Momentum (BEM) method and Park wake model. The details of BEM theory and Park wake model are explained in Chapter 3. In the BEM, the C_L and C_D variation with AOA data based on the work of Xiang Shen [126] with Re_c=135,000 and 1,000,000. This Re_c is expected for this lab-size turbine [14,127]. Each rotor is dealt separately using the BEM approach, where the incoming velocity seen by the front rotor is the water free stream velocity and the incoming velocity seen by the rear rotor is provided by the wake model. The effect of the rear rotor on the front one is neglected in this study. This is justified by the very fast decay of upstream propagating swirl and assuming the rear rotor is not too close to the front rotor, thus not adding a noticeable effect on its axial velocity. Such assumptions are commonly used for co-axial propulsive rotors that are much closer to each other than the current dual-rotor configuration [128]. The effect of the front rotor on the rear one is expressed through the Park wake model where the swirl effect is again neglected and the deficit in the axial velocity is assumed to be radially independent. Such assumptions are more accurate for the far wake of $X > 3 - 4D$ than for the near wake, where X is the axial distance between the two rotors and D is the rotor diameter, see Fig.5.2a, but the effect of downstream swirl is also commonly neglected in much closer rotors [128] and as it will be seen the wake behind our front rotor is far from turbulent. The downstream propagating swirl and non-radially uniform velocity deficit will be examined in this study using the CFD approach. Following the Park wake model the incoming velocity seen by the rear rotor is reduced by δU [129];

$$\delta U = U_\infty(1 - \sqrt{1 - C_T^{front}})(\frac{D}{D + 2kX})^2 \tag{5.1}$$

where k is an empirical factor accounting for the spread of the wake and is taken as 0.04 (Marden et al, 2013). Later, we will see that it also dependson the free stream turbulence. In the unlikely case of a turbulent wake behind the front rotor, i.e. $C_T^{front} > 1$, the square root of $(1-C_T^{front})$ should be replaced by $2a$. When normalised by the free stream velocity U_∞, the turbine overall coefficients are defined as:

$$C_{T,dual} = C_T^{front} + (1 - \delta U/U_\infty)^2 C_T^{rear} \tag{5.2}$$

$$C_{P,dual} = C_P^{front} + (1 - \delta U/U_\infty)^3 C_P^{rear} \tag{5.3}$$

In the BEM, the incoming velocity seen by the rear rotor is denoted as U and assumed as uniform and changing as the TSR of front rotor varies. The TSR of the rear rotor is relative to the velocity seen by the rear rotor and defined as:

$$TSR_U^{rear} = \frac{\Omega_2 R}{U} \tag{5.4}$$

Where the Ω_2 is the rotational speed of the rear rotor. But, in CFD simulation, Ω_2 is user specified as U is unknown before calculation, thus it is not possible to calculate Ω_2 for a given TSR_U^{rear}. As U_∞ is pre-defined and known quantity in the simulation, thus it is convenient to use U_∞ as reference velocity, and $TSR_{U_\infty}^{rear}$ is defined as:

$$TSR_{U_\infty}^{rear} = \frac{\Omega_2 R}{U_\infty} \tag{5.5}$$

As the incoming velocity seen by front rotor is always U_∞, thus the TSR of front rotor is defined as:

$$TSR_{U_\infty} = \frac{\Omega_1 R}{U_\infty} \tag{5.6}$$

where the Ω_1 is the rotational speed of the front rotor.

5.3.2 CFD

The computational domains of one rotor and dual-rotor are shown in Figure 5.3. Periodic boundary condition is used to reduce the computational resources. The origin of coordinate is located at the axis centre of front rotor. The inlet is located 3 diameter (D) upstream of rotor, the outlet is 10D downstream of rear rotor, and the radial distance is 2.5D.

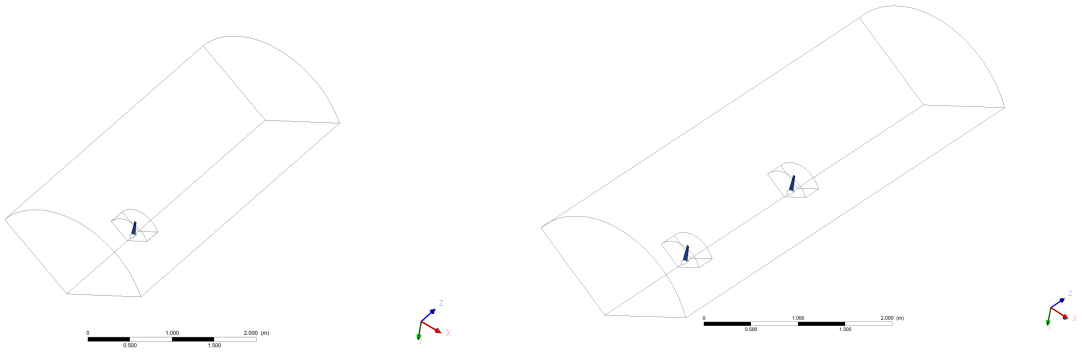

(a) (b)

Figure 5.3: Computational domains of one rotor (a) and dual-rotor (b)

A hybrid mesh is used in this study, with tetrahedron mesh used in the inner and hexahedron mesh used in the outer domain. the mesh size of inner domain is 6.7 million, while the outer domain mesh size is 124 × 63 × 60 (longitudinal × circumferential × radial). The meshing details for inner tetra mesh are similar with mesh detail mentioned in Chapter 4. A hexahedron mesh is used for the outer domain, which helps to reduce mesh size and have a finer mesh in wake region behind the turbine. Fig. 5.4 shows the mesh distributions on blade, interface, periodic boundary, inlet and outlet. The min edge size on the blade surface is 0.02mm with a mean edge size of 1mm. The surface mesh is extruded outward with 15 layers of prism mesh and a growth ratio of 1.2. The non-conformal interface are used to divide the whole computational domain into two domains. A mesh size of 10mm is used for the non-conformal interface 5.4 (c). The SST $K-\omega$ model was used for full geometry resolved steady simulation. References [71,122,130] show that SST $K-\omega$ model is better for flow with adverse pressure gradient and separation, such as airfoil, wing and rotating blade. The inlet boundary was specified as the velocity inlet at 0.6m/s at all cases, while the TSR was obtained by changing the rotational speed of the rotor. The outlet was specified as pressure outlet with a pressure of 1 atm neglecting the hydrostatic effect. The circumference was set as symmetry boundary condition, and the sides were set as periodic boundaries. To further reduce the computational cost, the Moving Reference Frame (MRF) was used to account for the rotor rotating [10]. The mean quantities (U, and P) are assumed as steady in the MRF, which further reduces the RANS equations. More time accurate models, such as UBEM and URANS, can be

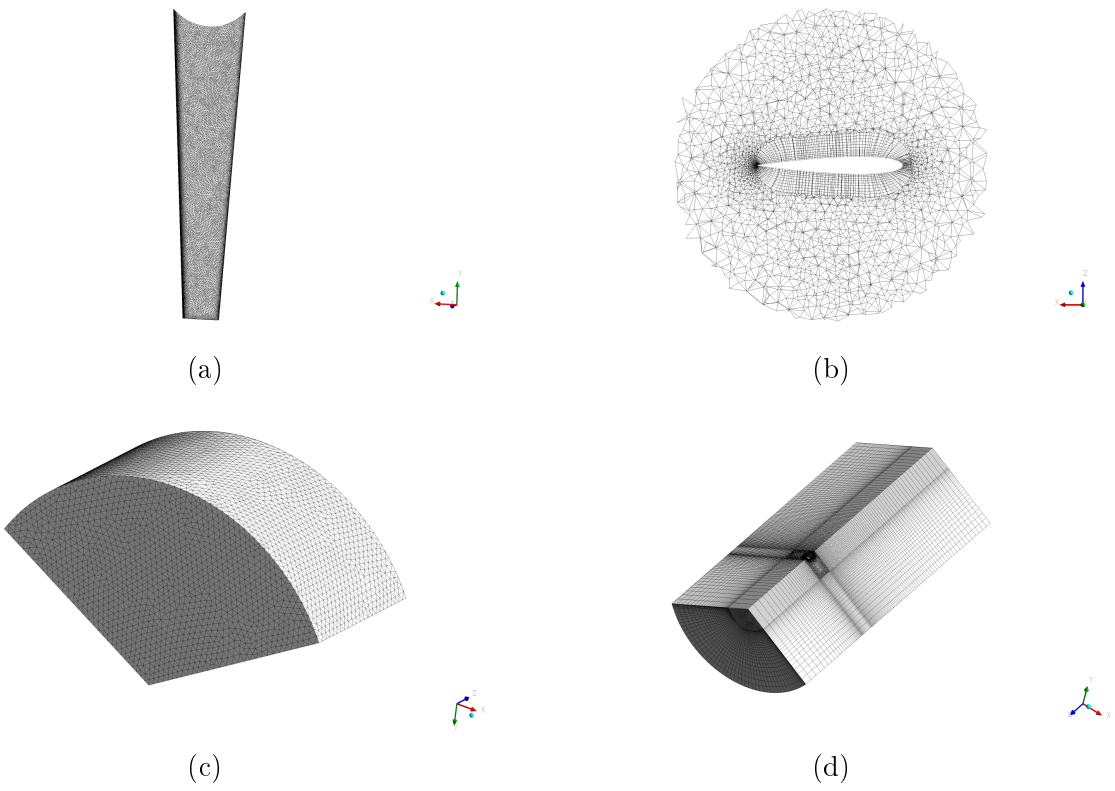

Figure 5.4: Mesh details for the turbine

used, but there is little benefit for predicting the time averaged quantities such as the mean C_P and C_T [71, 127]. The turbulence intensity and length scale were specified at inlet and out boundary conditions. The turbulence length scale is specified as 0.14m, which is 5% of diagonal length of the water tank [131]. Turbulence intensities of 1%, and 15% are used which corresponding to low, and high turbulence level respectively.

5.4 Numerical results and discussion

5.4.1 Power and thrust coefficients

The C_P and C_T variations with TSR are plotted in Fig. 5.5 for a single $0.46m$ turbine tip-pitched at $\theta_T = (-2°, 0°, 2°)$. For convenience, the power coefficient of a single-rotor tip-pitch at $\theta_T = (2°, 0°, -2°)$ are denoted as $C_{p,single}^{front}$, $C_{p,single}^{untwist}$, and $C_{p,single}^{rear}$ respectively. In general, the C_p and C_T from BEM results match their RANS counterparts, though larger discrepancies are observed when rotors operate at high TSRs or blades are negative pitched *i.e.*, $\theta_T = (-2°)$. It is seen that the single-rotor tip-pitched at $\theta_T = 2°$ produces the highest C_P almost up to 0.4, that is close to the C_P produced using the asymmetric profile E387 for this rotor [127]. Meanwhile, the optimum TSR of the rotor of $\theta_T = 2°$ is about 4.75 which is higher than that of E387 turbine (TSR=4) [127]. On the other hand, the rotor of $\theta_T = -2°$ has the lowest C_P that becomes negative at high TSR. This is as expected, since a negative θ_T places the profile opposite to the desired pitch angle illustrated in Fig. 5.2b. The $C_{p,single}^{rear}$ obtained from RANS is lower than the BEM's value. The maximum positive $C_{p,single}^{rear}$ gained from BEM is close 0.1, while its RANS's result is only close to 0.05. The negative pitch angle and high TSR also yields a C_T much larger

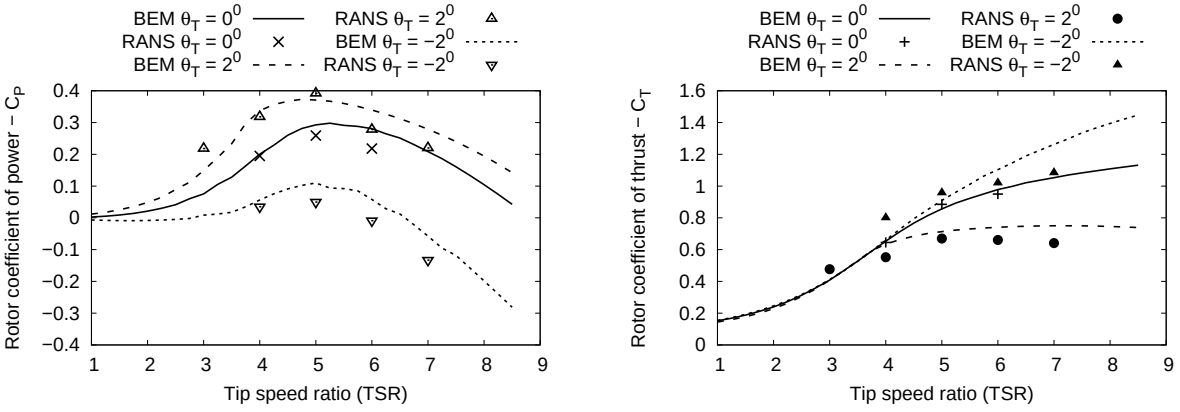

(a) (b)

Figure 5.5: Rotor's coefficient of power (C_P) and thrust (C_T) variations with the tip speed ratio (TSR) of each rotor for blade profile NACA0012 and Re_c=135K (TI =1% in RANS)

than one as seen in Fig. 5.5b, i.e. a turbulent wake behind the rotor. As a positive pitch angle is optimal for power performance, we expect the rear rotor will be at negative pitch angle as relative the wake velocity coming from the front rotor. The effect of turbulence intensity on the performance of the dual-rotor is further discussed in Fig. 5.7.

As a rotor is composed of various airfoils (hydrofoils) along the span-wise direction, a good understand of its lift and drag evolution with AOA is the foundation of blade design. The lift and drag variation over one revolution of NACA0012 profile at $Re_c = 1 \times 10^5$ is shown in Fig. 5.6. The first peak value of C_L is around 11.5° , followed by a sharp decrease of lift towards to 0.6 at 16° , and then climbs back and reaches maximum value close to 1 at around 42° [12].

The performance and thrust coefficients of an isolated single-rotor $\theta_T = -2°$ and the rear rotor of a dual-rotor are presented in Fig. 5.7. The rotor spacing is 4D in this case. Two ambient turbulence intensity are considered because the rear rotor of a dual-rotor turbine is operating in the wake region of front rotor, where velocity recovery rate is strongly influenced by the ambient turbulence levels [89]. However, the effect of turbulence intensity on an isolated rotor is less than 1% and negligible. The first obvious observation is that the power and thrust of a rotor operating in the wake region of front rotor is much lower than an isolated rotor's counterparts. The $C^{rear}_{P,dual}$ is lower than $C^{rear}_{P,single}$ is mainly due to the reduced velocity in the wake region of front rotor of a dual turbine. The RANS results show that the maximum $C^{rear}_{P,dual}$ is close to zero at TSR = 2.5 with $TI = 1\%$, which increases to 0.02 at TSR=3.2 with $TI = 15\%$. However, the maximum $C^{rear}_{P,dual}$ obtained from BEM-Park model is 0.04, which is higher than its RANS counterparts. The optimum TSR of the rear totor with $TI = 15\%$ is around 3, while its value is 3.65 from BEM result. This means the wake velocity is over predicted in the park model. For the same TSRs, the rear rotor always extracts more power at the high turbulence level, $TI = 15\%$ than the low turbulence level, $TI = 1\%$. Similar trends is observed for the thrust coefficient of the rear rotor of a dual turbine, as seen in Fig. 5.7 (b).

The dual-rotor's C_P variations with TSR are shown in Figs. 5.8a using the BEM approach. For $\theta = (0°, 2°)$ of the front rotor, where the rear rotor has a pitch angle of negative sign of that of the front. It is seen that operating both rotors at the same TSR

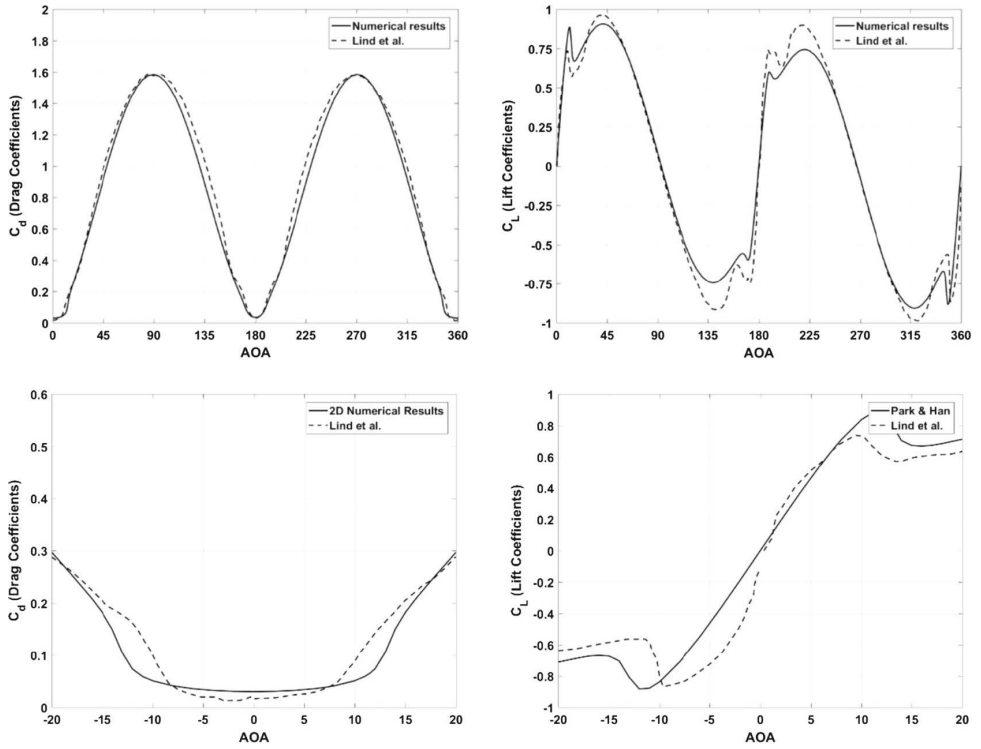

Figure 5.6: Lift and drag coefficients of NACA0012 at $Re = 1 \times 10^5$ ([12])

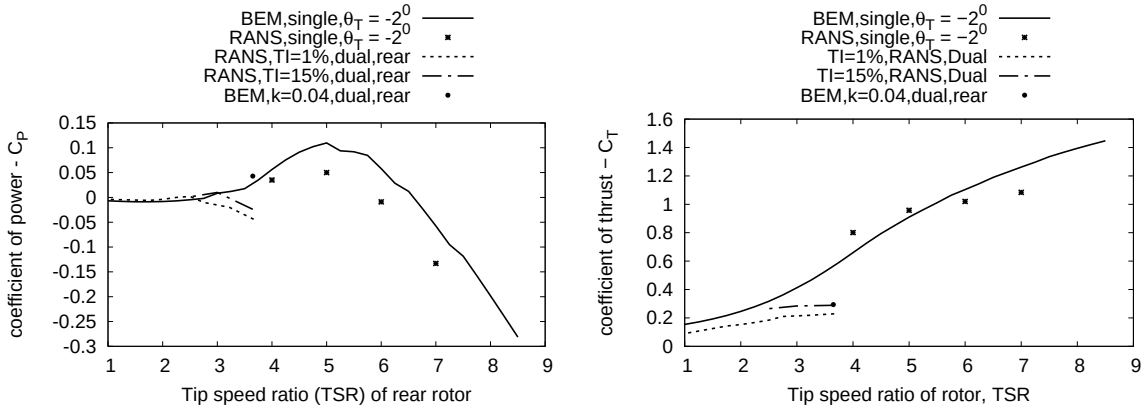

(a) (b)

Figure 5.7: Power and thrust coefficients of the rear rotor of a dual turbine (X=4D)with variable $TSR^{rear}_{U_\infty}$ and a fixed $TSR^{front}_{U_\infty} = 5$ (D=0.46m)

($TSR^{front}_{U_\infty} = TSR^{rear}_{U}$)results in an increase of up to 20% in C_P as relative to the C_P of the front rotor seen in Fig. 5.5a. This is because the peak of C_P is at about the same TSR for both the front and rear rotors. It results in a C_P mildly higher than that of the single-rotor of E387 in Fig. 5.8, while also being able to deal with a current of reversing directions. On the other hand, operating the rotors at the same rotational speed e.g. RPM, results in no improvement in the C_P.

Fig. 5.9 shows that increasing the stall AOA will enhance the performance of the dual-rotor turbine. This can be achieved using a profile design method as our CIRCLE approach [126] or by increasing the current low Reynolds number [132]. Increasing the profile Reynolds number Re_c from 135K to 1M as in the turbines of Figs. 5.10 means

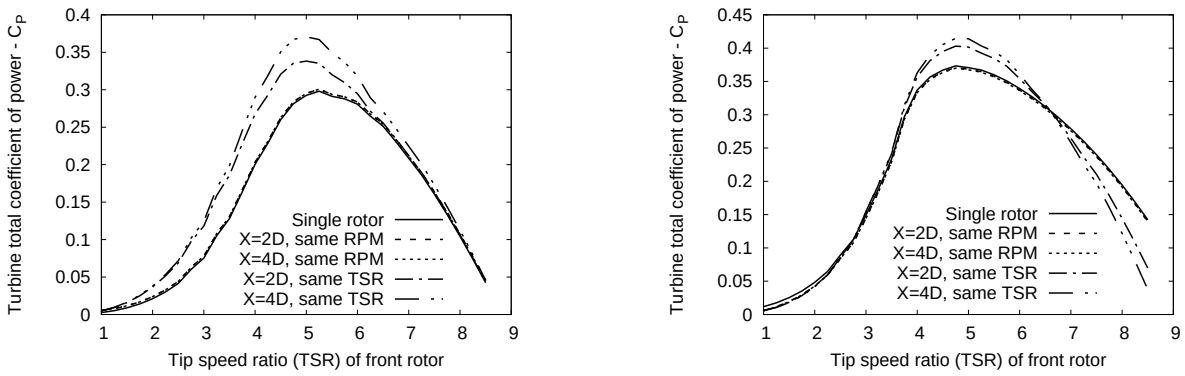

Figure 5.8: BEM results of turbine's total coefficient of power variation with the front rotor TSR and tip pitch angle (a) $\theta_T = 0°$ and (b) $\theta_T = 2°$ (Re_c=135k).

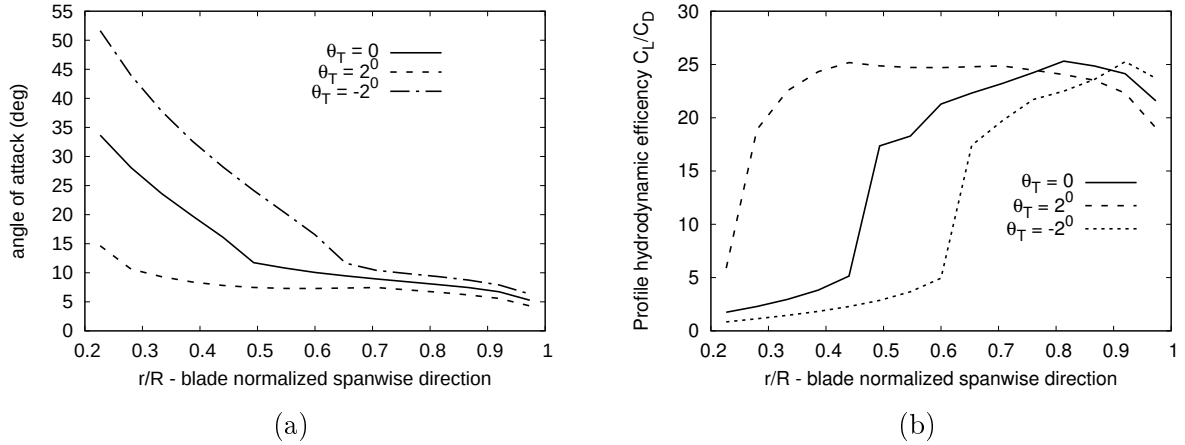

Figure 5.9: Local angle of attack and hydrodynamic efficiency distribution along the radial direction at TSR=5 for a single-rotor (BEM)

the turbine becomes of low mid-size diameter about 3.5 m. The BEM's C_P and C_T variations with TSR are shown in Figs. 5.10 for such dual-rotor turbines based on NACA0012 profile and the commonly-used thicker NACA0018, and for $\theta_T - (2°, -2°)$ of the front and rear rotors respectively. The C_P improves even just for the single-rotor when comparing with Fig. 5.5 a,because of the increase in the AOA of C_L, max from 110 for the NACA0012 of Re_c=135K to (160, 180) for the NACA0012 and NACA0018 of $Re_c = 1M$ respectively. Significant improvement in C_P is seen for the dual-rotor, particularly for the NACA0018-based, getting C_P, max to about 0.55 which is not far from the Betz limit of 0.59. The price to pay is a high thrust at high TSR as seen in Fig. 5.10 b, mostly due to the turbulence wake behind the rear rotor as was already seen from Fig. 5.5. The variation of the RPM_{rear}/RPM_{front} with TSR is shown in Fig. 5.11. This ratio is simply $1 - \delta U/U_\infty$ and it is seen that the RPM of the rear rotor has to be lower than that of the front one. There is a minimum in RPM_{rear}/RPM_{front}, which is slightly after the TSR of $C_{P,max}$. Increasing X reduces δV and thus increases the RPM ratio as seen in Fig. 5.11.

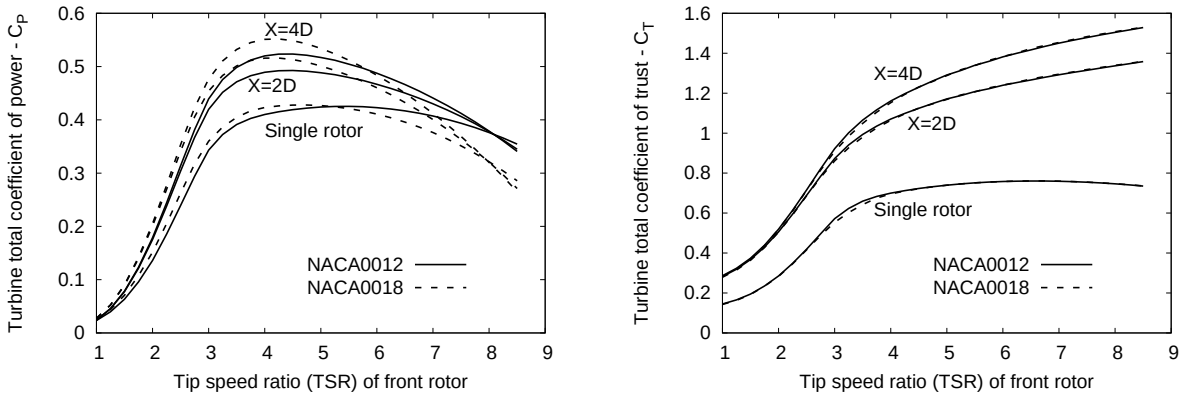

(a) (b)

Figure 5.10: Turbine's total coefficient of power C_P and thrust C_T variations with the TSR of the front rotor with root-pitch angle $\theta_T = 2°$, assuming $TSR_{U_\infty}^{front} = TSR_U^{rear}$ for both rotors and Re_c=1M (BEM).

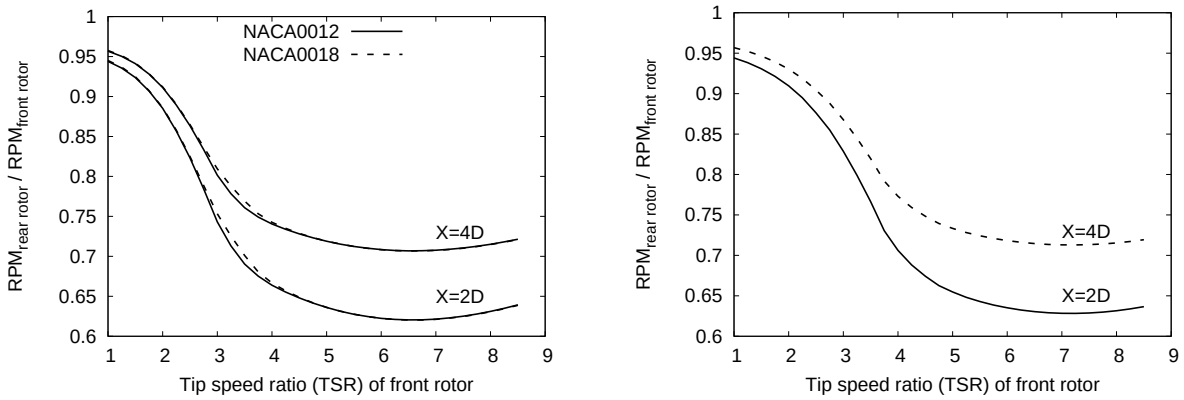

(a) Re_c=1M (b) NACA0012 at Re_c=135k

Figure 5.11: The variation of the RPM ratio between the two rotors of the dual-rotor turbines (BEM)

5.4.1.1 Effects of rotor spacing

Fig. 5.12a shows the effect of rotor spacing on the performance and thrust of a dual-rotor obtained from BEM-Park model at Reynolds number of 135,000. When the TSR of rotor varies between 3.5 and 6.5, the total power coefficient of dual-rotor increases steadily as the rotor spacing (X) grows. Similar trend was observed by Mycek et al [89], in which C_P increased as rotor spacing increasing at all TSRs and reached asymptotic value at X=6D. However, the analytical optimum distance is as close as 2.8D [88] which is lower than CFD result from Mycek et al [89]. The effect of rotor spacing on thrust of the dual-rotor is more noticeable when the TSR is higher than 4 (Fig. 5.12b). For example, for a dual-rotor operating at TSR 5,the C_T increases 5% when rotor spacing increases from 1D to 2D.

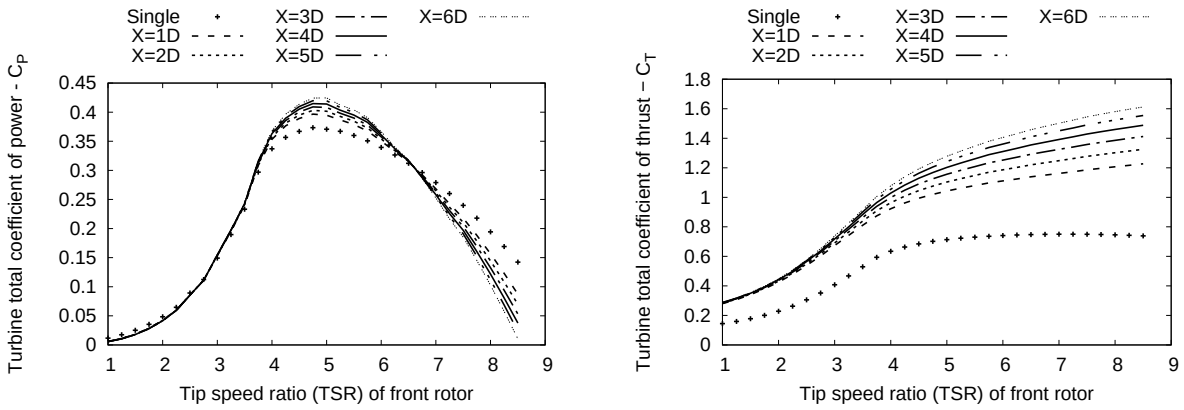

(a) (b)

Figure 5.12: Turbine's total coefficient of power C_P and thrust C_T variations with the TSR of the front rotor with tip pitch angle $\theta_T = 2°$, assuming same $TSR^{front} = TSR_U^{rear}$ for both rotors at Re_c=135k, (k=0.04) using the BEM approach.

5.4.2 Local angle of attack and streamline

The distribution of the AOA and profile's hydrodynamic efficiency C_L/C_D along the blade's span are shown in Fig.5.9. For $TSR = 5$ which is close to the maximum of C_P for $\theta_T = 2°$. The AOA for $\theta_T = -2°$ is well above the stall angle of about 12° for most of the blade except towards the tip. As result the rotor mostly operates in a post-stall condition giving a low hydrodynamic efficiency except towards the blade's tip, hence the low C_P in Fig. 5.5a. Increasing θ to zero reduces the post stall condition by pushing it more towards the hub, but a significant improvement occurs when θ is increased to 2°, resulting in an almost optimal AOA just around the AOA 11° of $C_{L,max}$ for most of the blade. This gives the very favourable C_P distribution in Fig. 5.5a and in the desired windmill state, showing C_T lower than one in Fig. 5.5b.

The streamline is an useful tool for locating flow separation and vortex region. The tangent direction of a point on streamline is the direction of velocity vector. In this study, the CFD-POST is used for the post-processing of RANS results. A sectional streamline around blade station gives more insight on local flow conditions. Fig. 5.13 shows the side view of streamlines of both single and dual-rotors at TSR 5. The inconsistency of streamline at the mesh interfaces are due to different start points of streamlines between the outer and inner domains. For the outer domain, the start points of streamlines are at the inlet, while the streamlines of the inner domain start from the interfaces. The first striking observation is the existence of vortex in the wake region in all three cases. The vortex size is about 0.5D for a single-rotor tip-pitched at $\theta_T = 2°$, while a much larger size of vortex (6D) is observed for a single-rotor tip-pitched at $\theta_T = -2°$. For a dual-rotor with front rotor tip-pitched at $\theta_T = 2°$, the size of vortex downstream front and rear rotors are almost the same as that of a single-rotor cases, although the shape of vortex downsteam of rear rotor (Fig. 5.13 (c)) is much more squeezed compared to that of a single-rotor tip-pitched at $\theta_T = -2°$. An interesting observation is that a new vortex is formulated in front of rear rotor.

Fig. 5.14 shows four sectional streamlines of a single-rotor tip-pitched at $\theta_T = 2°$ operating at around optimum TSR (TSR=5). A laminar separation bubble (LSB) is observed near leading edge of profile when r/R is below 0.5, and the LSB moves towards the leading edge as r/R decreases. The LSB near the inner board of blade thickens the

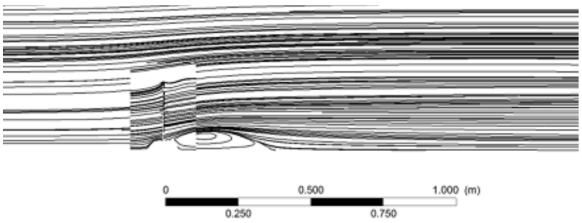

(a) single-rotor ($\theta_T = 2°$)

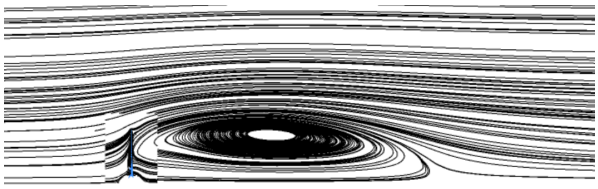

(b) single-rotor ($\theta_T = -2°$)

(c) dual-rotor, X=4D

Figure 5.13: Side view streamline of single and dual-rotors at TSR 5, TI=1% (RANS)

(a) 0.2R

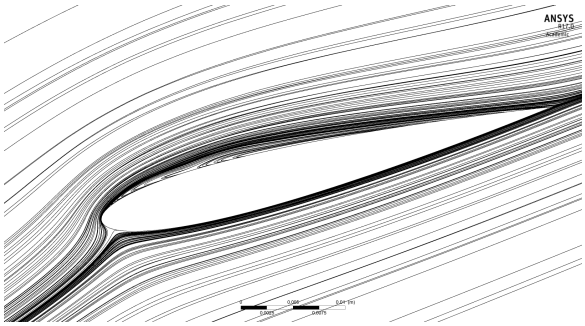

(b) 0.3R

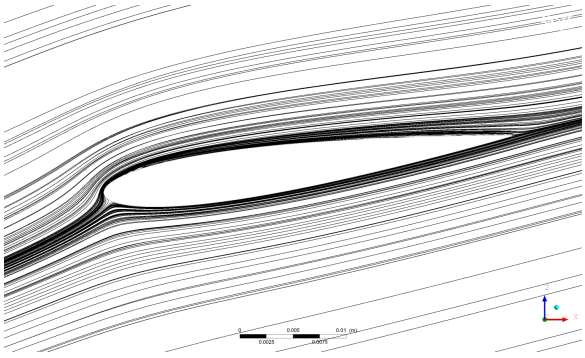

(c) 0.5R

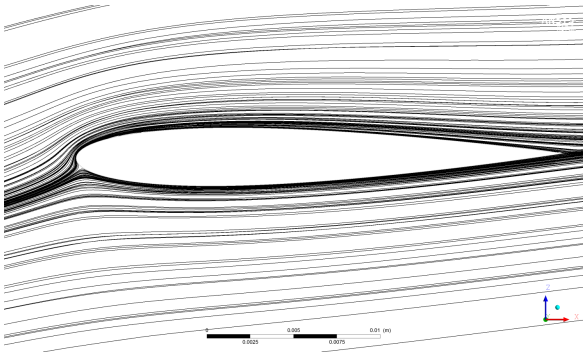

(d) 0.9R

Figure 5.14: Local streamline of single-rotor at TSR 5, TI=1% ($\theta_T = 2°$)

boundary layer and thus contributes to the decrease of profile hydrodynamic efficiency, C_L/C_D, which has been presented quantitatively in Fig. 5.9 using the BEM approach. The local AOA is relative to incoming free velocity vector seen by the blade profile and not the local slope of the streamline just in front of the blade profile, although they are not far from each other. To provide better estimate of the AOA from the CFD, several methods were allowed in the literature [133–135]. This can be important for a coupled

CFD-BEM method. For this study, we just note the good resemblance between the CFD and BEM's results.

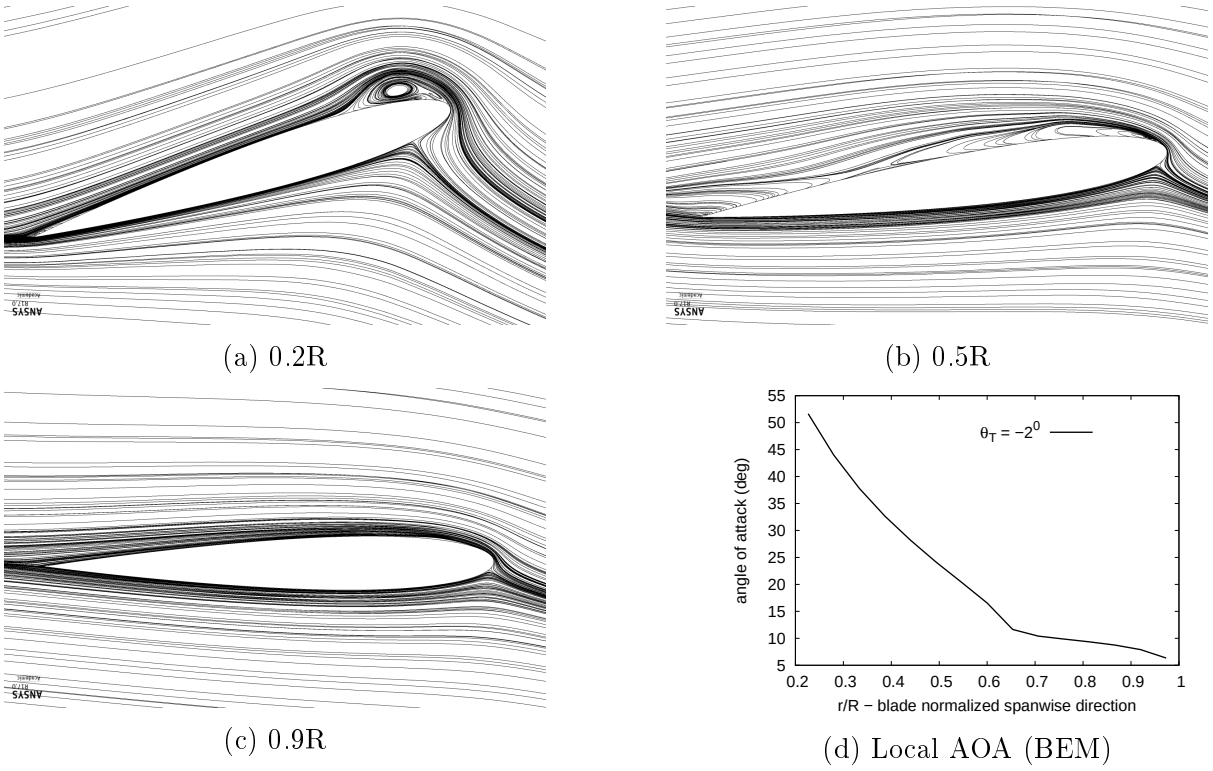

(a) 0.2R (b) 0.5R

(c) 0.9R (d) Local AOA (BEM)

Figure 5.15: Local streamline of single-rotor at TSR 5 ($\theta_T = -2°$)

Fig. 5.16 presents the local streamlines of rear rotor of a dual-rotor with fixed TSR of front rotor and variable $TSR_{\overline{U}}$ of rear rotor. Here, $\overline{U}$ is the area averaged mean axial velocity after a single-rotor tip-pitched at $\theta_T = 2°$ at X=4D. At low $TSR_{\overline{U}}$ (2.91, 3.75), there are large flow separation from the rear surface of the blade, while no flow separation is observed at high $TSR_{\overline{U}}$, such as $TSR_{\overline{U}} = 6$.

Fig. 5.17 presents the 3D streamline of single and dual-rotors. A nice screw-like vortex is seen behind the single-rotor at $\theta_T = 2°$ in Fig.5.17 (a), pointing to its high hydrodynamic efficiency. A large separated wake is seen behind the single-rotor of $\theta_T = -2°$, showing its low hydrodynamic efficiency. Illustration of the vortical wake behind the front rotor and how it affects the wake behind the rear rotor is shown in Fig. 5.17(c) & (d). The vortical wake shedded by the front rotor is seen to reduce the wake behind the rear rotor compared to the single-rotor wake of Fig. 18b and thus has the potential actually to mildly increase the rear rotor hydrodynamic efficiency, explaining the high Cp seen in Fig. 5.8 (b).

5.4.3 Wake characteristics

The mean axial velocity behind the front rotor is a key factor for the performance of rear rotor when the power is normalized by free stream velocity in front of front rotor, U_∞. The mean axial velocity data from RANS is area averaged and compared to the velocity deficit based on the Park wake model. In the RANS calculation, the area averaged axial

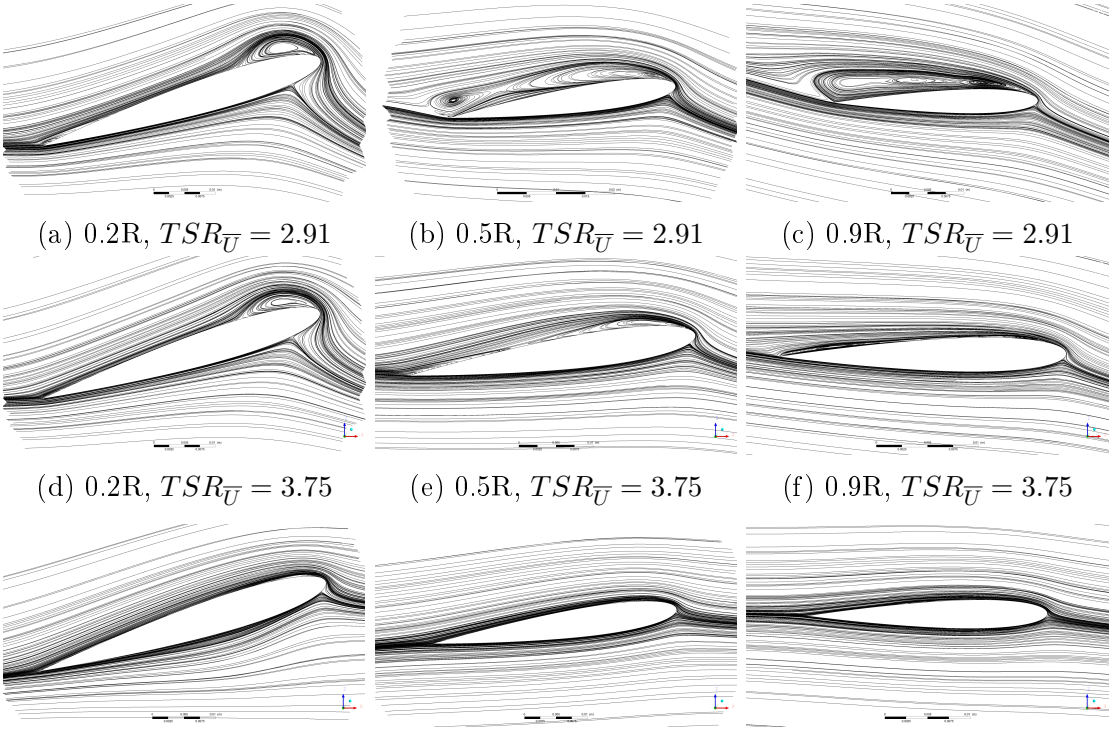

(a) 0.2R, $TSR_{\overline{U}} = 2.91$ (b) 0.5R, $TSR_{\overline{U}} = 2.91$ (c) 0.9R, $TSR_{\overline{U}} = 2.91$

(d) 0.2R, $TSR_{\overline{U}} = 3.75$ (e) 0.5R, $TSR_{\overline{U}} = 3.75$ (f) 0.9R, $TSR_{\overline{U}} = 3.75$

(g) 0.2R, $TSR_{\overline{U}} = 6$ (h) 0.5R, $TSR_{\overline{U}} = 6$ (i) 0.9R, $TSR_{\overline{U}} = 6$

Figure 5.16: Local streamline of the rear rotor of dual-rotor (X=4D) with $TSR^{front} = 5$ and variable TSR^{rear} (TI=1%, RANS, $\overline{U}$ is the mean axial velocity downstream a single-rotor tip-pitched $\theta_T = 2^\circ$)

mean velocity,$\overline{U}$, is defined as:

$$\overline{U} = \frac{\iint_{A(r)} U(x,y,z)dydz}{A(r)} \tag{5.7}$$

where U is the mean axial velocity, $A(r)$ is the area of wake region at a given axial distance (X/D) which is parallel to the rotational plane. Fig. 5.18 shows the mean axial velocity recovery as a function of non-dimensional axial distance after a single blade-twisted turbine ($\theta_T = 2^\circ$) which operates at TSR 5. Two turbulence intensity levels are available, namely 1% and 15%. These two turbulent intensities are corresponding to the low and high levels of turbulence intensity in a water tank or the field sites of tidal turbines. The value of k in the park model is related with turbulence intensity, and a relationship of k=0.4TI is used in this case, which is recommended by Pena [84] and Goccmen [136]. For RANS results, the axial mean velocity grows as the axial distance increases except in the very near wake of 1-2D, where a decrease of $\overline{U}$ is observed. However, a monotonic increase of $\overline{U}$ is observed in the park model. There is better agreement between BEM-Park model and RANS at the high turbulence level (TI=15%) than the low turbulence level(TI =1%). At TI=15%, the normalized axial mean velocity obtained from BEM-Park Model is about 6% higher than its RANS's counterpart. However, at TI=1%, general agreement is observed when X/D varies 1-3, but the slope of mean axial velocity obtained from RANS is higher than its BEM counterpart, which results in larger discrepancy as the axial distance increases. For example, the normalized axial mean velocity,$\overline{U}/U_\infty$, based on RANS results, is only 0.54 at $TI = 1\%$, and 0.63 at $TI = 15\%$ at $X = 2D$, which

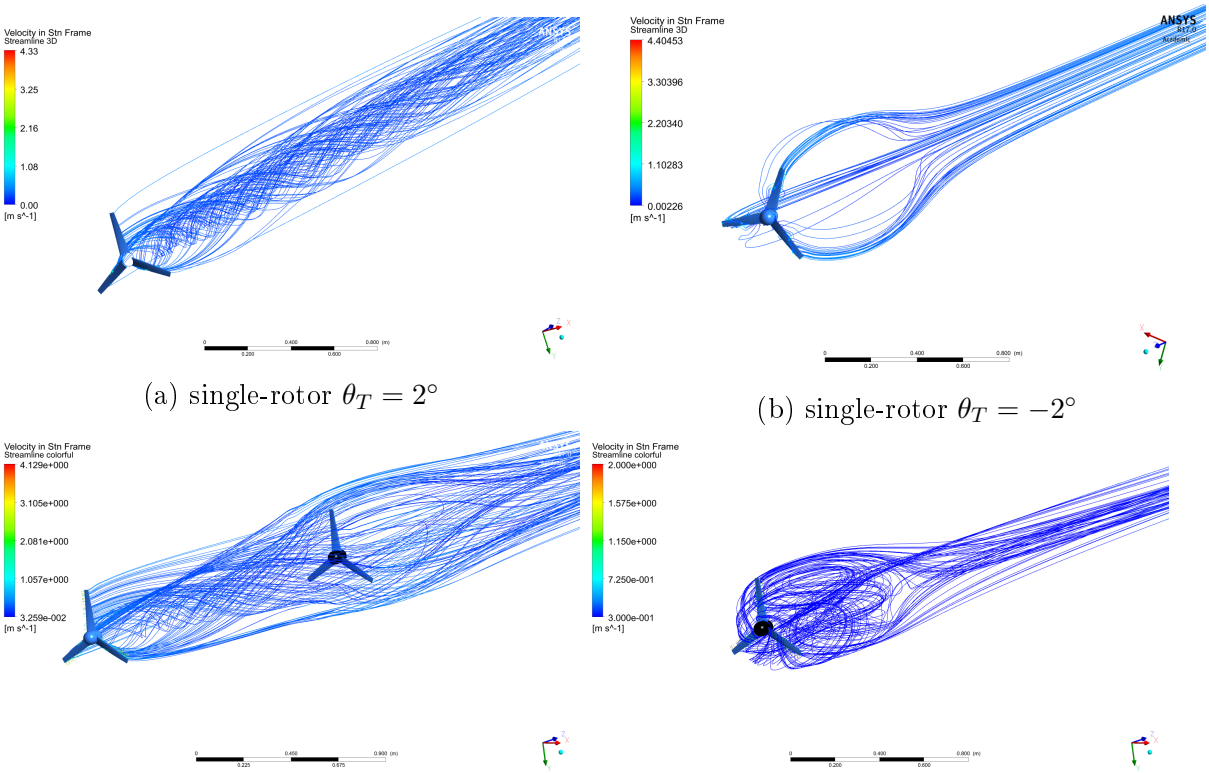

(a) single-rotor $\theta_T = 2°$

(b) single-rotor $\theta_T = -2°$

(c) dual-rotor $\theta_T = 2°$ with X=4D, streamline starts from front rotor

(d) dual-rotor $\theta_T = 2°$ with X=4D, streamline starts from rear rotor

Figure 5.17: 3D streamlines behind single and dual-rotors at TSR 5

increases to 0.58 and 0.72 at $X = 4D$. However, the axial mean velocity is a relatively high value of 0.8 U_∞ at $X = 4D$ according to Park model. If the wake axial velocity is $0.8U_\infty$, then the potential kinematic power is 0.51 $\rho U_\infty^3 A$. This explains why the power coefficient of rear rotor operating in a wake region is much lower than its counterpart operating in free stream velocity condition.

The evolution of the axial mean velocity in the wake region was presented in Fig. 5.18. For better fluid visualization, velocity contours are illustrated in order to enable better understanding of the potential in the dual-rotor configuration. Figs. 5.19, 5.20, 5.21, and 5.22 present velocity contours of a single-rotor tip-pitched at $\theta_T = 2°$, $\theta_T = -2°$ and a dual-rotor with rotor spacing of 4D. The wake regions are slightly larger than the rotor diameter in the radial direction. Meanwhile, a much longer low velocity region is observed for a single-rotor tip-pitched at $\theta_T = -2°$ compared with its $\theta_T = 2°$ counterpart. This is expected by the low hydrodynamic performance of the rotor at $\theta_T = -2°$ that also yielded a high C_T which is an indicator to a turbulent wake. For a single-rotor tip-pitched at $\theta_T = 2°$, whose wake shape is axisymmetric, while an non-axisymmetric wake is observed for a single-rotor tip-pitched at $\theta_T = -2°$ and a dual-rotor with rotor spacing of 4D.

Fig.5.23 presents side view of the turbulence intensity of a single and dual-rotors operating at TSR 5 with ambient turbulence intensity of 1%. Similarly as the side view of velocity contour, for a single-rotor tip-pitched at $\theta_T = -2°$, the area of high turbulence intensity is much larger than its $\theta_T = 2°$ counterpart. For a single-rotor tip-pitched at $\theta_T = -2°$, a high turbulence intensity region (such as TI >0.28) extends to 5D downstream after the rotor and 0.6D in radial direction, while the high turbulence

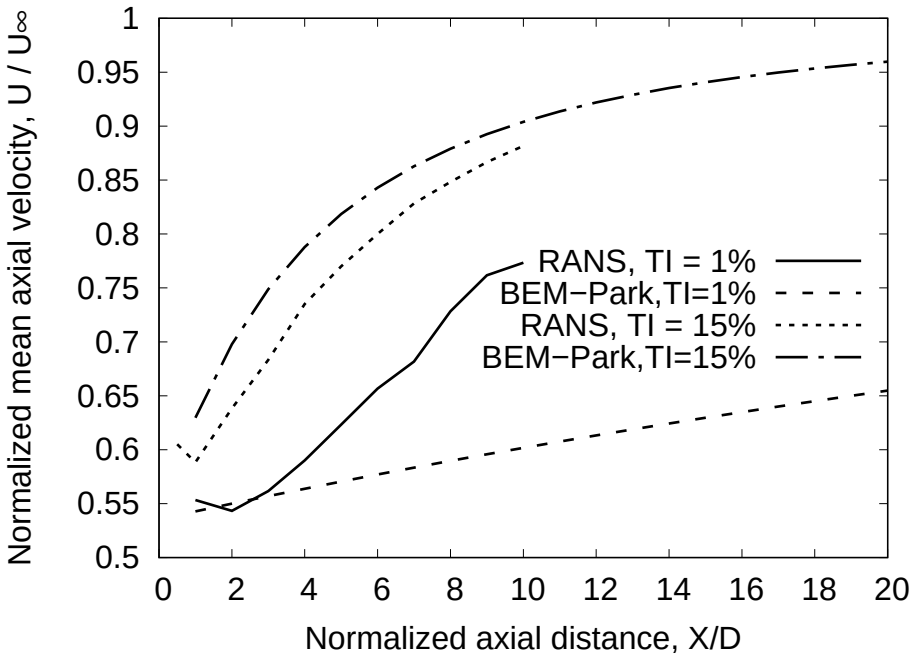

Figure 5.18: Normalized axial mean velocity downstream of a single-rotor tip-pitched at $\theta_T = 2°$ (k=0.4 TI, TSR 5)

intensity region is mainly constrained near the hub for a single-rotor tip-pitched at $\theta_T = 2°$. For a dual-rotor with X=4D, an interesting observation is that a turbulence intensity region is developed in front of rear rotor. Figs.5.24, 5.25 and 5.26 show the development of turbulent kinetic energy of a single-rotor tip-pitched at $\theta_T = 2°$, $\theta_T = -2°$ and a dual-rotor with rotor spacing of 4D at different downstream distances. For a single-rotor tip-pitched at $\theta_T = 2°$, the maximum TKE is observed near the hub in the near wake region (such as X=1D), then it is observed near the blade tip and extends inward in radial direction as downstream distance (X/D) increases, finally the TKE is more or less homogeneous in the wake region at 10D downstream of rotor. A striking different evolution is observed for a single-rotor tip-pitched at $\theta_T = -2°$, the high TKE region (red color) occupies the whole rotor disk area and decays along streamwise direction. For a dual-rotor with X=4D, an non-axisymmetric TKE is observed at all downstream distances. At the same downstream distance, the TKE level downstream of the rear rotor is lower than that of a single-rotor tip-pitched at $\theta_T = -2°$, such as at 1D behind the rear rotor, the TKE Level (Fig.5.26 (d)) is lower than its $\theta_T = -2°$'s counterpart (Fig.5.25(a)).

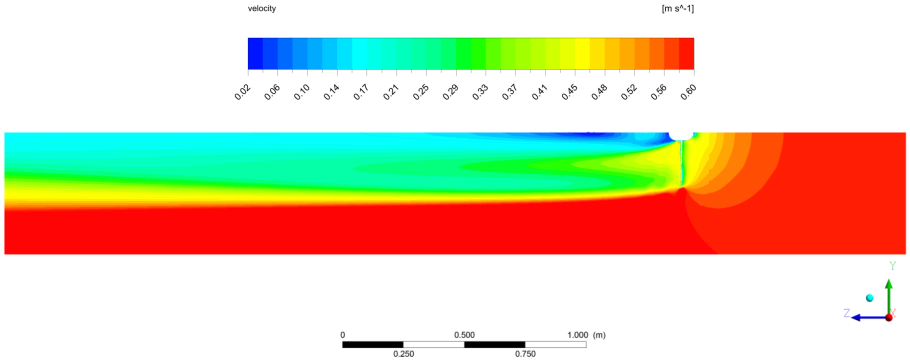

(a) single-rotor, $\theta_T = 2°$

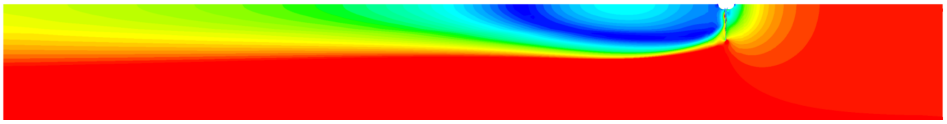

(b) single-rotor, $\theta_T = -2°$

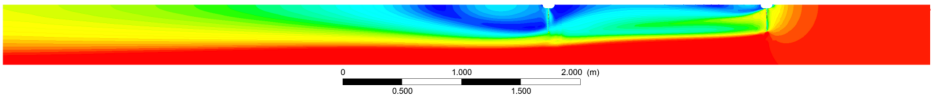

(c) dual-rotor with X=4D ($TSR^{front} = 5, TSR^{rear} = 3.5$)

Figure 5.19: Side view velocity contour of single and dual-rotors (inlet at right side)

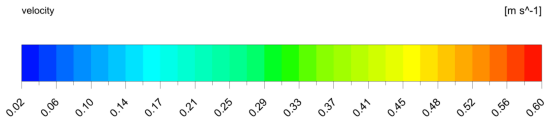

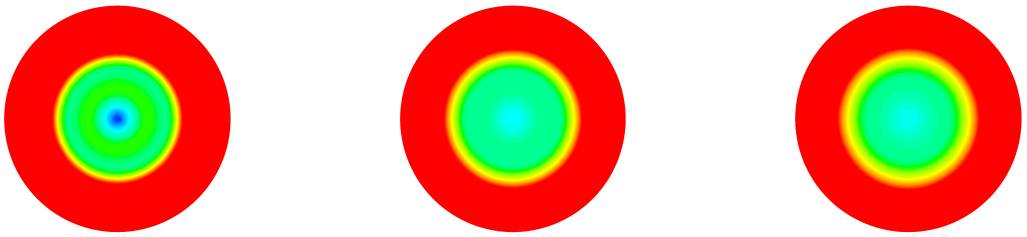

(a) 1D (b) 3D (c) 4D

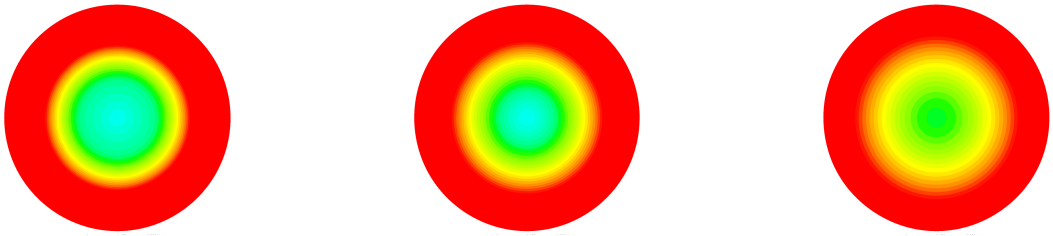

(d) 5D (e) 7D (f) 10D

Figure 5.20: Front view of the velocity contour behind single-rotor at TSR 5 ($\theta_T = 2°$)

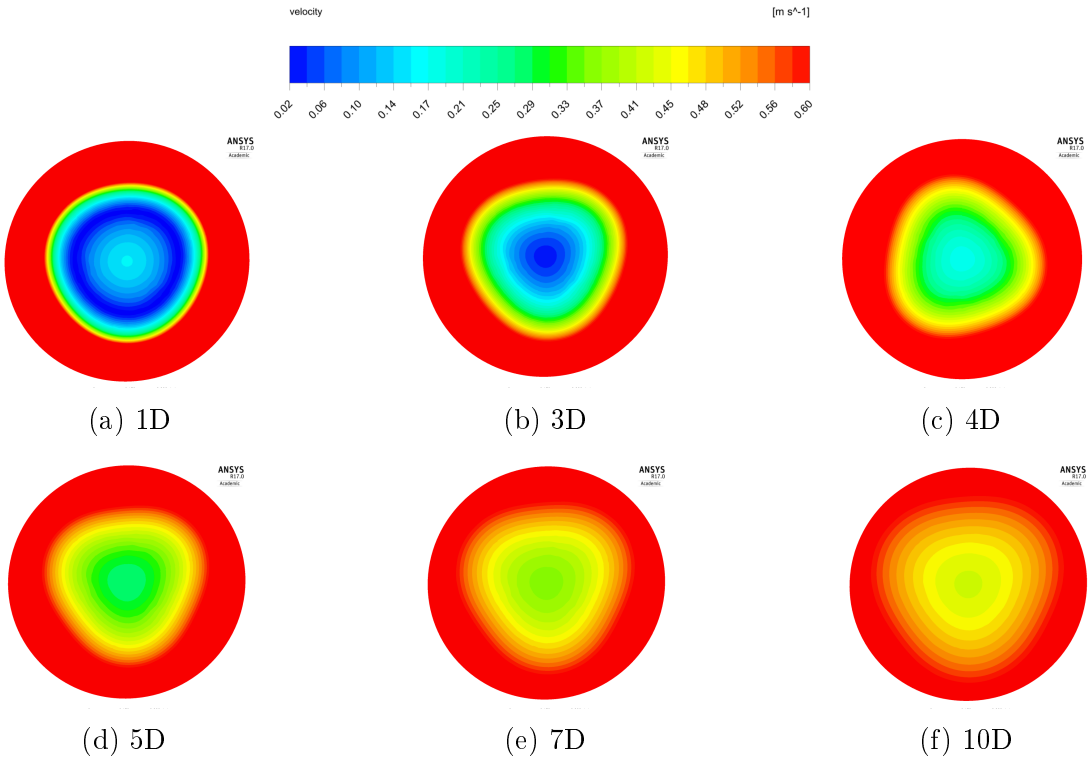

(a) 1D (b) 3D (c) 4D

(d) 5D (e) 7D (f) 10D

Figure 5.21: Front view of the velocity contour behind single-rotor at TSR 5 ($\theta_T = -2°$)

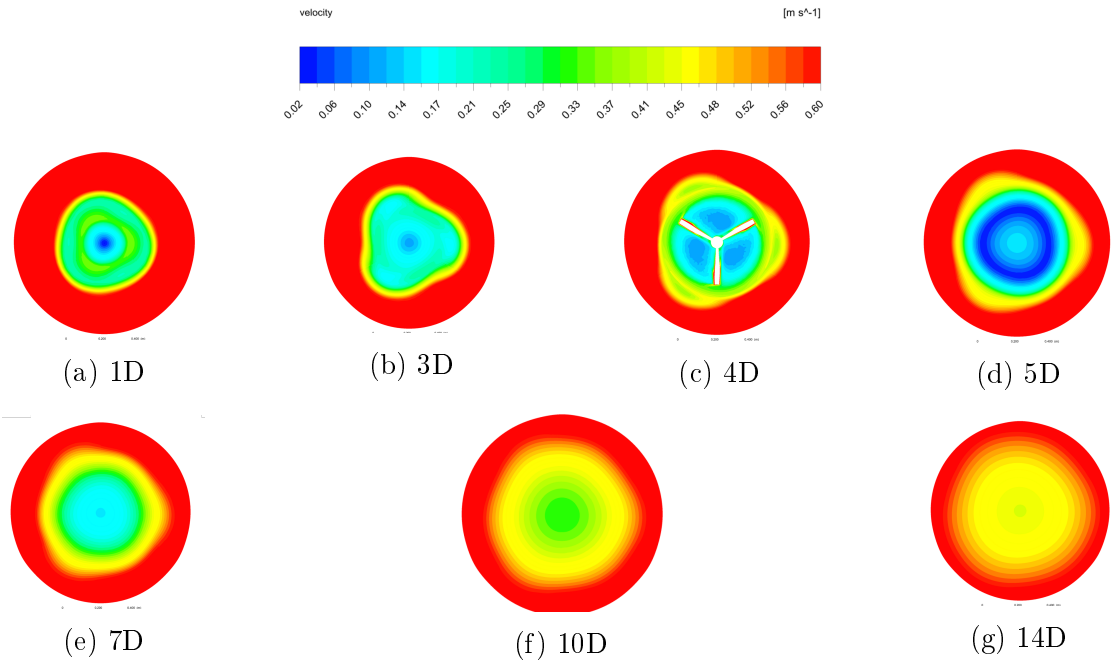

(a) 1D (b) 3D (c) 4D (d) 5D

(e) 7D (f) 10D (g) 14D

Figure 5.22: Front view of the velocity contour of dual-rotor with X=4D at TSR 5 (front rotor, $\theta_T = 2°$, origin is located at the axis center of front rotor)

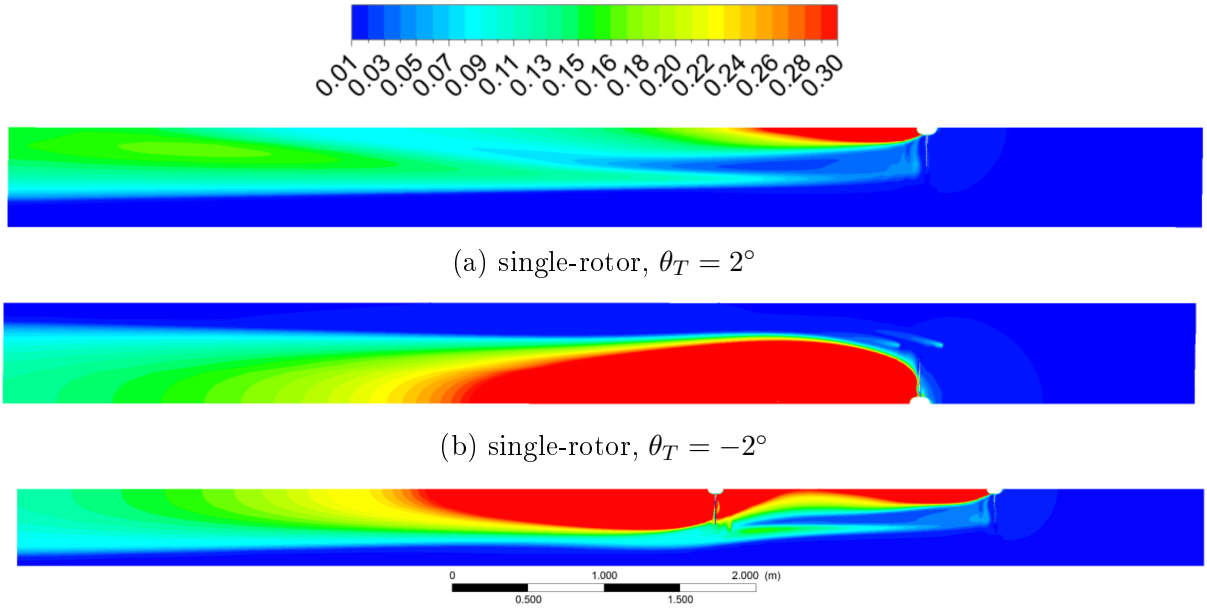

(a) single-rotor, $\theta_T = 2°$

(b) single-rotor, $\theta_T = -2°$

(c) dual-rotor with X=4D (front rotor, $\theta_T = 2°$)

Figure 5.23: Side view turbulence intensity of single and dual-rotors at TSR 5 (ambient TI=1%)

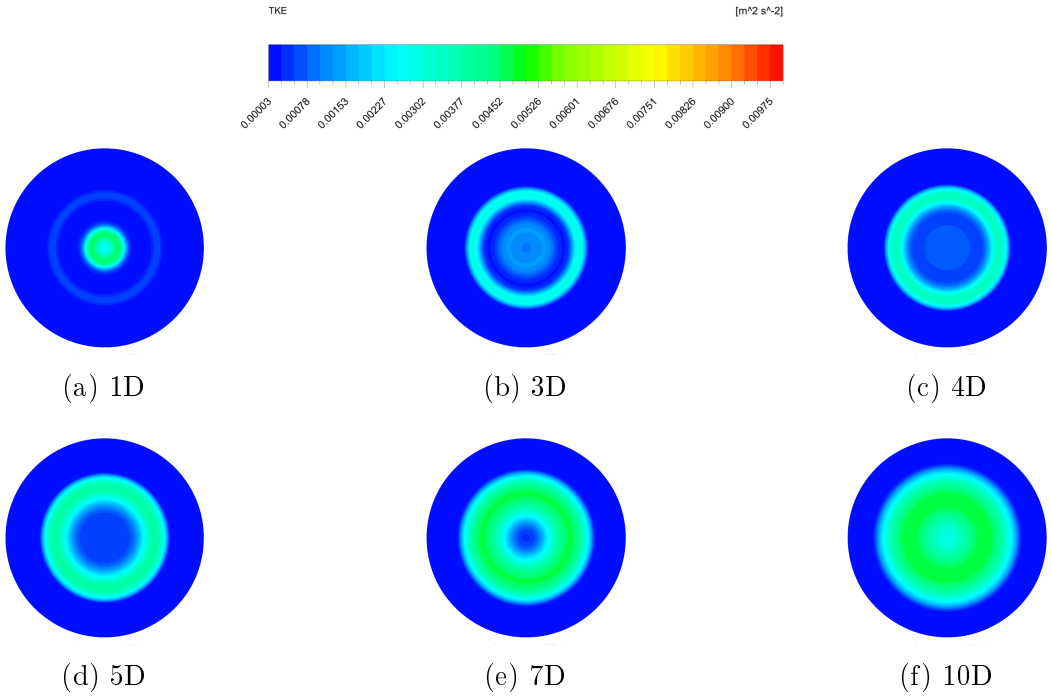

(a) 1D (b) 3D (c) 4D

(d) 5D (e) 7D (f) 10D

Figure 5.24: Front view of the turbulence kinetic energy of single-rotor at TSR 5 ($\theta_T = 2°$,TI =1% RANS)

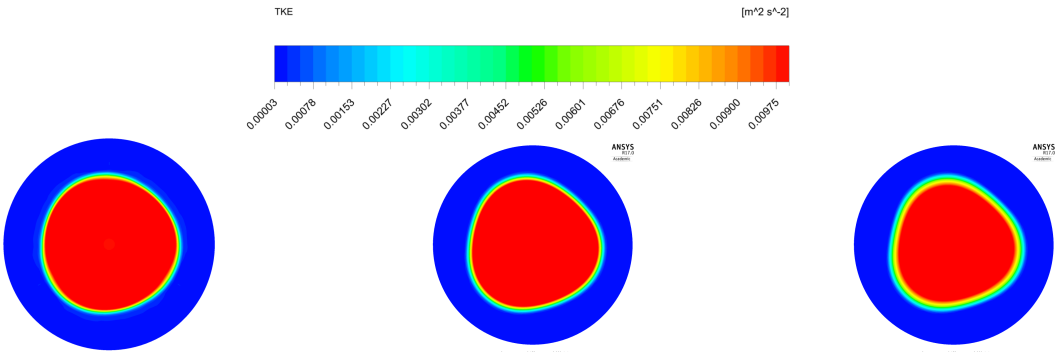

(a) 1D (b) 3D (c) 4D

(d) 5D (e) 7D (f) 10D

Figure 5.25: Front view of the turbulence kinetic energy of single-rotor at TSR 5 ($\theta_T = -2°$,TI =1% RANS)

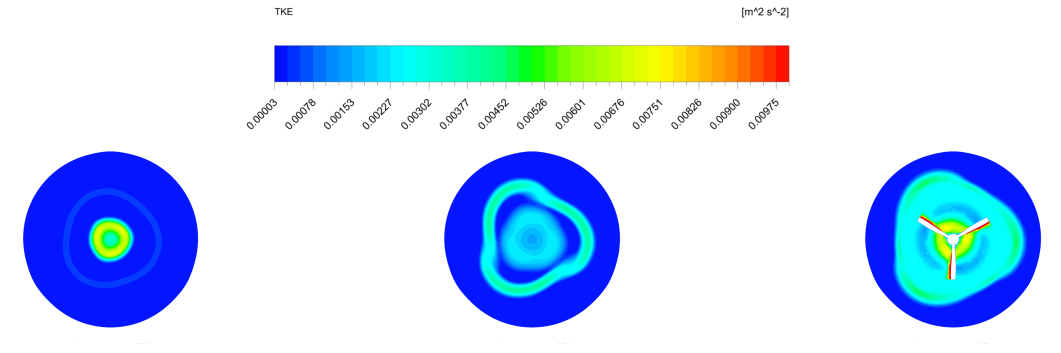

(a) 1D (b) 3D (c) 4D

(d) 5D (e) 7D (f) 10D

Figure 5.26: Front view of the turbulence kinetic energy of dual-rotor with X=4D at TSR 5 (front rotor, $\theta_T = 2°$), origin is located at the axis center of front rotor, TI =1% RANS

5.5 Analytical estimate of the additional power from the rear rotor

The previous section showed gains of 10% to 20% in power by operating the rear rotor when the BEM-Park model was adopted. To show this is of no coincidence of that particular turbine, an analytic estimate is given assuming the front rotor is optimally pitched while the rear rotor works entirely in post-stall conditions.

The relationship between inflow angle and axial and tangential induction factors(a and a') is defined as (Fig. 3.1b):

$$\tan\phi = \frac{U_\infty(1-a)}{\omega r(1+a')} = \frac{1-a}{TSR(1+a')x} \tag{5.8}$$

Where $x = r/R$. At high $TSR >> 1$, we can assume that $\phi << 1$ rad and $a' << 1$ [42, 137], thus

$$\phi = \frac{1-a}{TSR\,x} = \frac{\phi_T}{x} \tag{5.9}$$

Where the subscript T denotes blade tip condition. Linear aerodynamics is assumed, i.e. $C_L = C_{L\alpha}\alpha$ and the profile drag coefficient C_{D0} is assumed to be independent of AOA. Then the maximum C_P by the BEM model and when neglecting tip edge effects ;

$$C_{P,opt} = 0.5(TSR)^3\sigma\phi_T C_{L\alpha}(\phi_T - \theta_T) - 0.25\sigma C_{D0}(TSR)^3 \tag{5.10}$$

,where σ is the solidity of the rotor; $\sigma = Bc_{gr}/(\pi R)$. B is the number of the blades and c_{gr} is the blade mean geometric chord length. In deriving Eq. 5.10 it was assumed there is no or little variation in the $C_{L\alpha}$ and $C_{D0}D$ along the blade's span.

One can also show that for an optimal blade, its geometric twist follows $\theta = \theta_T/x$, where by the BEM model [123] ;

$$\theta_T = \frac{2}{3TSR_{opt}}(1 - \frac{8}{3TSR_{opt}C_{L\alpha}\sigma}) \tag{5.11}$$

and

$$\phi_T = \frac{2}{3TSR_{opt}} \tag{5.12}$$

Substituting Eqs 5.12 & 5.11 into Eq 5.10 and taking $C_{D0} = 0$ will yield the Betz limit, $C_{P,opt} = 16/27$. We shall assume that the front rotor has been optimized and performs as is predicted by Eq 5.10. Taking $C_{D0} = 0.02$, $\sigma = 0.1$ and $TSR = 4$, yields -0.032 for the second (viscous) term on the RHS of Eq5.10 and thus that term will be neglected.

On the other hand, the rear rotor blade is placed at the wrong pitch angle towards the flow and it is assumed that blades have totally stalled. A simplistic stall model is used for the profile hydrodynamics; $C_L = C_{L,max}$ and $C_D = C_{D,max}$ for $|\alpha| > \alpha_{stall}$. This yields after some manipulations and assuming $TSR >> 1$ [123];

$$C_{P,stall} = \frac{(TSR)^2\sigma C_{L,max}}{6} - \frac{8f(Y)}{(TSR)^4\sigma^2 C_{L,max}^2} - \frac{\sigma C_{D,max}(TSR)^3}{4} \tag{5.13}$$

where

$$f(Y) = \frac{Y^7}{7} - \frac{2Y^5}{5} + \frac{Y^3}{3} - \frac{8}{105} \quad \text{and} \quad Y = \sqrt{1 - 0.5\sigma C_{L,max}(TSR)^2} \tag{5.14}$$

Obviously this model holds as long as Y is a real number. Taking typical values of $C_{L,max} = 1$, $C_{D,max} = 0.1$, $\sigma = 0.1$, $TSR = 4$, yields the values of 0.27, 0.17 and -0.16 for the 1st, 2nd and 3rd terms on the RHS of Eq 5.13 respectively. Here, only the 1st term will be accounted.

The C_P of the rear rotor will be taken as of Eq 5.13 , but it is to be normalised according to the Eq. 5.3. Neglecting viscous effect for the front rotor yields $C_T \approx 8/9$ and assuming $C_{L\alpha}(\phi_T - \theta_T) = C_{L,max}$ for the front rotor leads to;

$$\frac{P_{rear}}{P_{front}} = (0.07, 0.12) \quad \text{for} \quad X = (2, 4)D \tag{5.15}$$

This is at lower end of the power gain estimates given in the section 5.4, where higher gains of up to 20% were recorded. This is because only part of the rear rotor operated in post-stall conditions, achieving high hydrodynamic efficiency towards the tip of the blade as in Fig. 5.9b.

5.6 Conclusion

A generic three-blades turbine was analysed, where it has a symmetric blade profiles, namely the NACA0012 and NACA0018. It is assumed the turbine was subject to a rotational speed control but not pitch and yaw controls. Such turbine is advantageous for a rectilinear tidal current of reversing directions. Two numerical methods were used for modelling, namely the BEM-Park model and CFD with RANS-based turbulence model k-ω SST. Power and thrust coefficients, mean axial velocities in the wake region were analysed using both methods, while the CFD results provided more details, such as velocity contours, TKE contours, and streamlines.

For a single-rotor, there was good agreement for Cp between BEM and CFD results, except when the rotor operated at hight TSR or turbulent wake state with negative pitched angle. For a dual-rotor, larger discrepancies were observed compared with single-rotor cases. The Cp of rear rotor obtained from BEM-Park model was higher than its CFD RANS counterpart. A gain of up to 20% in the overall C_P was recorded as relative to the C_P of just the front rotor, bringing the overall C_P to about 0.55 as long as the rear rotor operated at the optimum TSR as the front rotor. This is despite a significant part of the rear rotor towards the hub operated in post-stall conditions. The ambient TI is a key parameter for the C_P of rear rotor. A higher TI provided a higher Cp of rear rotor. This was the result of a faster recovery of velocity in the wake at higher TI. The effect of rotor spacing on the C_P of rear rotor was also analysed. For a rear rotor operated at TSR of 4-6 in the wake region, a slight rise of C_P was observed as the rotor spacing increased. A higher TSR had a negative effect on Cp of a dual-rotor. However, there was a monotonic increase of C_T as the rotor spacing increasing. A general analytical model based on the assumption of the front rotor working in optimal conditions while the rear rotor was fully in post-stall conditions gave an estimate of about 10% power gain from the rear rotor. This was viewed as the lower range of the power gain range due to the assumption of a fully-stalled rear rotor. The current investigation incorporated a symmetric profile as NACA0012 as comprise between the demands of the forward facing rotor and backwards facing one. As in the case of the vertical axis turbine further improvement can be sought by incorporating a symmetric profile with stall delay as of the CIRCLE-based that can particularly enhance blade hydrodynamic performance in a situation that is a comprise

between the two rotors and is not optimal for each of them. The current analysis did not account for effects from free surface waves and the BEM-Park model neglected swirl and radial non-uniformity in the wake between the two rotors. These effects can be further studied by improving the Park model for the rapid tool of the BEM approach. The time accurate URANS and LES simulation can also be used to improve the accuracy of the steady RANS that is approximation due to the assumption of moving reference frame for rotors, particularly for the rear rotor. Nevertheless, this research has pointed to the good potential power gain in operating a dual-rotor HAMCT that maximises the power from the rectilinear tidal current both directions without pitch or yaw control.

Chapter 6

Free surface wave effect on the performance of a HAMCT

6.1 Introduction

Although most of the HAMCT technology can be transferred from wind turbine, the existence of free surface pose a unique challenge for the HAMCT. The free surface wave adds transient periodic inlet velocity seen by the rotor. Meanwhile, its velocity is greatest at free surface, and decreases along the gravity direction. This mean there is greater potential kinetic energy near the free surface compared a location far from the free surface. However, the variation of velocity in the vertical direction introduces a sheared velocity profile, which increases the unsteadiness. Thus, the distance between the blade tip and mean free surface (tip clearance distance) is a key parameter for the performance and fatigue of a HAMCT.

The purpose of this study is to present an investigation of the effect of wave types, tip clearance distance, the free surface wave's amplitude and frequency on the loading and performance of a HAMCT. This investigation is part of a project aimed at investigating the viability of HAMCTs to provide energy to Indian remote islands. These turbines should show robustness, steady performance and minimum maintenance requirements. Flow unsteadiness caused by surface waves can adversely affect such turbines. For the study presented in this Chapter, we use the unsteady BEM approach as it is a rapid numerical solver enabling us to examine a wide range of wave variables at a low computational cost. It has already been demonstrated that such approach can reasonably predict well the turbine's time response to free surface waves [13, 36, 37]. More comprehensive method of CFD RANS has also been used as a complement. A simple sine wave is implemented by a User Defined Function (UDF). A detailed presentation of the BEM and CFD methods as given in Chapter 3, here a brief summary of our unsteady BEM and CFD approach are presented next, followed by results and analysis.

6.2 Numerical Methods

6.2.1 Turbine profile

For this study we chose to use the three-blades small scale model of Luznik [14] as the HAMCT. This is because Luznik conduced an experimental study of a HAMCT subjected to free surface waves. Meanwhile, our group already has good experience in studying its

blade profile E387 [138], and the BEM method requires good knowledge of the profile's lift and drag coefficients variation with the angle of attack. The turbine's diameter is 0.46 m and its hub was placed 0.782m beneath the undistributed water surface in a towing tank of 1.6 m depth.

6.2.2 Unsteady BEM method

We assume a submerged horizontal axis marine turbine (HAMCT) subject to a steady free stream speed U_∞, and the influence of gravity waves acting on the water surface, which we call free surface, see Fig.6.1(a). The free surface waves are modelled as Stokes waves, i.e. second order in amplitude, and their flow induced velocities are superimposed over the free stream speed U_∞. This leads to the flow instantaneous velocity vector;

$$\overline{u} = [U_\infty + u_r(z,t)]\hat{x} + w_r(z,t)\hat{z} \tag{6.1}$$

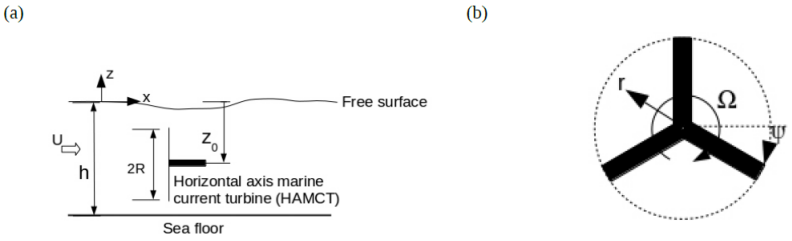

Figure 6.1: Schematic description of (a) the horizontal axis marine turbine configuration and (b) its rotor

In the Eq.6.1, $\hat{x}$ and $\hat{z}$ are unit velocity vectors in axial and vertical direction, while u_r and w_r are the axial and vertical Stokes wave velocities [74] at the location of the HAMCT, which we take as the instantaneous location of the blade's element while previous studies using the steady BEM used the location of the hub as the point to calculate u_r and w_r [37]. The explicit expressions of u_r and w_r are as follows [139]:

$$u_r = \frac{Hgk}{2(\omega - kU_\infty)} \frac{\cosh[k(z+h)]}{\cosh(kh)} \cos(\theta) + \frac{3H^2(\omega - kU_\infty)k}{16} \frac{cosh[2k(z+h)]}{\sinh(kh)^4} \cos(2\theta) \tag{6.2}$$

$$w_r = \frac{Hgk}{2(\omega - kU_\infty)} \frac{\sinh[k(z+h)]}{\cosh(kh)} \sin(\theta) + \frac{3H^2(\omega - kU_\infty)k}{16} \frac{\sinh[2k(z+h)]}{\sinh(kh)^4} \sin(2\theta) \tag{6.3}$$

and

$$\theta = kx - \omega t \tag{6.4}$$

where x is the axial coordinate, z is the vertical coordinate with origin located at the mean free surface level, h is the water depth, k is the wave number, H is the wave height, ω is the wave frequency, g is the gravity acceleration, and θ is the wave phase. Basically Stokes wave is a high order non-linear wave and we take the terms up to second order of kA , where A is the wave amplitude. A full mathematical description of Stokes waves is given in [74]. It is assumed that the wave length is long enough to neglect its axial variation along the control volume of the momentum calculation of the HAMCT at that

instant of time, which corresponds to the requirement of $kA < 1$. The wave frequency ω is related to its wave number k through the following dispersion relation [74];

$$(\omega - kU_\infty)^2 = gk \tanh(kh) \tag{6.5}$$

One should note that Eq. 6.5 accounts for the Doppler effect and thus there can be two positive roots of k for a given positive ω, which corresponds to a downstream propagating wave. Our interest lays in the longer wave (low k) as we expect the wave's velocities to decay as $exp(-|k|z)$ and thus the lower k is, the greater the effect of the wave is at deeper depths.

The loadings and power produced by the turbine are calculated using the unsteady BEM approach. In this section, we only give a brief summary of our approach. The interested reader can find more details on the various aspects of the steady and unsteady BEM methods in Chapter 3. The axial and tangential velocities seen by a radial element of the blade can be written as:

$$\overline{v}_{rel} = [U_\infty(1-a) + u_r(z,t)]\widehat{x} + [\Omega r(1+a') + w_r(z,t)cos(\psi)]\widehat{\psi} \tag{6.6}$$

where

$$d\psi/dt = \Omega \tag{6.7}$$

and ψ is the azimuthal angle, see Fig. 1b, $a(r,\psi)$ and $a'(r,\psi)$ are the axial and tangential velocity induction factors to be calculated by the BEM method. This is done by calculating the axial force and torque acting on each radial element of the blade using the momentum theory and the known hydrodynamics of the blade's profile. Both approaches must yield the same result and thus the two expressions for the axial force are required to yield the same value and the same holds for the torque expressions. This yields two non-linear equations for a and a' that typically are solved by a linear iterative solver. Please note that while for the steady BEM approach where uniform axial velocity is assumed, a and a' are taken as dependent only r and assumed to be identical for all the blades, in our case they can differ from blade to blade and they also depend on time as the azimuthal angle (ψ) varies with time.

At a high axial induction factor of $a > 0.4$, the wake behind the rotor becomes highly turbulent and thus the momentum expression for the axial force is no longer appropriate. It is replaced by Glauert's correction [7] in our calculation. Tip and hub losses are calculated using Prandtl's or Goldstein's loss factors. The variation of the blade's profile lift and drag coefficients with the angle of attack can be obtained from experimental data, free software as Xfoil and JavaFoil and CFD computations. Post-stall variation of the blade's profile lift and drag coefficients with the angle of attack are calculated using Viterna and Janetzke's empirical expressions [103].

The unsteadiness in the flow caused by u_r and w_r will cause unsteadiness in the blade's hydrodynamics and in the wake. The TUDK dynamic wake model is used to account for the wake's unsteadiness [7]. It is a relative simple engineering model that accounts for the time-delay of the turbine in reacting to the unsteadiness in the flow and is added as a correction after the steady BEM calculation. The unsteadiness in the blade profile's hydrodynamics is accounted using Theodorsen's theory for attached flow over an aerofoil and 0ye's dynamic stall model for when the flow becomes detached [140].

Small scale turbine blade's hydrodynamics like this one are sensitive to the Reynolds number more than their full scale counterparts. In this study we took the hydrodynamics of the blade of as of $Re_c = 10^5$ for $r < 0.7R$ and its tip as of 2×10^5 with linear variation

between them. As the TSR increases and the incoming velocity stays constant as in [14] the profile Reynolds number changes and thus re-distributing the hydro/aerodynamic data along the blade should improve the BEM accuracy for high TSR, but as noted above that level of TSR is not of strong operational interest.

6.2.3 CFD method

The computational domain (Fig. 6.2a) is subdivided into two sub-domains, one is stationary domain and another is rotational domain, which is implemented by a sliding mesh. The width of the computational domain is 6D, the depth is the same as water depth (1.6m), and the stream-wise length is 3L with 1L upstream of the rotor centre. A hybrid mesh (Fig.6.2b) is used to allow more flexibility of the computational domain. The inlet Boundary condition is specified as user defined velocity (Eq.6.1) by a user defined function (UDF), the outlet BC is specified as pressure outlet, and the symmetrical BC is used for the top, bottom, and lateral sides. The $k-\omega$ SST model is used for turbulence modeling and a time step size of 0.001s is implemented. The recommended time step size is no more than 1 degree per time step [141]. Also, the time step size should meet the Courant–Friedrichs–Lewy (CFL) condition for numerical stability requirement. The recommended CFL values are below 5 and 10 for explicit and implicit respectively [10]. All numerical simulation is conducted by ANSYS Fluent running on Apocrita cluster at QMUL.

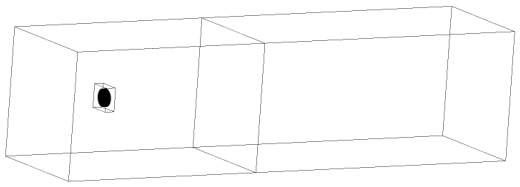

(a) Computational domain

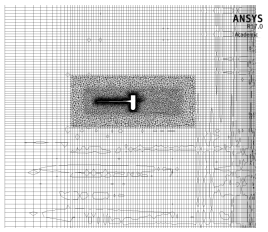

(b) Sectional view of the mesh at rotor center

Figure 6.2: Computational domain and mesh

6.3 Results and discussion

6.3.1 Validation

In this section, the steady and unsteady BEM code are used to get the performance and loading on a HAMCT and compare BEM results with baseline experimental results from Luznik [14]. The purpose of this section is to estimate the accuracy of performance and thrust based on BEM methods. Fig 6.3 (a) shows the BEM result of the variation of the power coefficient C_p with the tip speed ratio for the case with no surface waves. A very good agreement is revealed between the BEM results and the reported experimental

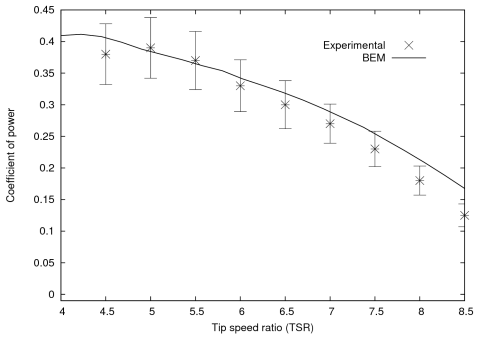

(a)

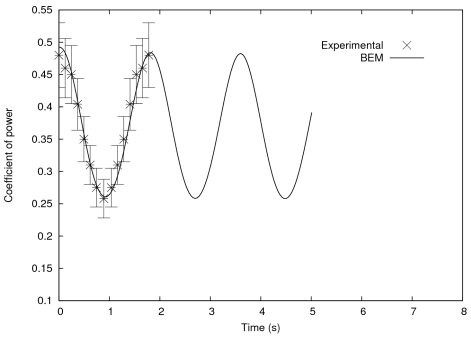

(b)

Figure 6.3: (a) The tip speed ratio variation of the time-averaged coefficient of power with no surface waves and (b) the time variation of the instantaneous coefficient of power for TSR=5.5, experimental data is from [13], BEM results

results [14], except for $TSR > 8$ which is of low importance as the C_P already declines to levels of no practical use.

The time variation of C_P when TSR=5.5 and with a small surface wave of an amplitude of 0.04 m and a time period of 1.78 s is shown in Fig 6.3 (b). The time oscillations of the C_P are very periodic (except at t=0 that is affected by the numerical initial condition) and correspond to the surface wave frequency. Again an excellent agreement with the experimental results is revealed. The peaks and troughs of C_P are in phase with the peaks and troughs of the surface wave. This can be explained by looking at the Stokes velocity potential [74]:

$$\phi = \mu_1 A \cosh[k(z+h)] sin(\theta) + \mu_2 A^2 \cosh[k(z+h)] \sin(2\theta) + ... \tag{6.8}$$

where the surface wave elevation is:

$$\eta = A\cos(\theta) + \mu_2 A^2 \cos(2z\theta) + ... \tag{6.9}$$

and

$$(u_r, w_r) = \nabla\phi \tag{6.10}$$

where μ_1 and μ_2 are positive expressions containing k, g, ω and U_∞. Thus u_r is in phase with η and it increases the axial velocity as seen by the turbine peaks, while one should note that C_p is defined as $P/(0.5\rho U_\infty^3 \pi R^3)$ and thus it can go above the Betz limit as u_r is added to U_∞ by the Eq.(6.1). A similar process was noted by [13, 14] but they more emphasized on w_r becoming zero at the peaks and troughs of C_P while we found this process to be more affected by u_r.

6.3.2 Parametric Study

In this section, the effects of wave types, wave amplitude, wave frequency, tip clearance distance are analyzed using BEM and CFD.

The first parameter is wave type. The sine wave is added at inlet by a UDF. Thus, the sine wave velocity is defined as:

$$u_r = Asin(\omega t) \tag{6.11}$$

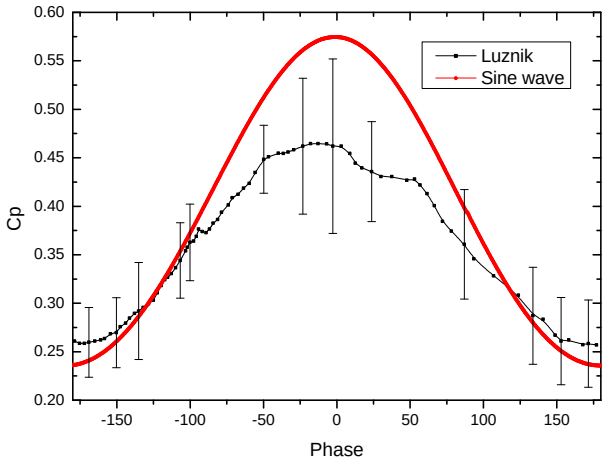

Figure 6.4: Cp versus instantaneous wave phase at TSR 5.5, CFD results (experimental result is from [14])

In the above equation, the amplitude and angular frequency of sine wave are the same as their counterparts of second Stokes wave used by Luznik [14].

Fig. 6.4 compares the impacts of a sine and second Stokes wave on the C_P of a HAMCT. The CFD C_P of a HAMCT subjected to sine wave is higher than its counterpart influenced by second Stokes wave during wave crest. This is in contrast to the good agreement between the experiment and unsteady BEM in the Fig.6.3b. Hence, despite the CFD having the potential of being more accurate than the unsteady BEM, the unsteady BEM provided more accurate results in this case. One reason is that the unsteady BEM could better for the induced velocity by the wave as seen in the Eq.6.1 than the simple approximation of the UDF inflow condition in the Eq. 6.11. It points to the need of 2nd Stokes wave by the UDF and two-phase simulation in the future. Fig.6.5 presents the horizontal and front views of the velocity contour of the HAMCT subjected to a combination of a sine wave and tidal current at TSR 5.5. An asymmetric velocity contour is formed in the wake region. Meanwhile, High velocity is observed near blade tips due to the rotation of blades. The wake velocity contours are presented in Fig.6.6. Unlike the axisymmetric contour of a HAMCT operating in a steady tidal current without free surface and seabed blockage that was studied in Ch4, the wake velocity is non-axisymmetric due to the wave and tidal current interaction.

For the rest of the chapter, we focus on the BEM results. The next parameter is the wave amplitude. Increasing the wave amplitude from 4 cm to 15 cm causes a significant increase in the amplitude of the fluctuations and a shift upwards in the time-averaged C_P as seen in Fig. 6.7b. Reducing the TSR from 5.5 to 4 while keeping the surface wave frequency the same causes a steepening of the time oscillations of C_P which is a hallmark of a non-linear interaction as seen in Fig.6.7a. This occurs because in a non-linear wave, the phase speed (ω/k) also depends on the instantaneous value of the property, e.g. C_P in Fig.6.7 and C_T in Fig.6.8, making the crest moving faster than the trough. Hence, the steepening occurs. It is also related to the fact that there is more than on dominant frequency as later discussed for the power spectra in Fig.6.11.

This is better seen in the time variation of the coefficient of thrust (drag) C_T presented in Figs. 6.8. A clear steepening is seen at TSR=4 and A=0.15 cm. C_T time averaged value is also reduced, while is less affected in TSR=5.5. The instantaneous radial distribution of d(Cp)/d(r/R) and (CT)/d(r/R) are shown in Figs 6.9 and 6.10 as expected the maximum

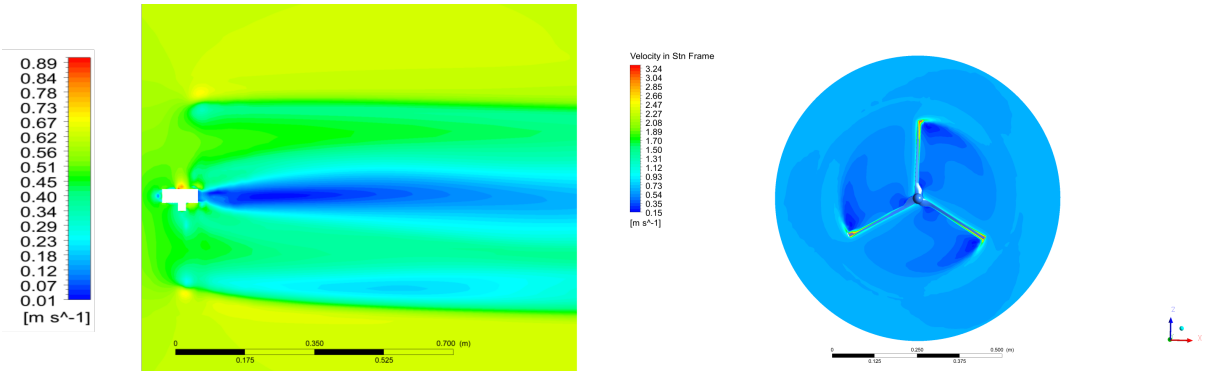

(a) (b)

Figure 6.5: Velocity contours on the horizontal plane (a) and rotational plane (b) at t=13.328s (sine wave, TSR 5.5, CFD results)

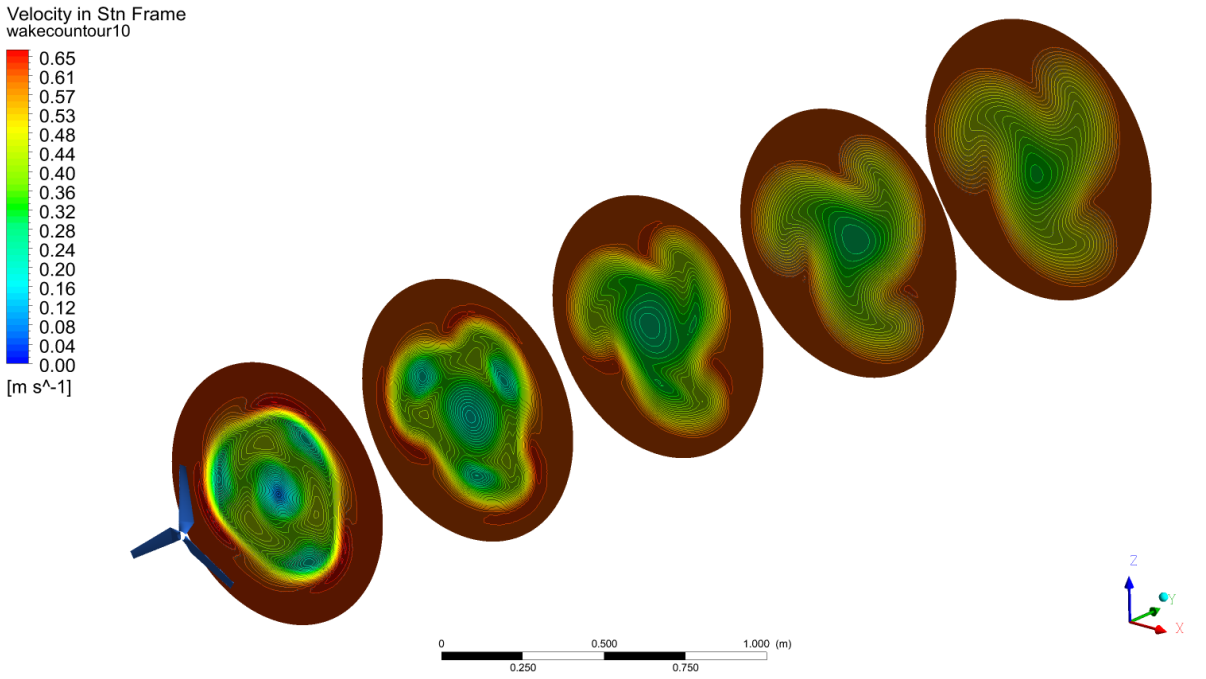

Figure 6.6: Velocity contours in the wake region at 1D, 3D, 5D,7D and 9D (sine wave,t=13.328s, TSR 5.5, CFD results)

occurs near the blade tip, before the tip loss factors reduce the load towards the tip. The difference between the crest (t=T/4) and trough (t=T/2) is higher for A=0.15 cm than A=0.04 cm in both cases of TSR and as expected. However, the distribution of TSR=4 at A=0.15 m less declines towards the hub than in TSR=5.5. The radial distribution of the thrust coefficient shows a similar behavior where TSR=4 shows a higher difference between the crest (t=T/4) and trough (t=T/2) as compared to TSR=5.5.

Finally, the power spectra of the coefficient of thrust are shown in Figs 6.11 for TSR =4 and 5.5. The power spectra is taken as the modulus of the complex discrete function

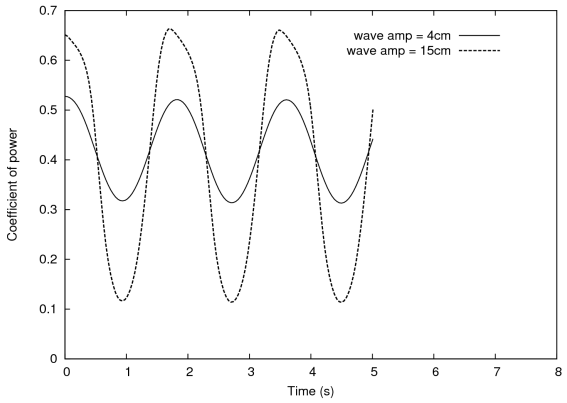

(a) $TSR = 4$

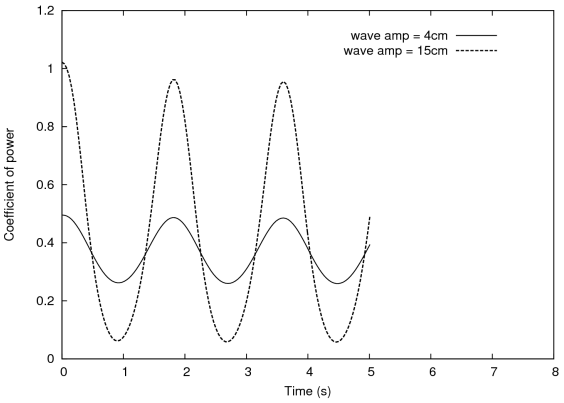

(b) $y = TSR = 5.5$

Figure 6.7: Time variation of the power coefficient,BEM results

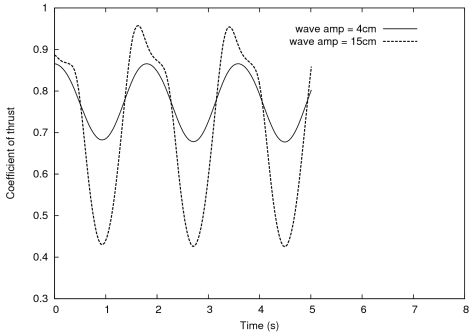

(a) TSR=4

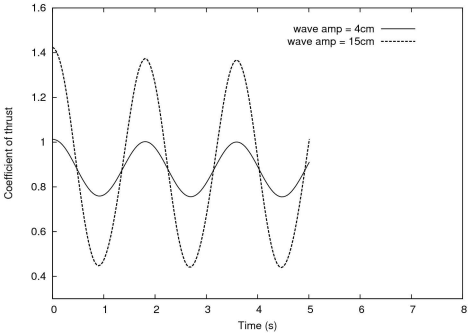

(b) TSR 5.5

Figure 6.8: Time variation of the thrust coefficient, BEM results

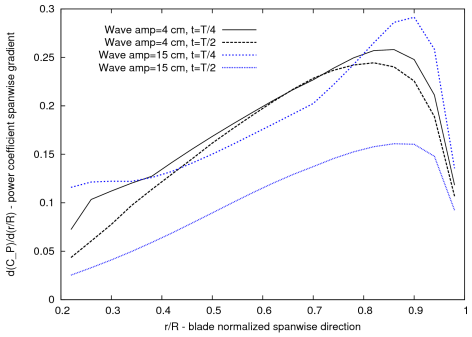

(a) $TSR = 4$

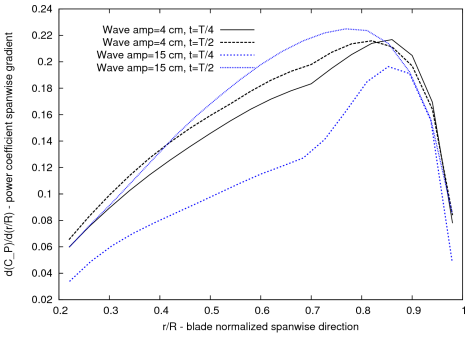

(b) $TSR = 5.5$

Figure 6.9: Spanwise distribution of the power coefficient, BEM results

$\hat{C_T}(\omega_i)$, i.e. $||\hat{C_T}(\omega_i)||$ [142]:

$$C_T(t) = \sum_{i=-N/2}^{i=N/2} \hat{C_T}(\omega_i) e^{j\omega_i t}, \text{and } \omega_i = \frac{2\pi \cdot i}{T} \tag{6.12}$$

where $j = \sqrt{-1}$, T is the time period of the sampling and $N/2$ is the number of points in the sampling. Since $C_T(t)$ is a real function:

$$\hat{C_T}(\omega_i) = \text{conjugate}[\hat{C_T}(-\omega_i)] \tag{6.13}$$

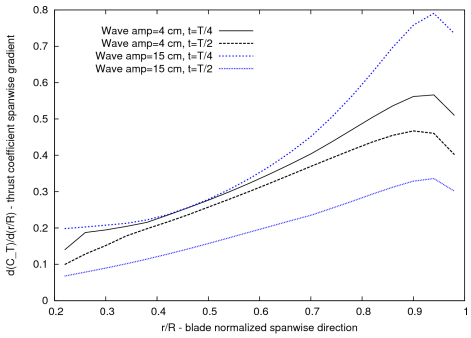

(a) $TSR = 4$

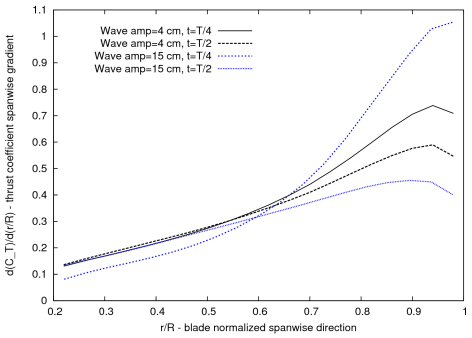

(b) $TSR = 5.5$

Figure 6.10: Spanwise distribution of the power coefficient,BEM results

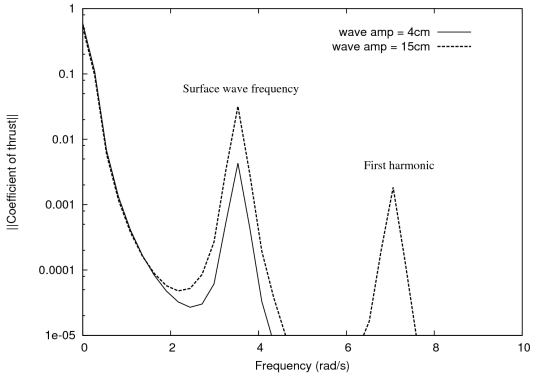

(a) $TSR = 4$

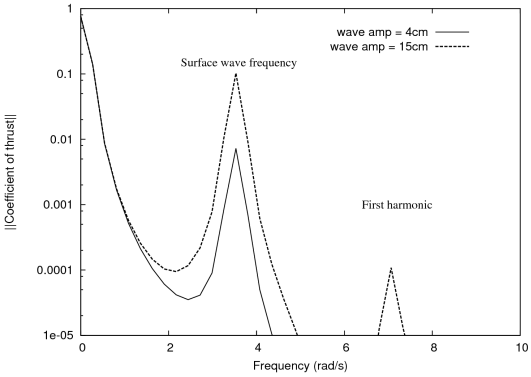

(b) $TSR = 5.5$

Figure 6.11: Power spectra of thrust coefficient, BEM results

Here, what is seen in Fig.6.12 is twice of the modulus of $C_T\hat{(}\omega_i)$ to account for the negative (opposite phase) frequency. Power spectra are notoriously noisy due to any mild non-periodicity, although windowing was used [142]. Nevertheless the surface wave frequency is clearly evident in both cases of $TSRs$ and is noted on the figures. The first harmonic is also evident for $A = 0.15cm$ and much clearer for $TSR = 4$ than for $TSR = 5.5$, pointing again towards non-linear interaction for low $TSRs$. The first harmonic can be related to the second term in Eq.6.8. Its significant increase with the increase in A shows the non-linear effect in the generation of C_T, where the increase in A to $15cm$ causes a relative larger increase in the first harmonic as compared to the use of $A = 4cm$ than on the fundamental frequency. The stronger increase in the non-linearity for $TSR = 4$ than for $TSR = 5$ corresponds to the non-linearity of the wave steepening seen in Figs.6.7 and 6.8.

Figure 6.12 (a) presents the effect of wave frequency on the C_P of a rotor operating at TSR 4, where Ω is the turbine angular velocity and ω is the wave angular velocity. For example, at $\omega/\Omega = 0.34$, the turbine rotational period is 0.60s, while the wave period is 1.78s, which is the wave period used in reference [14]. A higher amplitude of fluctuation is observed when the ω/Ω value slumps from 1 to 0.34. For example, a high 30% amplitude of fluctuation of C_P is recorded when the rotor operates at $\omega/\Omega = 0.34$ (solid line). When the rotor and wave are in phase ($\omega/\Omega = 1$, dot-dash line), the amplitude of fluctuation of C_P is only as low as 2.5%. This trend is consistent with the research work done by Tatum et al [143] who compared the C_P and C_T of a rotor subjected to modified linear

airy wave with two different wave frequencies. For the effect of wave frequency on the C_T of a HAMCT, a similar trend is observed at different wave frequencies as seen in Fig.6.12 (b). However, the circle averaged values of C_P and C_t are not affected by the wave frequency. In conclusion, for a rotor operating at the optimal TSR, a longer wave period has a stronger fluctuations on C_P and C_T, which have an adverse effect on power production and blade fatigue life.

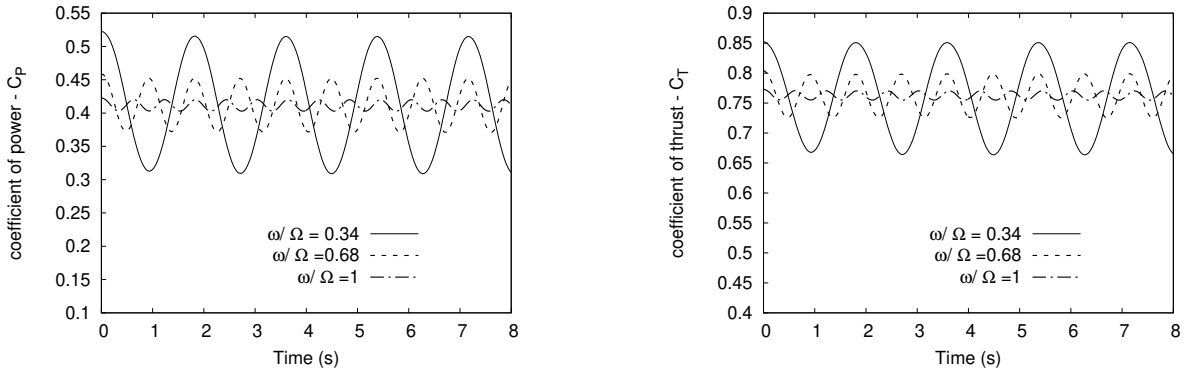

Figure 6.12: Power and thrust coefficients at different wave frequencies, TSR=4, BEM results

The tip clearance is referred as the distance between the blade tip and the mean free surface level. The vertical velocity of a wave is variable in the gravity direction, thus the tip clearance affects the velocity seen by the rotor. Meanwhile, there is a strong interaction between the blade and wave when the rotor blade is close to the free surface. Thus, the blade tip clearance is a key parameter for the deployment of a HAMCT.

Noruzi [15] studied the effect of installation depth on a HAMCT subjected to linear wave using BEM and CFD and concluded that the performance is significantly affected when the installation depth is below 20 % of water depth. However, a 120° computational domain and an axisymmetric assumption were used by the author, which are not appropriately because the axisymmetric assumption is not valid as the wave velocity is a function of z and non-axisymmetric. A recent experimental work was done by Katsutoshi et al. [79], who tested a scale model of kite-like turbine in a circulating water channel with linear wave generator [79]. The turbine was placed at different depth below the mean water level to analysis the wave impact on mooring line tension. The results showed that thrust of turbine is influenced by wave when the nacelle depth is half wave length, but not the case when the nacelle depth is slightly greater than the wavelength.

Figure 6.13 represents the vertical distribution of the normalized axial and vertical wave velocity. The vertical distance is normalized by the water depth, h, while the wave velocity profiles are normalized by the mean current velocity, U_∞, which is 0.6 m/s in this case. Horizontal lines are the levels of blade tips in the vertical direction. The maximum horizontal and vertical wave velocities are located at the mean free surface level. Both horizontal and vertical velocities decrease steadily in the gravity direction. The effect of blade tip clearance on the C_P and C_T is presented in Figures 6.14 (a) and (b). As the blade tip clearance declines, the amplitude of fluctuation of both C_P and C_T increases. The Cp varies from 0.27-0.56 when the rotor is placed near the free surface with a blade tip clearance of $0.1h$, which is represented as a cross point. When the rotor is located in a position with a large tip clearance such as 0.5h, a smaller fluctuation of C_P is observed, which varies from 0.33 to 0.51. When the blade tip clearance is $0.1h$, the fluctuation range

of C_T is 0.63-0.87. Its range narrows down to 0.68-0.84 when the blade tip clearance is down to $0.5h$. Although a much stronger fluctuation of thrust as the reduction of tip clearance, the maximum C_T value is still below 1, which is a tipping point of turbulent wake. The amplitude of fluctuation of C_T is closely related to the structural vibration of a HAMCT. Generally, a higher amplitude of fluctuation of blade loading is more likely to accelerate the structural fatigue, although the cyclic averaged value deviates little from the steady case.

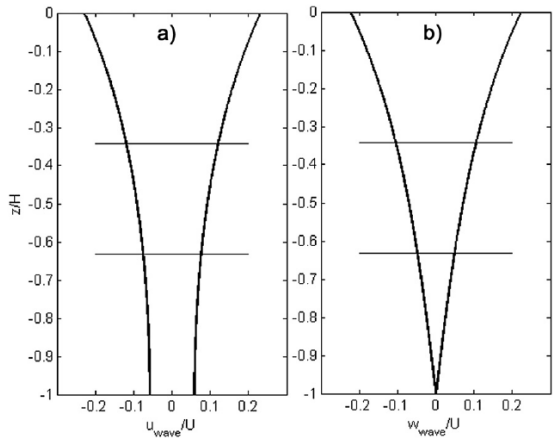

Figure 6.13: Normalized axial and vertical wave velocity profiles as relative to mean current velocity (0.6 m/s) [15]

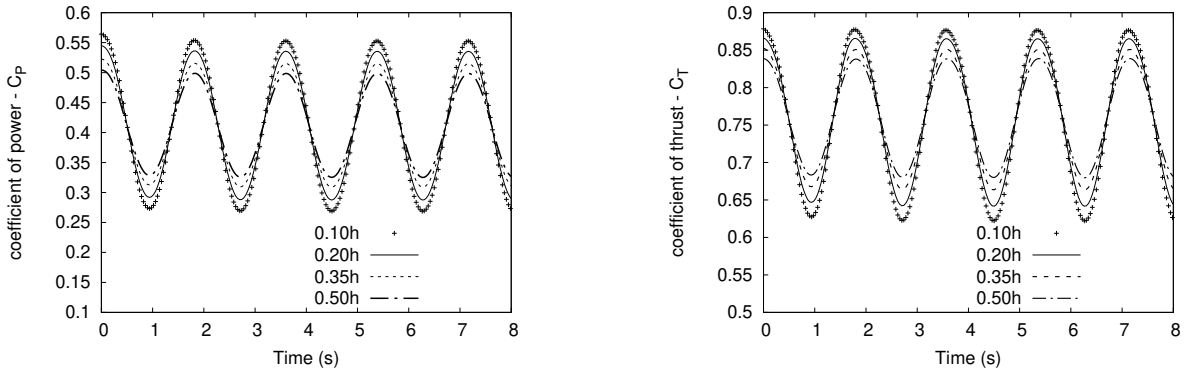

Figure 6.14: Power and thrust coefficients at different normalized tip clearance distance, TSR=4

6.4 Summary

Hydrodynamic calculations based on the unsteady BEM method and CFD have been pursued to assess the effect of free surface waves on marine current turbines (HAMCTs). Very good agreement between the BEM calculations and experimental results of a small scale HAMCT were found both for the time averaged and time varying coefficient of power with a small amplitude surface wave. A method was tested to reduce the computational cost using CFD by developing one-phase unsteady RANS coupled with an inflow velocity condition mimicking the effect of the free surface induced axial velocity.

Although it produced a behaviour of the C_P similar to that recorded by the available experimental results and the unsteady BEM. It over predicted the C_P value, pointing to need to have more accurate CFD modelling using for example two-phase (water and air). Unlike previous BEM studies, the unsteady BEM approach also accounted for the induced vertical wave velocity.

It was shown that large waves, but still long in sense of $kA < 1$ can affect in different ways the turbine performance by changing its time averaged coefficients of thrust and power while introducing non-linear behaviour in the time variations of those coefficients, particularly for low TSR. It also exhibited in a noticeable first harmonic of the surface wave affecting the turbine time-response. Higher blade loading was found near the tip as expected, but with larger time variation (i.e. blade location) as the wave amplitude was increased. This can have an effect on the blade's vibration. Effects of frequency ratio between the wave and turbine was also studied as well as the blade's tip clearance from the free surface.

In the future, a more detailed CFD study using two-phase flow RANS approach can be carried out. It will better account for turbulence effect and any risk of cavitation. However, current results indicate that for this HAMCT the risk of turbulent wake is low because C_T has value below 1. As for cavitation, ΩR for turbine's time period of 0.6s is 2.4 m/s or the dynamic pressure of $0.5\rho(\Omega R)^2 = 2880Pa$, which is low as compared to atmospheric pressure if we assume the blade tip is very close to the free surface. Hence, cavitation is of low risk for this HAMCT.

Chapter 7

Conclusions and further reseach

7.1 Summary and conclusions

This project has sought paths of hydrodynamic improvement for a common three blade horizontal axis marine current turbine, three paths were studied:

1. Replacing the blade profile with a redesigned profile using the CIRCLE method. The latter calls for a continuous curvature of the blade surface. Both steady BEM and CFD-RANS were used to estimate the HAMCT. Both methods showed that the A7 mildly outperform the E387 turbine at low TSRs for that particular geometric configurations. Hence, the A7 mildly increased the operational range of the original turbine. Further optimization was pursued by varying the blade's chord length and pitch angle using the Burton's and implicit models derived from the momentum theory. BEM calculations showed increase of 13% in the $C_{P,max}$ of both the E387 and A7 turbine due this optimisation procedure.

2. The second part of the study is to design a dual-rotor MCT without yaw and pitch controls, which operates in a rectilinear (direction-reversing) tidal current environment. The studied dual rotor configurations, had each rotor configured to face the free stream from its side, i.e. left rotor configured to face the stream coming from left by correctly placing the pitch angle and vice versa the right rotor. The BEM-Park model was proposed to predict the total power performance and thrust loading of such a dual-rotor MCT. Since the Park wake model is quite simplified and not accounting for swirl, CFD-RANS was used to assess it. It was found that turbulence and swirl may stay inside the wake between the rotors depending on the state of the front rotor. It was found that the dual rotor configuration can reach a combined C_P of up to 0.55 when the blade profile Reynold's number is 1M. This corresponded to a middle size turbine of about 3.5m diameter. Analytical derivation based on the BEM approach showed that an increase of about 10% can achieved for C_P when both rotors operate at the same TSR. However, analytical model assumed a simplistic post-stall aerodynamic profile model of constant C_L and C_D in post stall conditions.

3. The final case is the effect of free surface waves on the hydrodynamic performance of a single rotor HAMCT. The unsteady BEM method of dynamic wake coupled with non-linear Stokes surface wave theory was used as the main tool. Excellent agreement was achieved with literature-base experimental results for a HAMCT

subject to a small wave. Good agreement was also achieved with CFD-RANS of a single phase, where the free surface wave effect was modelled using the analytical expressions for the wave induced horizontal velocity as inflow condition. The latter was put through a user defined function in the ANSYS software. The agreement pointed to the option of HAMCT subject to free surface wave using a single phase approximation. But it also showed the robustness of the unsteady BEM-free surface wave theory approach. Hence, the unsteady BEM-free surface wave theory approach was used to further investigate the effect of large amplitude wave. For the first time, a non-linear time response in terms of power and thrust was identified. This happened at low TSRs. Further study included analysis the effect of the wave amplitude, frequency ratio between the wave and the turbine rotor and blade tip clearance. Blade loading and power spectra were also analyzed.

7.2 Further research

The numerical tools of this project are the steady and unsteady BEM methods, and the CFD-RANS approach. These methods can be further improved.

The Park model for the dual-rotor case is rather simplistic, new calibration is indicated based on the evolution of the mean axial velocity in the wake region obtained from the CFD-RANS. This requires further computations in order to yield better estimates of the new calibration of constants in the Park model. Such calculations can include swirl in the wake between the rotors to be coupled into the BEM approach as was done for aero coaxial rotors [144]. The unsteady BEM can be introduced instead of the steady BEM for the HAMCT dual rotor. Finally a CFD-BEM can replace the BEM-Park approach to account for the pillar effect.

The free surface wave effect can be further studied using a two-phase CFD approach. However, this will require significant computational resources to calculate a significantly large computational domain that includes at least three wave lengths in axial direction and both air and water in vertical direction.

The CFD-BEM approach can be used to reduce the computational cost, but this will have to be validated against a large scale simulation based on LES or DES. Such approach again will be able to account for the effect of the pillar. Such effect may be incorporated into the unsteady BEM using a wake model similar to Park's if the rotor is downstream facing (as relative to the pillar). Finally, one may wish to investigate other HAMCTs configuration composed of two or four blades rotor and a farm of HAMCTs.

References

[1] C. Lins, E. Musolino, K. Petrichenko, W. Rickerson, J. Sawin, K. Seyboth, J. Skeen, B. Sovacool, F. Sverrisson, and L. Williamson, "Renewables 2017 global status report," 2017. ix, 1

[2] "Atlantis unveils the world's largest tidal turbine - the ak1000." `https://simecatlantis.com/2010/08/11/atlantis-unveils-the-worlds-largest-tidal-turbine-the-ak1000/`. Accessed: 2018-05-30. ix, 4

[3] B. L. Méhauté, *An Introduction to Hydrodynamics and Water Waves*. Springer-Verlag, 1976. ix, 6

[4] J. Orme, I. Masters, and C. Mima, "Analysis and comparison of support structure concepts for tidal stream turbines," in *Proceedings of World Maritime Technology Conference*, 2006. ix, 12, 13

[5] B. Huang, Y. Nakanishi, and T. Kanemoto, "Numerical and experimental analysis of a counter-rotating type horizontal-axis tidal turbine," *Journal of Mechanical Science and Technology*, vol. 30, no. 2, pp. 499–505, 2016. ix, 20, 21

[6] J. Clarke, G. Connor, A. Grant, C. Johnstone, and S. Ordonez-Sanchez, "Analysis of a single point tensioned mooring system for station keeping of a contra-rotating marine current turbine," *IET Renewable Power Generation*, vol. 4, no. 6, pp. 473–487, 2010. cited By 9. ix, 21

[7] M. Hansen, "Aerodynamics of wind turbine 2nd edition," 2008. ix, 12, 23, 24, 26, 27, 73

[8] R. E. Wilson and P. B. Lissaman, "Applied aerodynamics of wind power machines," *NASA STI/Recon Technical Report N*, vol. 75, 1974. ix, 26

[9] D. M. Eggleston and F. Stoddard, *Wind turbine engineering design*. Van Nostrand Reinhold Co. Inc., New York, NY, 1987. ix, 26

[10] Fluent, "Ansys fluent theory guide," *Ansys Inc*, 2017. ix, 14, 30, 31, 32, 33, 34, 52, 74

[11] X. Shen, E. Avital, G. Paul, M. A. Rezaienia, P. Wen, and T. Korakianitis, "Experimental study of surface curvature effects on aerodynamic performance of a low reynolds number airfoil for use in small wind turbines," *Journal of Renewable and Sustainable Energy*, vol. 8, no. 5, p. 053303, 2016. ix, 3, 37, 38, 39

[12] B. H. Park and Y. O. Han, "Steady aerodynamic characteristics of two-dimensional naca0012 airfoil for one revolution angle of attack," *International Journal of Aeronautical & Space Sciences*, pp. 1–14, 2018. x, 54, 55

[13] E. E. Lust, L. Luznik, K. A. Flack, J. M. Walker, and M. C. Van Benthem, "The influence of surface gravity waves on marine current turbine performance," *International Journal of Marine Energy*, vol. 3, pp. 27–40, 2013. xi, 2, 17, 71, 75

[14] L. Luznik, K. A. Flack, E. E. Lust, and K. Taylor, "The effect of surface waves on the performance characteristics of a model tidal turbine," *Renewable energy*, vol. 58, pp. 108–114, 2013. xi, 6, 17, 37, 40, 49, 50, 51, 71, 74, 75, 76, 79

[15] R. Noruzi, M. Vahidzadeh, and A. Riasi, "Design, analysis and predicting hydrokinetic performance of a horizontal marine current axial turbine by consideration of turbine installation depth," *Ocean Engineering*, vol. 108, pp. 789–798, 2015. xi, 16, 18, 80, 81

[16] S. R. Massel, *Ocean surface waves, their physics and prediction*. World scientific, 2017. xiii, 5

[17] B. Drew, A. Plummer, and M. Sahinkaya, "A review of wave energy converter technology," *Proceedings of the Institution of Mechanical Engineers, Part A: Journal of Power and Energy*, vol. 223, no. 8, pp. 887–902, 2009. cited By 441. 1

[18] R. H. Charlier, "A "sleeper" awakes: tidal current power," *Renewable and Sustainable Energy Reviews*, vol. 7, no. 6, pp. 515–529, 2003. 2

[19] "Tidal barrage generation." `http://www.alternative-energy-tutorials.com/tidal-energy/tidal-barrage.html`. Accessed: 2018-10-30. 2

[20] "Bluewater energy services." `http://www.emec.org.uk/about-us/our-tidal-clients/bluewater-energy-services/`. Accessed: 2018-10-30. 2

[21] R. Eppler, *Airfoil Design and Data*. Springer-Verlag Berlin Heidelberg, 1990. 2

[22] R. K. Singh, M. R. Ahmed, M. A. Zullah, and Y. H. Lee, "Design of a low reynolds number airfoil for small horizontal axis wind turbines," *Renewable Energy*, vol. 42, no. 1, pp. 66–76, 2012. 2

[23] P. Jeffcoate, T. Whittaker, C. Boake, and B. Elsaesser, "Field tests of multiple 1/10 scale tidal turbines in steady flows," *Renewable Energy*, vol. 87, pp. 240–252, 2016. 2

[24] M. S. Selig and B. D. McGranahan, "Wind tunnel aerodynamic tests of six airfoils for use on small wind turbines; period of performance: October 31, 2002–january 31, 2003," tech. rep., National Renewable Energy Laboratory (NREL), Golden, CO., 2004. 3, 38, 40

[25] H. Hodson, "Boundary-layer transition and separation near the leading edge of a high-speed turbine blade," *Journal of Engineering for Gas Turbines and Power*, vol. 107, no. 1, pp. 127–134, 1985. 3

[26] T. Korakianitis, I. Hamakhan, M. Rezaienia, A. Wheeler, E. Avital, and J. Williams, "Design of high-efficiency turbomachinery blades for energy conversion devices with the three-dimensional prescribed surface curvature distribution blade design (circle) method," *applied Energy*, vol. 89, no. 1, pp. 215–227, 2012. 3

[27] T. Korakianitis, M. Rezaienia, I. Hamakhan, and A. Wheeler, "Two-and three-dimensional prescribed surface curvature distribution blade design (circle) method for the design of high efficiency turbines, compressors, and isolated airfoils," *Journal of Turbomachinery*, vol. 135, no. 4, p. 041002, 2013. 3

[28] T. Korakianitis, "Hierarchical development of three direct-design methods for two-dimensional axial-turbomachinery cascades," *Journal of turbomachinery*, vol. 115, no. 2, pp. 314–324, 1993. 3

[29] I. Hamakhan and T. Korakianitis, "Aerodynamic performance effects of leading-edge geometry in gas-turbine blades," *Applied Energy*, vol. 87, no. 5, pp. 1591–1601, 2010. 3

[30] T. Korakianitis, M. Rezaienia, I. Hamakhan, E. Avital, and J. Williams, "Aerodynamic improvements of wind-turbine airfoil geometries with the prescribed surface curvature distribution blade design (circle) method," *Journal of engineering for gas turbines and power*, vol. 134, no. 8, p. 082601, 2012. 3

[31] Y. Song, C.-W. Gu, and Y.-B. Xiao, "Numerical and theoretical investigations concerning the continuous-surface-curvature effect in compressor blades," *Energies*, vol. 7, no. 12, pp. 8150–8177, 2014. 3

[32] S. B. Elghali, M. Benbouzid, and J. F. Charpentier, "Marine tidal current electric power generation technology: State of the art and current status," in *Electric Machines & Drives Conference, 2007. IEMDC'07. IEEE International*, vol. 2, pp. 1407–1412, IEEE, 2007. 4

[33] O. Singha, N. Venkatesan, A. Samad, and E. Avital, "Modeling and controller implementation of tidal turbine for indian remote islands," in *Mechanical and Aerospace Engineering (ICMAE), 2016 7th International Conference on*, pp. 279–284, IEEE, 2016. 4

[34] Y. Dong, Y. Zhao, W. Zhu, X. Zhang, and J. Guo, "Development of a simple power controller for horizontal-axis standalone tidal current energy generation system," *International Journal of Global Energy Issues*, vol. 40, no. 1-2, pp. 117–127, 2017. 4

[35] A. Bahaj, A. Molland, J. Chaplin, and W. Batten, "Power and thrust measurements of marine current turbines under various hydrodynamic flow conditions in a cavitation tunnel and a towing tank," *Renewable energy*, vol. 32, no. 3, pp. 407–426, 2007. 5, 15

[36] N. Barltrop, K. Varyani, A. Grant, D. Clelland, and X. Pham, "Investigation into wave'current interactions in marine current turbines," *Proceedings of the Institution of Mechanical Engineers, Part A: Journal of Power and Energy*, vol. 221, no. 2, pp. 233–242, 2007. 6, 17, 71

[37] P. W. Galloway, L. E. Myers, and A. S. Bahaj, "Quantifying wave and yaw effects on a scale tidal stream turbine," *Renewable Energy*, vol. 63, pp. 297–307, 2014. 6, 17, 71, 72

[38] I. Power, J. K. Seacore, and G. Kassel, "Sea flow-world's first pilot project for the exploitation of marine currents at a commercial scale," *Final Publishable Report*, pp. 1–34, 2005. 9, 10

[39] "tidal turbine." `https://www.atlantisresourcesltd.com/services/turbines`. Accessed: 2015-05-30. 9

[40] "Seagen s." `http://www.marineturbines.com/SeaGen-Products/SeaGen-S`. Accessed: 2015-05-30. 10

[41] "tidal devices." `http://www.emec.org.uk/marine-energy/tidal-devices/`. Accessed: 2018-01-18. 9

[42] T. Korakianitis, M. Rezaienia, X. Shen, E. Avital, A. Munjiza, P. Wen, and J. Williams, "Aerodynamics of wind turbine technology," *Handbook of Clean Energy Systems*, 2015. 10, 26, 68

[43] S. Quayle and A. Rennie, "Integrating computational fluid dynamic and prototyping technologies in the investigation of multi-element profiles for a high-lift variable pitch vertical-axis tidal power generator," *International Journal of Agile Systems and Management*, vol. 2, no. 2, pp. 222–236, 2007. 10

[44] M. Lesieur, "Turbulence in fluids: stochastic and numerical modeling," *NASA STI/Recon Technical Report A*, vol. 91, p. 24106, 1990. 13

[45] P. Kundu and I. Cohen, "Fluid mechanics. 2004," *Elsevier Academic Press, San Diego). Two-and three-dimensional self-sustained flow oscillations*, vol. 307, pp. 471–476, 2008. 14

[46] Wilcox and DavidC, *Turbulence modeling for CFD / 3rd ed.* DCW Industries, 2006. 14, 30, 31

[47] E. E. Lust, K. A. Flack, and L. Luznik, "Survey of the near wake of an axial-flow hydrokinetic turbine in quiescent conditions," *Renewable Energy*, vol. 129, pp. 92–101, 2018. 15

[48] P. Mycek, B. Gaurier, G. Germain, G. Pinon, and E. Rivoalen, "Experimental study of the turbulence intensity effects on marine current turbines behaviour. part i: One single turbine," *Renewable Energy*, vol. 66, pp. 729–746, 2014. 15

[49] E. Osalusi, J. Side, and R. Harris, "Reynolds stress and turbulence estimates in bottom boundary layer of fall of warness," *International Communications in Heat and Mass Transfer*, vol. 36, no. 5, pp. 412–421, 2009. 15

[50] I. A. Milne, R. N. Sharma, R. G. Flay, and S. Bickerton, "Characteristics of the turbulence in the flow at a tidal stream power site," *Phil. Trans. R. Soc. A*, vol. 371, no. 1985, p. 20120196, 2013. 15

[51] J. Thomson, B. Polagye, V. Durgesh, and M. C. Richmond, "Measurements of turbulence at two tidal energy sites in puget sound, wa," *IEEE Journal of Oceanic Engineering*, vol. 37, no. 3, pp. 363–374, 2012. 15

[52] J. MacEnri, M. Reed, and T. Thiringer, "Influence of tidal parameters on seagen flicker performance," *Phil. Trans. R. Soc. A*, vol. 371, no. 1985, p. 20120247, 2013. 15

[53] Y. Li, J. A. Colby, N. Kelley, R. Thresher, B. Jonkman, and S. Hughes, "Inflow measurement in a tidal strait for deploying tidal current turbines: lessons, opportunities and challenges," in *ASME 2010 29th international conference on ocean, offshore and arctic engineering*, pp. 569–576, American Society of Mechanical Engineers, 2010. 15

[54] P. G. Novo and Y. Kyozuka, "Field measurement and numerical study of tidal current turbulence intensity in the kobe strait of the goto islands, nagasaki prefecture," *Journal of Marine Science and Technology*, vol. 22, no. 2, pp. 335–350, 2017. 15

[55] E. E. Lust, *The Influence of Surface Gravity Waves on the Performance and Near-Wake of an Axial-Flow Marine Hydrokinetic Turbine*. PhD thesis, University of Maryland, 2017. 15

[56] Y. Zhang, J. Zhang, Y. Zheng, C. Yang, W. Zang, and E. Fernandezrodriguez, "Experimental analysis and evaluation of the numerical prediction of wake characteristics of tidal stream turbine," *Energies*, vol. 10, no. 12, p. 2057, 2017. 15

[57] L. Chernin and D. V. Val, "Probabilistic prediction of cavitation on rotor blades of tidal stream turbines," *Renewable Energy*, 2017. 15

[58] W. M. J. Batten, A. S. Bahaj, A. F. Molland, and J. R. Chaplin, "The prediction of the hydrodynamic performance of marine current turbines," *Renewable Energy*, vol. 33, no. 5, pp. 1085–1096, 2008. 16

[59] A. S. Bahaj, W. M. J. Batten, and G. Mccann, "Experimental verifications of numerical predictions for the hydrodynamic performance of horizontal axis marine current turbines," *Renewable Energy*, vol. 32, no. 15, pp. 2479–2490, 2007. 16

[60] I. Masters, A. Williams, T. N. Croft, M. Togneri, M. Edmunds, E. Zangiabadi, I. Fairley, and H. Karunarathna, "A comparison of numerical modelling techniques for tidal stream turbine analysis," *Energies*, vol. 8, no. 8, pp. 7833–7853, 2015. 16, 32

[61] I. Masters, J. C. Chapman, M. R. Willis, and J. A. C. Orme, "A robust blade element momentum theory model for tidal stream turbines including tip and hub loss corrections," *Journal of Marine Engineering & Technology*, vol. 10, no. 1, pp. 25–35, 2011. 16

[62] R. Malki, I. Masters, A. J. Williams, and T. N. Croft, "Planning tidal stream turbine array layouts using a coupled blade element momentum–computational fluid dynamics model," *Renewable Energy*, vol. 63, pp. 46–54, 2014. 16, 18, 32

[63] R. Malki, A. J. Williams, T. N. Croft, M. Togneri, and I. Masters, "A coupled blade element momentum – computational fluid dynamics model for evaluating tidal stream turbine performance," *Applied Mathematical Modelling*, vol. 37, no. 5, pp. 3006–3020, 2013. 16

[64] A. Williams, T. Croft, I. Masters, C. Bennett, S. Patterson, and M. Willis, "A combined bem-cfd model for tidal stream turbines," in *3rd International Conference on Ocean Energy. Bilbao, Spain*, 2010. 16, 32

[65] M. Edmunds, R. Malki, A. Williams, I. Masters, and T. Croft, "Aspects of tidal stream turbine modelling in the natural environment using a coupled bem–cfd model," *International Journal of Marine Energy*, vol. 7, pp. 20–42, 2014. 16

[66] I. Masters, R. Malki, A. J. Williams, and T. N. Croft, "The influence of flow acceleration on tidal stream turbine wake dynamics: A numerical study using a coupled bem–cfd model," *Applied Mathematical Modelling*, vol. 37, no. 16-17, pp. 7905–7918, 2013. 16

[67] T. Leroux, N. Osbourne, and D. Groulx, "Numerical study into horizontal tidal turbine wake velocity deficit: Quasi-steady state and transient approaches," *Ocean Engineering*, vol. 181, pp. 240–251, 2019. 17

[68] B. Abuan and R. Howell, "The performance and hydrodynamics in unsteady flow of a horizontal axis tidal turbine," *Renewable Energy*, pp. 1338–1351, 2019. 17

[69] A. Olczak, T. Stallard, T. Feng, and P. Stansby, "Comparison of a rans blade element model for tidal turbine arrays with laboratory scale measurements of wake velocity and rotor thrust," *Journal of Fluids and Structures*, vol. 64, pp. 87–106, 2016. 17

[70] S. Muchala and R. Willden, "Influence of support structures on tidal turbine power output," *Journal of Fluids and Structures*, vol. 83, pp. 27–39, 2018. 17

[71] M. Rahimian, J. M. Walker, and I. Penesis, "Numerical assessment of a horizontal axis marine current turbine performance," *International Journal of Marine Energy*, vol. 20, pp. 151–164, 2017. 17, 39, 52, 53

[72] E. Fernandez-Rodriguez, T. Stallard, and P. Stansby, "Experimental study of extreme thrust on a tidal stream rotor due to turbulent flow and with opposing waves," *Journal of Fluids and Structures*, vol. 51, pp. 354–361, 2014. 17

[73] T. McCombes, *An unsteady hydrodynamic model for tidal current turbines.* PhD thesis, University of Strathclyde, 2014. 17

[74] G. B. Whitham, *Linear and nonlinear waves.* John Wiley & Sons, 1974. 17, 72, 73, 75

[75] X. Bai, E. Avital, A. Munjiza, and J. Williams, "Numerical simulation of a marine current turbine in free surface flow," *Renewable Energy*, vol. 63, pp. 715–723, 2014. 18, 32

[76] L. Chamorro, C. Hill, S. Morton, C. Ellis, R. Arndt, and F. Sotiropoulos, "On the interaction between a turbulent open channel flow and an axial-flow turbine," *Journal of Fluid Mechanics*, vol. 716, pp. 658–670, 2013. 18

[77] N. Kolekar and A. Banerjee, "Performance characterization and placement of a marine hydrokinetic turbine in a tidal channel under boundary proximity and blockage effects," *Applied Energy*, vol. 148, pp. 121–133, 2015. 18

[78] J. Riglin, W. C. Schleicher, I.-H. Liu, and A. Oztekin, "Characterization of a micro-hydrokinetic turbine in close proximity to the free surface," *Ocean Engineering*, vol. 110, pp. 270–280, 2015. 18

[79] K. Shirasawa, J. Minami, and T. Shintake, "Scale-model experiments for the surface wave influence on a submerged floating ocean-current turbine," *Energies*, vol. 10, no. 5, p. 702, 2017. 18, 80

[80] Q. Hu, Y. Li, Y. Di, and J. Chen, "A large-eddy simulation study of horizontal axis tidal turbine in different inflow conditions," *Journal of Renewable and Sustainable Energy*, vol. 9, no. 6, p. 064501, 2017. 18

[81] S. M. Simmons, S. J. McLelland, D. R. Parsons, L.-B. Jordan, B. J. Murphy, and L. Murdoch, "An investigation of the wake recovery of two model horizontal-axis tidal stream turbines measured in a laboratory flume with particle image velocimetry," *Journal of Hydro-environment Research*, 2017. 18

[82] N. O. Jensen, "A note on wind generator interaction," tech. rep., 1983. 18

[83] P. Beaucage, M. Brower, N. Robinson, and C. Alonge, "Overview of six commercial and research wake models for large offshore wind farms," *Proceedings of the European Wind Energy Associate (EWEA)*, 2012. 18

[84] A. Peña, P.-E. Réthoré, and M. P. van der Laan, "On the application of the jensen wake model using a turbulence-dependent wake decay coefficient: the sexbierum case," *Wind Energy*, vol. 19, no. 4, pp. 763–776, 2016. 19, 61

[85] P. Pyakurel, W. Tian, J. H. VanZwieten, and M. Dhanak, "Characterization of the mean flow field in the far wake region behind ocean current turbines," *Journal of Ocean Engineering and Marine Energy*, vol. 3, no. 2, pp. 113–123, 2017. 19

[86] B. G. Newman, "Actuator-disc theory for vertical-axis wind turbines," *Journal of Wind Engineering and Industrial Aerodynamics*, pp. 347–355, 1983. 19, 20

[87] B. Newman, "Multiple actuator-disc theory for wind turbines," *Journal of Wind Engineering and Industrial Aerodynamics*, vol. 24, no. 3, pp. 215–225, 1986. 19

[88] H. Sundararaju, K. H. Lo, R. Metcalfe, and S. S. Wang, "Aerodynamics and cfd analysis of equal size dual-rotor wind turbine," *Journal of Renewable and Sustainable Energy*, vol. 9, no. 4, p. 043305, 2017. 19, 20, 57

[89] P. Mycek, B. Gaurier, G. Germain, G. Pinon, and E. Rivoalen, "Experimental study of the turbulence intensity effects on marine current turbines behaviour. part ii: Two interacting turbines," *Renewable Energy*, vol. 68, pp. 876–892, 2014. 19, 54, 57

[90] W. Z. Shen, V. A. K. Zakkam, J. N. Sørensen, and K. Appa, "Analysis of counter-rotating wind turbines," in *Journal of Physics Conference Series*, p. 012003, 2007. 19

[91] A. Vaselbehagh and C. L. Archer, "Wind farms with counter-rotating wind turbines," *Sustainable Energy Technologies and Assessments*, vol. 24, pp. 19–30, 2017. 19, 20

[92] S. Lee, E. Son, and S. Lee, "Velocity interference in the rear rotor of a counter-rotating wind turbine," *Renewable Energy*, vol. 54, pp. 235–240, 2013. 19

[93] S. N. Jung, T. No, and K. Ryu, "Aerodynamic performance prediction of a 30kw counter-rotating wind turbine system," *Renewable Energy*, vol. 30, no. 5, pp. 631–644, 2005. 19, 20

[94] W. Cho, K. Lee, I. Choy, and J. Back, "Development and experimental verification of counter-rotating dual rotor/dual generator wind turbine: Generating, yawing and furling," *Renewable Energy*, vol. 114, pp. 644–654, 2017. 20

[95] Z. Wang, A. Ozbay, W. Tian, and H. Hu, "An experimental study on the aerodynamic performances and wake characteristics of an innovative dual-rotor wind turbine," *Energy*, vol. 147, pp. 94–109, 2018. 20

[96] B. Hwang, S. Lee, and S. Lee, "Optimization of a counter-rotating wind turbine using the blade element and momentum theory," *Journal of Renewable and Sustainable Energy*, vol. 5, no. 5, p. 052013, 2013. 20

[97] J. Clarke, G. Connor, A. Grant, and C. Johnstone, "Design and testing of a contra-rotating tidal current turbine," *Proceedings of the Institution of Mechanical Engineers, Part A: Journal of Power and Energy*, vol. 221, no. 2, pp. 171–179, 2007. 20

[98] B. Huang, G. J. Zhu, and T. Kanemoto, "Design and performance enhancement of a bi-directional counter-rotating type horizontal axis tidal turbine," *Ocean Engineering*, vol. 128, pp. 116–123, 2016. 20

[99] V. Okulov, J. N. Sørensen, and G. A. van Kuik, *Development of the optimum rotor theories: On the 100th Anniversary of Professor Joukowsky's vortex theory of screw propeller*. R&C Dynamics, 2013. 23

[100] A. Betz, "Das maximum der theoretisch möglichen ausnutzung des windes durch windmotoren," *Zeitschrift fur das gesamte Turbinenwesten*, vol. 20, 1920. 23

[101] H. Glauert, "Airplane propellers," in *Aerodynamic theory*, pp. 169–360, Springer, 1935. 23, 26

[102] H. Snel, "A short history of wind turbine aerodynamics, or: From betz to better," in *Invited presentation for the Conference: The second conference on the Science of Making Torque from Wind, Lyngby, Denmark, AuguSt*, pp. 28–3l, 2007. 23

[103] P. J. Moriarty and A. C. Hansen, "Aerodyn theory manual," tech. rep., National Renewable Energy Lab., Golden, CO (US), 2005. 23, 73

[104] J. Tangler and D. Kocurek, "Wind turbine post-stall airfoil performance characteristics guidelines for blade-element momentum methods," in *43rd AIAA Aerospace Sciences Meeting and Exhibit*, p. 591, 2005. 24, 28

[105] H. Snel and J. Schepers, *Joint investigation of dynamic inflow effects and implementation of an engineering method.* Netherlands Energy Research Foundation ECN, 1995. 24, 27, 28

[106] T. Burton, D. Sharpe, N. Jenkins, and E. Bossanyi, *Wind energy handbook.* John Wiley & Sons, 2001. 26, 45

[107] S.Oye, "Dynamic stall simulated as time lag of separation," *Proceedings of the 4th IEA Symposium on the Aerodynamics of Wind Turbines*, 1991. 27, 28

[108] S. F. Hoerner and H. V. Borst, *Fluid-dynamic lift: Practical information on aerodynamic and hydrodynamic lift.* Hoerner Fluid Dynamics, 1985. 28

[109] H. K. Versteeg and W. Malalasekera, *An introduction to computational fluid dynamics: the finite volume method.* Pearson Education, 2007. 30

[110] F. G. Schmitt, "About boussinesq's turbulent viscosity hypothesis: historical remarks and a direct evaluation of its validity," *Comptes Rendus Mécanique*, vol. 335, no. 9, pp. 617–627, 2007. 30

[111] S. B. Pope, *Turbulent flows.* Cambridge University Press, 2001. 30

[112] B. E. Launder and D. B. Spalding, *Mathematical models of turbulence.* Academic press, 1972. 30

[113] F. R. Menter, "Review of the shear-stress transport turbulence model experience from an industrial perspective," *International Journal of Computational Fluid Dynamics*, vol. 23, no. 4, pp. 305–316, 2009. 31

[114] F. R. Menter, "Two-equation eddy-viscosity turbulence models for engineering applications," *AIAA Journal*, vol. 32, no. 8, pp. 1598–1605, 1994. 31

[115] R. Malki, A. Williams, T. Croft, M. Togneri, and I. Masters, "A coupled blade element momentum–computational fluid dynamics model for evaluating tidal stream turbine performance," *Applied Mathematical Modelling*, vol. 37, no. 5, pp. 3006–3020, 2013. 32

[116] B. Francois, M. Costes, G. Dufour, C. Cerfacs, and T. France, "Comparison of chimera and sliding mesh techniques for unsteady simulations of counter rotating open-rotors," in *20th International Symposium on Air Breathing Engines· ISABE 2011*, 2011. 33

[117] Fluent, "Ansys fluent customization manual," *Ansys Inc*, 2017. 34

[118] X. Shen, T. Korakianitis, and E. Avital, "Numerical investigation of surface curvature effects on aerofoil aerodynamic performance," in *Applied Mechanics and Materials*, vol. 798, pp. 589–595, Trans Tech Publ, 2015. 37

[119] M. Ahmed, E. Avital, and T. Korakianitis, "Investigation of improved aerodynamic performance of isolated airfoils using circle method," *Procedia Engineering*, vol. 56, pp. 560–567, 2013. 37

[120] R. J. McGhee, B. S. Walker, and B. F. Millard, "Experimental results for the eppler 387 airfoil at low reynolds numbers in the langley low-turbulence pressure tunnel," tech. rep., Langley Research Center, Hamption Virginia, 1988. 38

[121] S. Ning, "Airfoilprep. py documentation: Release 0.1. 0," tech. rep., National Renewable Energy Lab.(NREL), Golden, CO (United States), 2013. 39

[122] T. Karthikeyan, E. Avital, N. Venkatesan, and A. Samad, "Design and analysis of a marine current turbine," in *ASME 2017 Gas Turbine India Conference*, pp. V001T02A014–V001T02A014, American Society of Mechanical Engineers, 2017. 39, 52

[123] R. A, *Wind turbines lecture notes*. Technion press, 1987. 45, 50, 68

[124] K.-W. Ng, W.-H. Lam, and K.-C. Ng, "2002–2012: 10 years of research progress in horizontal-axis marine current turbines," *Energies*, vol. 6, no. 3, pp. 1497–1526, 2013. 49

[125] Y. J. Gu, Y. G. Lin, Q. K. Xu, H. W. Liu, and W. Li, "Blade-pitch system for tidal current turbines with reduced variation pitch control strategy based on tidal current velocity preview," *Renewable Energy*, vol. 115, 2018. 49

[126] X. Shen, E. Avital, M. A. Rezaienia, G. Paul, and T. Korakianitis, "Computational methods for investigation of surface curvature effects on airfoil boundary layer behavior," *Journal of Algorithms & Computational Technology*, vol. 11, no. 1, pp. 68–82, 2017. 51, 55

[127] K. Ai, E. Avital, T. Korakianitis, A. Samad, and N. Venkatesan, "Surface wave effect on marine current turbine, modelling and analysis," in *Mechanical and Aerospace Engineering (ICMAE), 2016 7th International Conference on*, pp. 180–184, IEEE, 2016. 51, 53

[128] J. G. Leishman, "Aerodynamic performance considerations in the design of a coaxial proprotor," *Journal of the American Helicopter Society*, vol. 54, no. 1, pp. 12005–12005, 2009. 51

[129] J. R. Marden, S. D. Ruben, and L. Y. Pao, "A model-free approach to wind farm control using game theoretic methods," *IEEE Transactions on Control Systems Technology*, vol. 21, no. 4, pp. 1207–1214, 2013. 51

[130] J. Mcnaughton, *Turbulence modelling in the near-field of an axial flow tidal turbine in code_saturne*. PhD thesis, School of Mechanical, Aerospace and Civil Engineering, 2013. 52

[131] G. Lloyd and A. Espanoles, "Best practice guidelines for marine applications of computational fluid dynamics," *WS Atkins Consultants and Members of the NSC, MARNET-CFD Thernatic Network: London, UK*, p. 84, 2002. 53

[132] E. N. Jacobs and A. Sherman, "Airfoil section characteristics as affected by variations of the reynolds number," tech. rep., National Advisory Committee for Aeronautics, Langley Aeronautical Laboratory, USA, 1937. 55

[133] S. Guntur and N. N. Sørensen, "An evaluation of several methods of determining the local angle of attack on wind turbine blades," in *Journal of Physics: Conference Series*, vol. 555, p. 012045, IOP Publishing, 2014. 59

[134] E. Jost, L. Klein, H. Leipprand, T. Lutz, and E. Krämer, "Extracting the angle of attack on rotor blades from cfd simulations," *Wind Energy*, 2017. 59

[135] H. Rahimi, J. Schepers, W. Z. Shen, N. R. García, M. Schneider, D. Micallef, C. S. Ferreira, E. Jost, L. Klein, and I. Herráez, "Evaluation of different methods for determining the angle of attack on wind turbine blades with cfd results under axial inflow conditions," *Renewable Energy*, vol. 125, pp. 866–876, 2018. 59

[136] T. Göçmen, P. Van der Laan, P.-E. Réthoré, A. P. Diaz, G. C. Larsen, and S. Ott, "Wind turbine wake models developed at the technical university of denmark: A review," *Renewable and Sustainable Energy Reviews*, vol. 60, pp. 752–769, 2016. 61

[137] T. Karthikeyan, K. Ezhilsabareesh, A. Samad, N. Venkatesan, E. AVITAL, *et al.*, "Parametric analysis of a tidal current turbine using cfd techniques," in *Renew 2016 2nd International Conference on Renewable Energies Offshore*, CRC Press, 2016. 68

[138] A. Heffron, J. J. Williams, and E. J. Avital, "Flow seperation and passive flow control on e387 airfoil," in *54th AIAA Aerospace Sciences Meeting*, p. 0324, 2016. 72

[139] P. Lin, *Numerical modeling of water waves*. CRC Press, 2008. 72

[140] A. Björck, "Dynstall: Subroutine package with a dynamic stall model," *Aeronautical Research Inst. of Sweden, TR-FFAP*, vol. 110, 2000. 73

[141] I. Afgan, J. McNaughton, S. Rolfo, D. Apsley, T. Stallard, and P. Stansby, "Turbulent flow and loading on a tidal stream turbine by les and rans," *International Journal of Heat and Fluid Flow*, vol. 43, pp. 96–108, 2013. 74

[142] W. H. Press, S. A. Teukolsky, W. T. Vetterling, and B. P. Flannery, *Numerical recipes in FORTRAN 90 the art of parallel scientific computing*, vol. 2. Cambridge University Press, 1996. 78, 79

[143] S. Tatum, M. Allmark, C. Frost, D. O. Doherty, A. Masonjones, and T. O. Doherty, "Cfd modelling of a tidal stream turbine subjected to profiled flow and surface gravity waves," *International Journal of Marine Energy*, vol. 15, pp. 156–174, 2016. 79

[144] E. Avital, T. Korakianitis, and F. Motallebi, "Low reynolds number proprotor aerodynamic performance improvement using the continuous surface curvature design approach," *The Aeronautical Journal*, pp. 1–19, 2018. 84